When do cosmic peaks, filaments, or walls merge? A theory of critical events in a multiscale landscape

C. Cadiou, C. Pichon, S. Codis, M. Musso, D. Pogosyan, Y. Dubois, J.-F. Cardoso, S. Prunet

Monthly Notices
of the
ROYAL ASTRONOMICAL SOCIETY

MNRAS **496,** 4787–4821 (2020)
Advance Access publication 2020 June 26

doi:10.1093/mnras/staa1853

When do cosmic peaks, filaments, or walls merge? A theory of critical events in a multiscale landscape

C. Cadiou [1,2]★ C. Pichon,[2,3,4] S. Codis,[2,4] M. Musso,[5] D. Pogosyan,[3,6] Y. Dubois,[2] J.-F. Cardoso[2] and S. Prunet[7]

[1]*Department of Physics and Astronomy, University College London, London WC1E 6BT, UK*
[2]*CNRS and Sorbonne Université, UMR 7095, Institut d'Astrophysique de Paris, 98 bis Boulevard Arago, F-75014 Paris, France*
[3]*Korea Institute of Advanced Studies (KIAS) 85 Hoegiro, Dongdaemun-gu, Seoul 02455, Republic of Korea*
[4]*IPHT, DRF-INP, UMR 3680, CEA, Orme des Merisiers Bat 774, F-91191 Gif-sur-Yvette, France*
[5]*East African Institute for Fundamental Research (ICTP-EAIFR), KIST2 Building, Nyarugenge Campus, University of Rwanda, PO Box 4285, Kigali, Rwanda*
[6]*Department of Physics, University of Alberta, 11322-89 Avenue, Edmonton, Alberta T6G 2G7, Canada*
[7]*Canada-France-Hawaii Telescope, 65-1238 Mamalahoa Highway, Kamuela, HI 96743, USA*

Accepted 2020 June 22. Received 2020 May 13; in original form 2020 March 9

ABSTRACT

The merging rate of cosmic structures is computed, relying on the *ansatz* that they can be predicted in the initial linear density field from the coalescence of critical points with increasing smoothing scale, used here as a proxy for cosmic time. Beyond the mergers of peaks with saddle points (a proxy for halo mergers), we consider the coalescence and nucleation of all sets of critical points, including wall-saddle to filament-saddle and wall-saddle to minima (a proxy for filament and void mergers, respectively), as they impact the geometry of galactic infall, and in particular filament disconnection. Analytical predictions of the one-point statistics are validated against multiscale measurements in 2D and 3D realizations of Gaussian random fields (the corresponding code being available upon request) and compared qualitatively to cosmological N-body simulations at early times ($z \geq 10$) and large scales ($\geq 5\,\mathrm{Mpc}\,h^{-1}$). The rate of filament coalescence is compared to the merger rate of haloes and the two-point clustering of these events is computed, along with their cross-correlations with critical points. These correlations are qualitatively consistent with the preservation of the connectivity of dark matter haloes, and the impact of the large-scale structures on assembly bias. The destruction rate of haloes and voids as a function of mass and redshift is quantified down to $z = 0$ for a Lambda cold dark matter cosmology. The one-point statistics in higher dimensions are also presented, together with consistency relations between critical point and critical event counts.

Key words: galaxies: evolution – galaxies: formation – galaxies: kinematics and dynamics – cosmology: theory – large-scale structure of Universe.

1 INTRODUCTION

The large-scale structures of our observable Universe are routinely observed through the distribution of galaxies, neutral gas, or dark matter. As such, galaxies and their haloes are both probes of the large-scale density field (from the point of view of cosmology), and the subject of interest (from the point of view of galaxy formation). It is now accepted that the large-scale structures are key to understand galaxy formation, for example, by driving angular momentum acquisition through cosmic cold streams (Dekel & Birnboim 2006; Agertz, Teyssier & Moore 2009; Pichon et al. 2011; Danovich et al. 2012; Dubois et al. 2012) and by galaxy mergers, which efficiently disrupt galaxies into ellipticals (e.g. Toomre & Toomre 1972; Naab & Burkert 2003; Bournaud, Jog & Combes 2007). This scale coupling is also relevant to cosmology, as it influences, for example, lensing observations through spin alignments (Crittenden et al. 2001; Codis, Pichon & Pogosyan 2015). In the era of precision cosmology, any attempt to infer cosmological parameters from observations of galaxies and haloes should therefore take into account the influence of the surrounding large-scale structures. Since the details of the buildup of cosmic structure and galaxies are encoded in the initial matter density field and are coupled, one could, in principle, predict their joint evolution from the initial conditions. Considering that an initial Gaussian random field with small density perturbations leads to the formation of both cosmic structures and galaxies, some descriptive statistics of this field can be used to jointly predict the final fate of galaxies, haloes, and the cosmic web. More specifically – and this will be the topic of this paper – we should be able to identify special sets of points via a multiscale analysis of the initial conditions (as a means of compressing the relevant information content of this field) and use them to predict the fate of cosmic structures.

The topology of the initial density field at a given smoothing scale is encoded in the positions and heights of all its critical points, namely extrema (maxima and minima) and saddle points (filament-type and wall-type saddle points). For instance, peaks in the initial conditions will later form the nodes of the cosmic web (Bardeen et al. 1986), while bridges in between, in the middle of which is found a saddle point, will subsequently collapse due to the tidal anisotropies to form filaments (Bond, Kofman & Pogosyan 1996;

★ E-mail: c.cadiou@ucl.ac.uk

Rossi 2013). Conversely, voids will develop from the initial minima (Sheth & van de Weygaert 2004), and walls around wall-type saddle points. Beyond the strong focus on extrema, Pogosyan et al. (2009b) developed a theoretical framework, the skeleton, to understand the structure of the cosmic web as a whole (walls and filaments) in terms of gradient lines joining peaks and voids through saddle points. In this context, computational geometry allows us to quantify the strength of topological pairing between critical points (Sousbie, Pichon & Kawahara 2011; van de Weygaert et al. 2011) through persistence (Edelsbrunner, Letscher & Zomorodian 2002; Pranav et al. 2017), which measures their relative heights, and defines a scale-free hierarchy amongst filaments, walls, and voids of the cosmic web.

Focusing now on haloes, within the paradigm of the spherical gravitational collapse, one can draw a relationship between the time of collapse of the initial overdense patch and the scale at which it must be smoothed so as to pass a theoretically given overdensity threshold (Press & Schechter 1974), and therefore map features of the initial linear density field to later-time non-linear structures. In practice, not only does the patch need to pass a given density threshold as a function of smoothing but additional constraints must be added, notably to avoid double counting (the so-called cloud-in-cloud problem). This requires enforcing a first crossing condition to ensure that no larger scales than the one considered has collapsed, which makes the core of the excursion set approach (Peacock & Heavens 1990; Bond et al. 1991; Jedamzik 1995; Maggiore & Riotto 2010; Musso & Sheth 2012). Better agreement with actual collapsed haloes can be achieved with a modified stochastic threshold that incorporates the effects of tidal forces on top of spherical collapse (Bond & Myers 1996; Sheth, Mo & Tormen 2001). When studying halo statistics in cosmological models with cold dark matter (CDM; Blumenthal et al. 1984) that exhibit the hierarchical clustering, it is also of interest to investigate the substructures (hence smaller scales) within a given patch so as to study its assembly history. Lacey & Cole (1993) showed that the properties of the excursion set trajectories carry information on the matter accretion history of the forming haloes, allowing us to split this accretion into a smooth component on the one hand and mergers on the other hand. In this sense, the fate of a given region is encoded in its initial conditions and is captured by the multiscale properties of the corresponding Gaussian random field.

Going one step further, Manrique & Salvador-Sole (1995, 1996) brought together the virtues of the two approaches (peaks and excursion sets) in the so-called confluent system formalism, where excursion set trajectories are not randomly located in space and concentric, but insist on peaks and follow their position as the smoothing scale changes. This approach was later perfected and made more analytically manageable (Paranjape & Sheth 2012; Paranjape, Sheth & Desjacques 2013), including the effect of tidal shear (Castorina et al. 2016).

The very notion of special points in the position–smoothing space is hence crucial in the context of modelling the evolution of haloes but also of the cosmic web as a whole. The drift of critical points with smoothing defines the so-called skeleton tree (Hanami 2001), which captures the variation of this topology with smoothing scale, hence time. One can identify special scales at which two such points coalesce, hence producing merger *events*, as they are located in time as well as in space, of different types, corresponding to mergers of haloes, filaments, walls, or voids. In that paper, the focus was on the coalescence of filament saddles with maxima, which the author named sloping saddles (as they are vanishing saddle points on the slope of peaks), identified as proxies for merging events. These are known to play a significant role in triggering active galactic nucleus feedback, which impacts gas inflow and therefore galactic morphology (Dubois et al. 2016). Coalescence of other critical points also impact the geometry of the cosmic web (in particular the filaments), which defines preferred directions along which galaxies are fed cold gas and acquire their spin. They also impact wall disappearance, hence void statistics (Dubinski et al. 1993).

The focus should now therefore be on special points in the $3+1\mathrm{D}$[1] position–smoothing space, where these paired critical points merge, i.e. when the persistence level tends to zero as a function of smoothing. Using the above-mentioned mapping between scale and cosmic time provided by the spherical collapse model, we will rely on the *ansatz* that these mergers in the initial linear density field can be matched to structurally important special moments that modify the topology of the evolved non-linear density field, while a more careful evaluation of the accuracy of this assumption will be carried out in future works. For instance, when two haloes merge, the topology of the excursion set of the density field (i.e. the region above a given threshold) is changed because it decrements the number of components above the threshold.

Mapping the geometry of the Gaussian random field on to the knowledge of only these singular events is a very efficient and useful compression of the information encoded in the field. It is efficient because it compresses the information about a 3D random field into a finite set of points in $3+1\mathrm{D}$. It is useful because (i) these points bear significance in terms of cosmology or galaxy formation, and (ii) we will be able to characterize the corresponding point process in terms of the properties of the underlying initial Gaussian field – therefore, statistically, in terms of the underlying power spectrum.

Hence, in this paper, we will present a 'critical event theory' to capture not only the evolution of the halo hosting the galaxy via its merger tree, but also the evolution of the spatial structures that fed it, which are known to affect the acquisition of secondary galactic properties (such as their angular momentum) and may thus contribute to assembly bias. We will include the coalescence of minima with wall-type saddles and wall-type saddles with filament-type saddles corresponding, respectively, to the merging of two walls (with a void disappearing in between) and two filaments (with disappearance of a wall). We will finally study the clustering properties of all these critical events in the multiscale landscape, as a means to relate their sequence and geometry to the events relevant to the evolution of galaxies.

Our astrophysical motivations are the following. Study the generalized history of accretion: What kind of mergers happen when, and where? Quantify the conditional rate of filament and wall disappearance in conjunction to that of an existing larger scale critical point. Understand the origin of void disappearance and its usefulness as a cosmic probe for dark energy. Connect the multiscale landscape of initial conditions to the properties of dark matter haloes. Study how the anisotropic large-scale modes bias its assembly history. Beyond astrophysics, we aim to quantify the statistical properties of zero persistence points in a multiscale landscape and to provide tools to identify such points.

This paper proceeds as follows. Section 2 forecasts critical events through the coalescence of critical points in the multiscale density landscape. We present a formal definition of critical events and re-derive the condition for a critical event in an arbitrary frame. We derive their one-point statistics in two and three dimensions (in the main text) and higher dimensions (in the Appendix) as a function of their height and kind. We also propose an extension of the theory

[1]The field smoothed at all scales has a 3D spatial component and a 1D smoothing scale component, hence the short-hand notation '$3+1\mathrm{D}$'.

Table 1. Summary of notations and definitions.

Notation	Equation	Note
Definitions		
$\delta(R)$	(1)	Density field smoothed over a scale R
$\sigma_i^2(R)$	(3)	Variance of the ith derivative of the density field
x, x_i, x_{ij}, x_{ijk}	(2)	Density, density first, second, and third derivatives, normalized by their variance
$R_0, R_*, \tilde{R}$	(4)	Typical separation between zero-crossings, critical points, and inflection points
$\gamma, \tilde{\gamma}$	(5)	Cross-correlation coefficients between the field and its derivatives
$\mathbf{H}, H = \det(\mathbf{H})$	(7), (8)	Density Hessian matrix and determinant
Notations		
p, f, w, v		Peak, filament-saddle, wall-saddle, and void (minima) critical points
$\mathcal{P}, \mathcal{F}, \mathcal{W}$		Peak, filament, and wall critical events
Critical point definitions		
$n_{\rm cp}$		Total number density
$n_{\rm cp}^{(j)}$		Total number density of kind $j \in \{\rm p, f, w, v\}$
$n_{\rm cp}^{(j)}(\nu)$		Number density of kind $j \in \{\rm p, f, w, v\}$ at height ν
Critical event definitions		
$n_{\rm ce}$	(9), (11)	Total number density
$n_{\rm ce,+}, n_{\rm ce,-}$	(13)	Total number density of nucleation (+) and destruction (−)
$n_{\rm me}$	(15)	Total net merger rate (critical event net density)
$n_{\rm me}^{(j)}$	(21)	Total net merger rate of kind $j \in \{\mathcal{P}, \mathcal{F}, \mathcal{W}\}$
$n_{\rm me}^{(j)}(\nu)$	(30)	Net merger rate of kind $j \in \{\mathcal{P}, \mathcal{F}, \mathcal{W}\}$ at height ν

for mildly non-Gaussian fields. Section 3 presents the two-point statistics of critical events in simplified setups. We present numerical integrations of the auto- and cross-correlation functions of different kind of critical events and of their number densities in the presence of a large-scale tide. We also derive analytically the clustering of peak critical events in their simplest configuration. Section 4 compares the predictions of the one-point statistics to realizations of Gaussian random fields for validation for different linear matter power spectra. We also present measurements of the auto- and cross-correlation functions in the general case. Section 5 discusses possible applications in astrophysics and beyond. We present predictions of the destruction rate of haloes and voids as a function of cosmic time. We present consistency relations with the evolution of the cosmic connectivity. We develop how the framework can be applied to the problem of assembly bias. We also make qualitative comparisons to N-body simulations. Section 6 presents our conclusions. A summary of the notations and conventions used throughout this paper is provided in Table 1.

Appendix A presents the counts in arbitrary dimensions and illustrates them in up to 6D. Appendix B explores the duality between critical points and critical events. Appendix C discusses alternative interpretations of critical events from low to high densities. Appendix D describes the local behaviour of critical point lines near their coalescence. Appendix E presents algorithms to generate Gaussian random fields satisfying a set of given 'events' at some scale and position. Appendix F generalizes some results using alternative definitions to relate critical events to mergers in physical space. Appendix G gives the joint PDF of a Gaussian random field up to the third derivative of the field. Appendix H explains how the critical events are measured in random field maps and cubes.

2 THEORY: ONE-POINT STATISTICS OF CRITICAL EVENTS

In this paper, we consider the overdensity at position $\boldsymbol{r}$, $\delta(\boldsymbol{r}) = \rho(\boldsymbol{r})/\bar{\rho} - 1$, to be a homogeneous and isotropic Gaussian random field of zero mean and linear power spectrum P_k, smoothed on scale R. In this section, we will focus on one-point statistics associated with merger rates of the field critical points as the smoothing scale increases. In Section 2.1, we define different quantities used throughout this paper to describe the relevant features of the field. Section 2.2 presents the number density of critical events. Section 2.3 introduces critical events of different types (peak, filament, and wall mergers) and calculates their total and differential densities at given height. Section 2.4 sketches the corresponding theory for projected maps, while Section 2.5 presents its extension to non-Gaussian fields.

In this section, limiting assumptions are introduced as late as possible: All the results are general up to Section 2.2, which introduces the requirement for a Gaussian filter. In Section 2.3 and after, and unless stated otherwise, it is assumed that the field is a Gaussian random field smoothed by a Gaussian filter. We also remind the reader that a summary of the notations and definitions used throughout this paper can be found in Table 1.

2.1 Characteristic features of a field

Let us first introduce the dimensionless quantities for the density field, smoothed over a scale R by a filter function W:

$$\delta(\boldsymbol{r}, R) = \int \frac{\mathrm{d}^3k}{(2\pi)^3}\delta(\boldsymbol{k})W(kR)\mathrm{e}^{i\boldsymbol{k}\cdot\boldsymbol{r}}\,. \tag{1}$$

We will consider the statistics of this field and its derivatives in this paper. For practical purposes, let us introduce the dimensionless quantities:

$$x \equiv \frac{\delta}{\sigma_0},\ x_k \equiv \frac{\nabla_k\delta}{\sigma_1},\ x_{kl} \equiv \frac{\nabla_k\nabla_l\delta}{\sigma_2},\ x_{klm} \equiv \frac{\nabla_k\nabla_l\nabla_m\delta}{\sigma_3}, \tag{2}$$

which are normalized by their respective variance,

$$\sigma_i^2(R) \equiv \frac{1}{2\pi^2}\int_0^\infty \mathrm{d}k k^2 P_k(k) k^{2i} W^2(kR)\,, \tag{3}$$

so that we have $\langle x^2\rangle = \sum_k \langle x_k x_k\rangle = \sum_{k,l}\langle x_{kl}x_{kl}\rangle = \sum_{k,l,m}\langle x_{klm}x_{klm}\rangle = 1$. Note that here and in the rest of this paper, we have dropped the explicit dependence of the quantities of equation (2) on the smoothing scale.

Following closely Pogosyan et al. (2009b), let us introduce the characteristic scales of the field:

$$R_0 = \frac{\sigma_0}{\sigma_1}, \quad R_* = \frac{\sigma_1}{\sigma_2}, \quad \tilde{R} = \frac{\sigma_2}{\sigma_3}. \tag{4}$$

These scales are ordered as $R_0 \geq R_* \geq \tilde{R}$. The first two have well-known meanings of typical separation between zero-crossing of the field and mean distance between extrema, respectively (Bardeen et al. 1986). The third one, $\tilde{R}$, is by analogy the typical distance between inflection points.

Let us define a set of spectral parameters that depend on the shape of the underlying power spectrum. Out of the three scales introduced above, two dimensionless ratios may be constructed that are intrinsic parameters of the theory:

$$\gamma \equiv \frac{R_*}{R_0} = \frac{\sigma_1^2}{\sigma_0\sigma_2}, \quad \tilde{\gamma} \equiv \frac{\tilde{R}}{R_*} = \frac{\sigma_2^2}{\sigma_1\sigma_3}. \tag{5}$$

From the geometrical point of view, γ specifies how frequently one encounters a maximum between two zero-crossings of the field, while $\tilde{\gamma}$ describes, on average, how many inflection points are between two extrema. From a statistical perspective, γ and $\tilde{\gamma}$ are cross-correlation coefficients between the field and its derivatives at the same point:

$$\gamma = -\frac{\langle \delta \Delta \delta \rangle}{\sigma_0\sigma_2}, \quad \tilde{\gamma} = -\frac{\langle \nabla\delta \cdot \nabla^2 \nabla\delta \rangle}{\sigma_1\sigma_3}. \tag{6}$$

These scales and scale ratios fully specify the correlations between the field and its derivative (up to third order) at the same point. For power-law power spectra of index n, $P_k(k) \propto k^n$, with Gaussian smoothing at the scale R in 3D, $R_0 = R\sqrt{2/(n+3)}$, $R_* = R\sqrt{2/(n+5)}$, and $\tilde{R} = R\sqrt{2/(n+7)}$ while $\gamma = \sqrt{(n+3)/(n+5)}$ and $\tilde{\gamma} = \sqrt{(n+5)/(n+7)}$. See also Appendix A1 for their generalization to any dimension.

2.1.1 Critical points of the random field

Critical *points* of the 3D field at fixed smoothing scale are defined as places where the spatial gradient of the field vanishes: $\nabla\delta = 0$. This provides a number of conditions exactly equal to the dimensionality of the space, and thus is, in general, satisfied only at isolated points. The type of critical point is given by the signs of the eigenvalues $\sigma_2\lambda_i$ of the Hessian of the field,

$$\mathbf{H} \equiv \nabla\nabla\delta, \tag{7}$$

which we will always consider sorted $\lambda_1 \leq \lambda_2 \leq \lambda_3$.

Local extrema of the field are critical points whose eigenvalues have all the same sign, negative for maxima, and positive for minima. Other critical points are saddles of different types: In 3D, filamentary saddles have $\lambda_1 \leq \lambda_2 < 0 < \lambda_3$ and wall-like saddles have $\lambda_1 < 0 < \lambda_2 \leq \lambda_3$. Requiring ever more eigenvalues to be positive, we go from maxima to filamentary saddles to wall saddles and to minima, each type differing from the neighbours by the sign of one eigenvalue. Correspondingly, the Hessian determinant,

$$H \equiv \det(\nabla\nabla\delta) = \sigma_2^3\lambda_1\lambda_2\lambda_3, \tag{8}$$

changes sign at every step of this progression.

In Euclidean space, the average Euler characteristic is zero. This means that the alternating sum of critical points is null, i.e. $n_{\rm cp}^{\rm p} - n_{\rm cp}^{\rm f} + n_{\rm cp}^{\rm w} - n_{\rm cp}^{\rm v} = 0$, with $n_{\rm cp}^{\rm p,f,w,v}$ the mean number densities of peaks, filament-type saddle, wall-type saddles, and voids, respectively. A more formal definition is given in Appendix B. Thus, the density of all the critical points with $H > 0$ is equal to the density of ones with $H < 0$. For any dimension, this mathematically reads $\sum_{H_i>0} n_{\rm cp}^{(i)} = \sum_{H_i<0} n_{\rm cp}^{(i)}$.

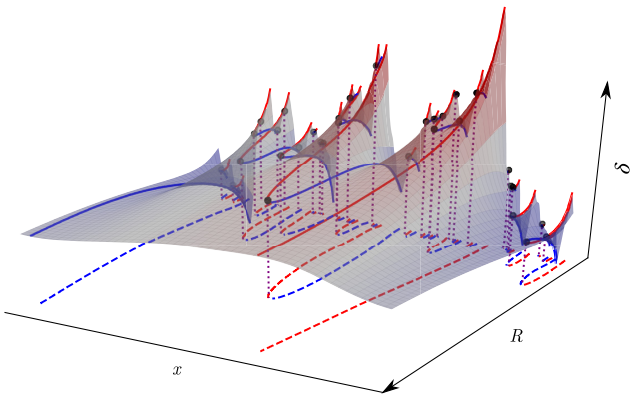

Figure 1. 1 + 1D landscape of a 1D field smoothed at a scale R. Solid lines indicate maxima (red) and minima (blue). Smoothing length R is the smallest at the backplane and increases toward the viewer; critical point lines end at critical events (black dots). The critical point lines are projected on the $\delta = -1$ plane (red and blue dashed lines). Vertical purple lines indicate the projection of critical events on to the $\delta = -1$ plane and illustrate that critical events are found at the location where two critical points merge. An interactive version can be found in the online supplemental material and online.

2.1.2 Critical event definition

Let us now define critical *events*. These events – which generalize the notion of sloping saddles in Hanami (2001) – are defined in the 3 + 1D position–smoothing space as locations where, besides $\nabla\delta = 0$, the Hessian determinant H also vanishes.[2] Because we impose these four conditions in a 4D space, the solution is a set of points in the position–smoothing space, which will be interpreted as points in space–time, hence the denomination *events*. These events in 3 + 1D space correspond to mergers of the trajectories traced by critical *points* as the smoothing scale R changes. Since, in general, at each critical event only one eigenvalue of $\mathbf{H}$ vanishes, only the tracks of critical points of neighbouring types can merge.

Fig. 1 shows the critical events for a 1 + 1D field. These events are found at the tip of critical point lines and represent the disappearance of a pair of critical points of neighbouring kind (e.g. a maximum and a minimum in case of one spatial dimension, a maximum, and a saddle point for higher dimensions). At a critical event, the topology of the field at fixed R slice is changed by removing a pair of critical points. The inverse process where a critical point pair is created and two trajectories emerge from a critical event[3] is also possible (for a Gaussian filter, only in more than 1D), although, as we will show further, much less probable.

Let us illustrate the concept of critical events using an analogy with a mountainous landscape, the latter being restricted to 2D space. A mountainous landscape is made of peaks analogous to proto-haloes. A peak is linked to some of its neighbours via mountain passes that form a proto-filamentary structure. Following the ridge from one peak to another one is analogous to following a filamentary structure between two proto-haloes. With the action of time, the mountains

[2]We warn against possible confusion that critical events are not a generalization of critical points to the position–smoothing space. The additional condition imposed is not $\partial\delta/\partial R = 0$ but $H = 0$.

[3]In this paper, we will always be speaking about mergers or creation as smoothing increases, i.e. consider trajectories traced by critical points in the direction of increasing R. In general, one could also consider unsmoothing the field as a proxy for some control parameter in the context of bifurcation theory.

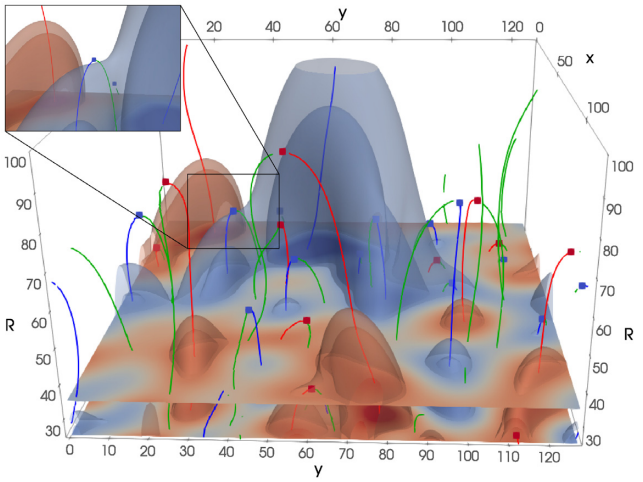

Figure 2. 2 + 1D landscape of a 2D field smoothed at a scale R. The density field (blue to red map) is smoothed at increasing (upward) R. For each scale, the critical points (red lines: peaks, green lines: saddle points, blue lines: minima) are found. At the tip of each branch, a critical event is found (red: peak-saddle critical events, blue: saddle-minima). Isocontours of density in 2 + 1D are shown as transparent surfaces (blue for negative density and red for positive density). An interactive version can be found in the online supplemental material and online. Note that the critical points at coordinate ∼(50, 20) (see inset) or ∼(110, 55) are indeed clearly sloping saddles: One of the eigenvalues of the Hessian vanishes as the curvature changes.

will erode until eventually no peak will subsist – this is analogous to the smoothing operation. In the process, a disappearing peak will see its height (the density) decrease with time. If the peak is not prominent enough, it will eventually be smoothed to the point where it no longer is a peak but a shoulder on another peak's slope. Just before the peak disappears, it is still linked to its neighbour via a pass. When the peak disappears, so does the pass – indeed, a pass is always located between *two* peaks; when one disappears, so does the pass. This particular event is what we defined as a critical *event*. It encodes the moment when two critical points (here a peak and a saddle point) annihilate. This can also be interpreted as the moment a peak disappears on the slope of its nearest neighbour – the two peaks merged and the most prominent subsisted. Critical events have hence a dual interpretation. Figs 2 and 3 show an illustration in this specific case of a 2 + 1D field using a 3D visualization and a sequence of 2D renderings at various smoothing length. Critical events can be equivalently defined as pairs of critical points with vanishing persistence (Edelsbrunner et al. 2002).[4]

In the following, we will rely on the *ansatz* that critical points (peaks, filament saddles, wall saddles, and minima) in the linear density field can be mapped into late-time structures of the cosmic web (haloes, filaments, walls, and voids, respectively), with increasing smoothing scales probing later times. Under this assumption, critical events (where critical points merge) can be interpreted as mergers of cosmic structures. While this assumption sounds generally reasonable, a word of caution is required. For instance, the formation redshift, z, of a halo is usually related to the height δ of the corresponding peak through the relation $\delta = \delta_c/D(z)$, with peaks of vanishing height forming haloes asymptotically late in the future. This automatically excludes local maxima of negative height from the picture. Thus, critical events where local maxima of negative height disappear should never be associated to halo mergers, nor should those where local minima of positive height disappear be associated to void mergers. Similarly, critical events leading to the creation of critical points (unlikely, but possible nucleation) have no obvious late-time counterparts. We will come back to these details later.

Since the primordial density field is a 3D field, the density landscape is made of peaks (proto-haloes), saddle points (proto-filaments and proto-walls), and minima (proto-voids). Critical events record the merger of peaks into proto-filaments (PF critical events), of proto-filaments into proto-walls (FW critical events) and of proto-walls into proto-voids (WV critical events). This is illustrated in Fig. 4. PF critical events (top panel) encode the merger of two haloes separated by a filament. After the merger, the most prominent peak subsists, while the other proto-halo and the proto-filament have disappeared. FW critical events (centre panel) encode the merger of two filaments separated by a wall. After the merger, the most prominent proto-filament subsists, while the other proto-filament and the proto-wall have disappeared. WV critical events (bottom panel) encode the merger of two walls separated by a void. After the merger, the most prominent wall subsists, while the other proto-wall and the proto-void have disappeared. Note that here we have interpreted the merger from the viewpoint of the densest surviving structure (e.g. the surviving peak of a peak-filament merger), but a dual interpretation is possible that instead takes the viewpoint of the least dense structure. This is further discussed in Appendix C but is kept out of the main text for the sake of conciseness. In the rest of this paper and unless stated otherwise (as in e.g. Section 5.1), we will always use the former interpretation.

2.2 Critical event number density

In this section, we will present the derivation of the mean number density of critical events in the 3 + 1D position–smoothing space. The averaging is performed over ensemble of field realizations on 3D spatial slices and the resulting mean density is smoothing dependent. In Section 2.2.1, we demonstrate how one can express the critical event constraint as a function of the local properties of the field and its derivatives. We also describe in more details the link between the 3 + 1D density of critical events and the rate of change with smoothing of the 3D spatial density of critical points and introduce the concept of *net merger event density* (see also Appendix B). We then perform in Section 2.2.2 the computation of the critical event density in the eigenframe of the Hessian of the field where it takes a simpler form.

2.2.1 *General formulation*

As defined in Section 2.1.2, each critical event is a solution $(\boldsymbol{r}_{ce}, R_{ce})$ of the set of constraint equations $\nabla\delta = 0$ and $H = 0$, the latter implying that one eigenvalue of the Hessian vanishes. In the direction of the null eigenvector, the field behaves as at a flat (critical) inflection point. Following Hanami (2001), the number density of critical events

[4]Recalling that topology defines a special relationship between specific sets of critical points, which create and destroy topological components of the excursion, persistence – the height difference between such points – is a measure of the robustness of the newly created component. Hence, vanishingly low persistence pairs correspond to vanishingly short-lived components when scanning the excursion, or changes in topology when smoothing. Note that persistence is traditionally used in computational geometry to de-noise data, rather than to probe multiple scales at once.

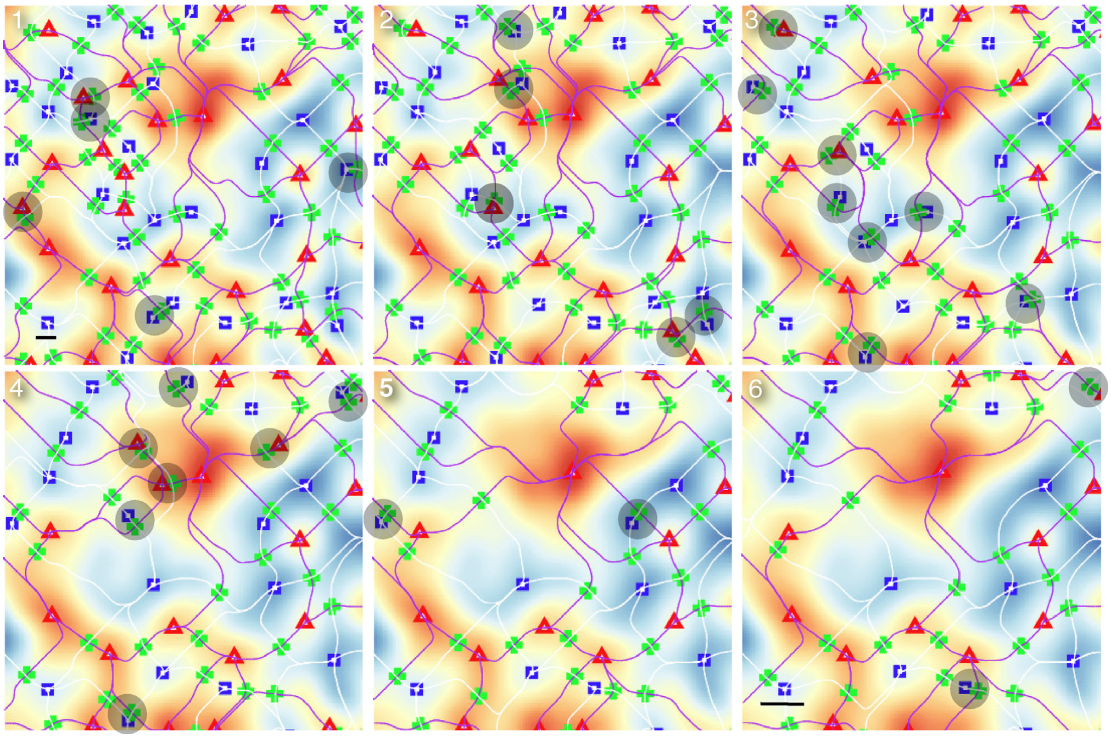

Figure 3. From the left- to right-hand side and top to bottom, a smoothing sequence of a Gaussian random field, whose density is colour coded from blue to red as a function of height (analogous to the slices shown in Fig. 2). The skeleton tracing the ridges (Pogosyan et al. 2009b) is shown in purple, while the antiskeleton tracing the trough is shown in white. The saddles shown as green crosses lie at the intersection. The maxima are shown as red triangles and the minima as blue squares. As one smooths the field, these critical points drift towards each other along the skeletons, until they vanish in (zero persistence) pairs. The upcoming coalescence are identified with grey circles. Note that as saddle points vanish, the two corresponding skeletons also do. Note also that the direction of coalescence is typically set by the skeleton's just before coalescence. In this 2D example, the ratio of peak + saddle to void + saddle event is 1. The black segment in the bottom left-hand panel of the first and last image represents the amount of smoothing. This paper is concerned with studying the one and two-point statistics of these grey circles. Note that these events are indeed proxy for mergers of the peaks of the underlying field: For instance, between snapshots 3 and 5, the central four peaks have merged into one. Similarly, between 1 and 4, the central four voids have merged into one. We provide an interactive tool to follow such events in 2D and 3D.

in the position–smoothing space is given by

$$n_{\rm ce}^{\rm 3D} \equiv \left\langle \sum_{\rm ce} \delta_{\rm D}^{(3)}(\boldsymbol{r} - \boldsymbol{r}_{\rm ce})\delta_{\rm D}(R - R_{\rm ce}) \right\rangle , \tag{9}$$

where $\boldsymbol{r}_{\rm ce}$ is the position of a critical event (i.e. a critical point with a degenerate direction) in real space and $R_{\rm ce}$ its associated smoothing scale, and $\delta_{\rm D}$ is the Dirac function. The brackets in equation (9) denote the 3 + 1D spatial averaging over volume V and scale range ΔR, $\langle \dots \rangle = (V\Delta R)^{-1} \int_{\Delta R} {\rm d}R \int_V \dots {\rm d}^3\boldsymbol{r}$.

In the following, we will use ∂_R to denote derivatives with respect to scale R. Since critical events are characterized by H and $\nabla\delta$, let us rewrite equation (9) in terms of the properties of the field, using the coordinate transformation from $(\boldsymbol{r}, R)$ to $(\nabla\delta, H)$. As pointed out by Musso & Sheth (2019), this involves the 3 + 1D Jacobian of the transformation

$$\begin{aligned} J(H, \nabla\delta) &= \begin{vmatrix} \partial_R H & \nabla H \\ \partial_R \nabla\delta & \nabla\nabla\delta \end{vmatrix}, \\ &= H \left(\partial_R H - \partial_R \nabla\delta \cdot \mathbf{H}^{-1} \cdot \nabla H \right). \end{aligned} \tag{10}$$

The latter expression for the 3 + 1 decomposition of the Jacobian formally requires the Hessian $\mathbf{H}$ to be invertible, which is not the case at the critical event. Still, the Jacobian is well defined even there since the product $H\mathbf{H}^{-1}$ remains finite in the $H \to 0$ limit. Interestingly, the term $\partial_R H$ does not contribute to J since it enters the result only multiplied by the vanishing H.

The fully covariant formulation of the number density of critical events, which generalizes Hanami (2001), is then

$$n_{\rm ce}^{\rm 3D} = \left\langle |J|\, \delta_{\rm D}^{(3)}(\nabla\delta)\delta_{\rm D}(H) \right\rangle, \tag{11}$$

where the brackets now indicate the expectation value over the joint distribution of the field and its successive derivatives up to second order, as well as derivatives of the field gradient with respect to R, $P(x, x_i, x_{ij}, \partial_R x_i)$.

The statistics of $\partial_R \nabla\delta$ variables depend on the choice of filtering function and may be non-local. Its treatment is significantly simplified when filtering with a Gaussian window, in which case the change in the value of the field with R is given by a local quantity via the diffusion-type equation:

$$\partial_R \delta = R\nabla^2\delta, \tag{12}$$

so we can replace the problem by averaging over the one-point distribution of the field and its derivatives up to the third order, $P(x, x_i, x_{ij}, x_{ijk})$. This distribution involves 20 variables; see Appendix G for the PDF for Gaussian random fields. For the calculations that follow, we will use a Gaussian filtering model and equation (12).

It is important to stress now that the 3 + 1D number density of critical events given by equation (11) is not equivalent to the rate of

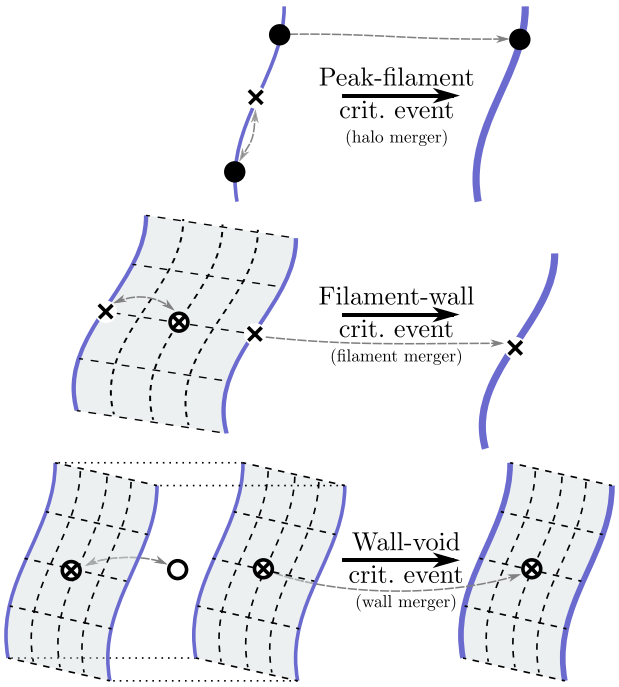

Figure 4. Illustration of critical events in a 3D random field and their physical meaning. ● symbols are peaks, × symbols are filament-type saddle points (filament centres), ⊗ symbols are wall-type saddle points (wall centres), and ○ symbols are minima (void centres). Top panel: Peak-filament critical events encode the merger of two haloes and the disappearance of their shared filament. After the merger, only one peak subsists and the filament disappears. Middle panel: Filament-wall critical events encode the merger of two filaments and the disappearance of their shared wall. After the merger, only one filament subsists. Bottom panel: Wall-void critical events encode the merger of two walls and the disappearance of their joint void (surrounded by the two walls and the dotted lines). After the merger, only one wall-type saddle-point subsists and the void has disappeared. Halo mergers are encoded by peak-filament critical events, filament mergers. Alternatively, one could have chosen to describe these events as, respectively, filament, wall, and void disappearances, while describing the excursion from the low-density end. This is illustrated in Fig. C1.

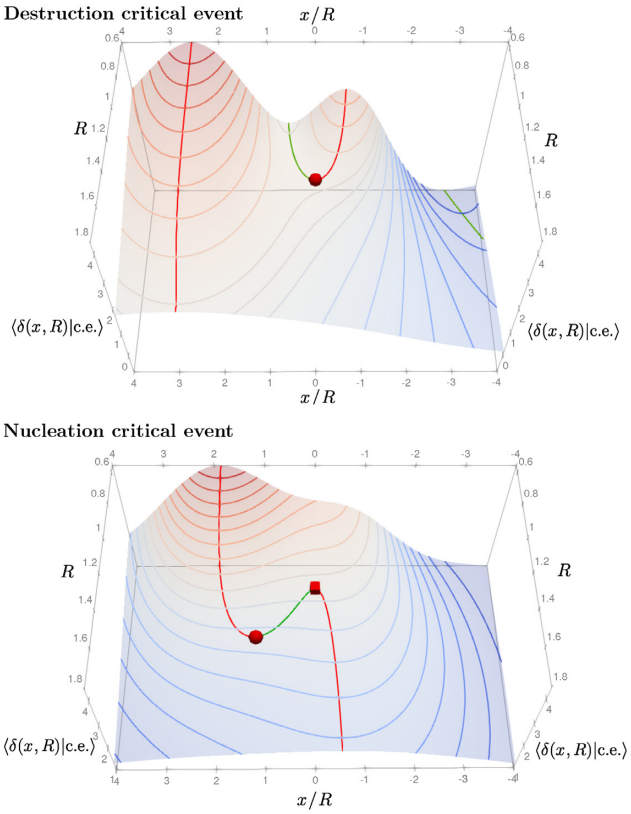

Figure 5. 2D slice, in the (x, R) plane, of the conditional mean density in the 3 + 1D position–smoothing space, under the constraint of a destruction critical event (red sphere, top panel) and a nucleation critical event (red box, bottom panel) at $R = 1$, $x = 0$. The slice position is chosen to contain the events. Green lines show filament-type saddle points at each R and red lines show peaks. Density isocontours are represented as coloured lines (from red, high density to blue, low density). The top panel is reminiscent of Fig. 1, since 3D merger events closely resemble 1D merger events along filaments, while the bottom panel is unique to dimensions larger than one for Gaussian smoothing. An interactive version can be found in the online supplemental material and online. While nucleation events such as that shown on the bottom panel can occur, they statistically seem to remain short-lived and are less frequent than destruction ones.

change with smoothing R of the 3D density of critical point pairs. Indeed, at a critical event, one pair of critical points of adjacent topological types (e.g. maximum and filamentary saddle) coalesce, but as a local analysis in Appendix D demonstrates, this event can describe either the merging or the creation of the pair, depending on the sign of Jacobian J. Namely, the partial number densities,

$$n^{\rm 3D}_{\rm ce,\pm} \equiv \left\langle |J| \Theta_{\rm H}(\pm J)\, \delta_{\rm D}^{(3)}(\nabla\delta)\delta_{\rm D}(H) \right\rangle, \tag{13}$$

such that $n^{\rm 3D}_{\rm ce} = n^{\rm 3D}_{\rm ce,-} + n^{\rm 3D}_{\rm ce,+}$, count separately critical events where a pair of critical points is created (+, also called a nucleation) or destroyed (−). The two kinds are illustrated on Fig. 5, which was generated using the code detailed in Appendix E for two likely configurations. Note however that nucleation critical events are ∼30 times less probable than the destruction critical event (see Fig. F1) for $n_{\rm s} < -1$ ($\gamma \lessapprox 0.8$). The quantity that is equal to the rate of change of the density of critical points with smoothing is, therefore, obtained by removing the absolute value from the Jacobian in equation (11), as shown in Appendix B, which shows that the rate of change of the number density of critical points with smoothing obeys

$$\frac{{\rm d}n_{\rm cp}}{{\rm d}R} = 2\left\langle J\, \delta_{\rm D}^{(3)}(\nabla\delta)\delta_{\rm D}(H) \right\rangle \equiv -2\, n^{\rm 3D}_{\rm me}\,, \tag{14}$$

where we introduced the 'net merger rate' (taken with minus sign) as

$$n^{\rm 3D}_{\rm me} = n^{\rm 3D}_{\rm ce,-} - n^{\rm 3D}_{\rm ce,+}\,. \tag{15}$$

While in this paper the term 'net merger rate' has been chosen for the sake of readability, we must emphasize that this quantity measures rates in the position–smoothing scale space. Care should be taken to relate these mergers to mergers in space–time, as will be discussed in Section 5.1.

2.2.2 *Expression in the frame of the Hessian*

One possible method to yield an analytical expression of equation (14) is to re-express it in the frame of the Hessian, where the Jacobian becomes sparse and can be computed in terms of the field variables. We shall denote the field variables in the eigenframe of the Hessian

with a tilde. In this frame, the diagonal components of the Hessian itself are given by the eigenvalues $\tilde{x}_{ii} = \lambda_i$ with off-diagonal ones being zero $\tilde{x}_{i\neq j} = 0$. The Jacobian is by construction invariant under rotation, so we can rewrite it in the Hessian eigenframe without loss of generality. Developing H into $\sigma_2^3\lambda_1\lambda_2\lambda_3$ and assuming, for instance, that direction 3 is the degenerate one, the Jacobian can be rewritten as follows:

$$\frac{J(H,\nabla\delta)}{\sigma_1\sigma_2^4\sigma_3} = \lambda_1\lambda_2 \begin{vmatrix} \partial_R\lambda_3 & \tilde{x}_{331} & \tilde{x}_{332} & \tilde{x}_{333} \\ \partial_R\tilde{x}_1 & \lambda_1 & 0 & 0 \\ \partial_R\tilde{x}_2 & 0 & \lambda_2 & 0 \\ \partial_R\tilde{x}_3 & 0 & 0 & 0 \end{vmatrix} \tag{16}$$

$$= -(\lambda_1\lambda_2)^2\tilde{x}_{333}\partial_R\tilde{x}_3\,, \tag{17}$$

where the factorization of $\lambda_1\lambda_2$ in equation (16) is a consequence of λ_3 being zero, which also nulls the last component of the last row. Using equation (12) to re-express the derivative with respect to smoothing in terms of the Laplacian of the field, we find the number density of critical events in equation (11) to be[5]

$$n_{\rm ce}^{\rm 3D} = \frac{R}{\tilde{R}^2\,R_*^3}\left\langle |\textstyle\sum_l \tilde{x}_{3ll}||\tilde{x}_{333}|\delta_{\rm D}^{(3)}(\tilde{x}_i)\lambda_1\lambda_2\delta_{\rm D}(\lambda_3)\right\rangle, \tag{18}$$

where $\delta_{\rm D}^{(3)}(\tilde{x}_i)$ is understood as the product of the Dirac delta functions of all components of the gradient of the field. R_* and $\tilde{R}$ are the typical inter-critical point and inter-inflection point separation, respectively, introduced in equation (4).

Let us stress that in equation (18), the averaging is performed over the distribution of the fields expressed in the frame of the Hessian matrix (Doroshkevich 1970) that differs functionally from the distribution in an arbitrary frame. For computational purposes, it is useful to avoid this complication. We achieve this by noticing that in the integral over the Hessian space, the transition to the eigenframe can be introduced using the Dirac delta functions on off-diagonal elements of the Hessian coupled with the Jacobian of the transformation $\propto (\lambda_3-\lambda_1)(\lambda_3-\lambda_2)(\lambda_2-\lambda_1)$ times $2\pi^2$ due to integration over angles of Hessian orientation assuming statistical isotropy. Namely, equation (18) can be cast in the form of an average over the distribution of field variables in an arbitrary frame as

$$n_{\rm ce}^{\rm 3D} = \frac{2\pi^2 R}{\tilde{R}^2\,R_*^3}\Big\langle |\textstyle\sum_l x_{3ll}||x_{333}|\delta_{\rm D}^{(3)}(x_i)x_{11}^2x_{22}^2(x_{22}-x_{11}) \times\Theta_{\rm H}(-x_{22})\Theta_{\rm H}(x_{22}-x_{11})\delta_{\rm D}(x_{33})\delta_{\rm D}^{(3)}(x_{i\neq k})\Big\rangle\,. \tag{19}$$

We can use this expression as is to compute the average $n_{\rm ce}^{\rm 3D}$ over any isotropic distribution given in an arbitrary coordinate frame, since the Hessian eigenframe condition is now enforced explicitly by $\delta_{\rm D}^{(3)}(x_{i\neq k})$, which denotes again a product of Dirac delta functions of all the off-diagonal components of the Hessian matrix, while the Heaviside functions $\Theta_{\rm H}$ enforce the sorting of the Hessian's diagonal elements. Thus, we have dropped the tilde sign from the variables. For compactness, we have given the integrand in a non-rotation invariant form, having used the presence of $\delta_{\rm D}(x_{33})$ in the integral that describes condition of the vanishing third Hessian eigenvalue.

The novelty of equation (19) compared to the classical BBKS formula is the weight $|\sum_i x_{3ii}||x_{333}|$, which requires the knowledge of the statistics of the third-order derivatives of the field. The expectations in equation (19) can be evaluated with the joint statistics of the field and its successive derivatives, $P(x_{113}, x_{223}, x_{333}, x_{11}, x_{22})$, which now only involves five of the variables listed above to average over.

Following the same derivation, one can also compute the net merger rate:

$$n_{\rm me}^{\rm 3D} = \frac{2\pi^2 R}{\tilde{R}^2\,R_*^3}\Big\langle \left(x_{333}\textstyle\sum_l x_{3ll}\right)\delta_{\rm D}^{(3)}(x_i)x_{11}^2x_{22}^2(x_{22}-x_{11}) \times\Theta_{\rm H}(-x_{22})\Theta_{\rm H}(x_{22}-x_{11})\delta_{\rm D}(x_{33})\delta_{\rm D}^{(3)}(x_{i\neq k})\Big\rangle\,. \tag{20}$$

Let us stress here that equations (19) and (20) describe different quantities that were defined in equations (11) and (15), respectively. In equation (20) and in the rest of this paper, the quantity of interest will be the net merger rate.

Note that equation (18) closely resembles the equation giving the flux of critical lines per unit surface presented in Pogosyan et al. (2009b), up to the delta function on the third eigenvalue (and the corresponding Jacobian). It involves the product of the transverse curvatures because the larger those curvatures, the larger the flux of such lines per unit transverse surface. The extra third eigenvalue delta function reflects that we also now require that along the filament's direction the curvature should be flat, whereas they marginalized over all possible longitudinal curvature. The similarity implies that critical points essentially slide along critical lines as one smooths the field; see Fig. 3: In some loose sense, the 3D event count can be approximately recast into a 1D event count along the ridges.

2.3 Gaussian number density of critical events per type

In this section, the number counts are extended to distinguish different critical event types and count them as a function of density. Section 2.3.1 presents the number count of the different types of critical events. Section 2.3.2 presents their number count as a function of their density. Throughout the section, the field will be assumed to be a Gaussian random field.

2.3.1 Different critical events and their mean number density

In the previous example, we chose the largest eigenvalue λ_3 to be vanishing at the critical event, which corresponds to the coalescence of a peak–filamentary saddle pair. Thus, we did not count all possible critical events in equations (19) and (20). While the coalescence of peaks with filaments (PF critical events, the sloping saddles of Hanami 2001) are clearly central to the theory of mass assembly, the coalescence of filament saddles with wall saddles (FW critical events) and of wall saddles with voids (WV critical events) are also likely to affect the topology of galactic infall. FW critical events correspond to the case when the middle eigenvalue λ_2 vanishes, while WV critical events are the ones with the lowest eigenvalue λ_1 being zero.

Let us therefore compute the net merger rate for each type of mergers ($\mathcal{P} \equiv$ PF, $\mathcal{F} \equiv$ FW, and $\mathcal{W} \equiv$ WV) using Gaussian assumption about the density field. For an isotropic Gaussian field, odd- and even-order derivatives of the field at the same point are completely statistically independent. Therefore, equation (20), generalized to the case where any eigendirection can be chosen as a degenerate one, can be split into odd- and even-order derivative

[5]One factor of $\lambda_1\lambda_2$ drops between equations (17) and (18) because of $\delta_{\rm D}(H)$ in equation (11). We also note that $\lambda_1\lambda_2 \geq 0$ when $\lambda_3 = 0$.

terms as[6]

$$n_{\rm me}^{(j)} = \frac{R}{\tilde{R}^2 R_*^3}\, C_{\rm odd}\, C_{j,\rm even}\,, \tag{21}$$

where

$$C_{j,\rm even} = \left\langle 2\pi^2 \delta_{\rm D}(x_{jj}) \Theta_{\rm H}(x_{33}-x_{22}) \Theta_{\rm H}(x_{22}-x_{11}) \right. \\ \left. \times \delta_{\rm D}^{(3)}(x_{k\neq l}) \left| \sum_{kl} \frac{1}{2} \varepsilon^{jkl} x_{kk}^2 x_{ll}^2 (x_{kk}-x_{ll}) \right| \right\rangle, \tag{22}$$

with ε^{jkl} being the completely antisymmetric Levi–Civita tensor and $j = 3$, 2, and 1 for peak, filament, and walls. In turn, the term that involves the odd-order derivatives of the field,

$$C_{\rm odd} = \left\langle \sum_l x_{jll} x_{jjj} \delta_{\rm D}^{(3)}(x_i) \right\rangle, \tag{23}$$

is actually independent on j due to isotropy. In the rest of this paper, we will also make use of the notation $\mathcal{P}$, $\mathcal{F}$, $\mathcal{W}$ instead of $j = 3$, 2, 1 (for peak, filament, and wall mergers, respectively) in formulas with an astrophysical interpretation.

The factors $C_{\rm odd}$ and $C_{j,\rm even}$ that constitute $n_{\rm me}^{(j)}$ are readily evaluated. In 3 + 1D, they are

$$C_{1,\rm even} = C_{3,\rm even} = \frac{29-6\sqrt{6}}{18\sqrt{10\pi}}\,, \quad C_{2,\rm even} = \frac{2}{\sqrt{15\pi}}\,, \tag{24}$$

while common to all merger event types,

$$C_{\rm odd} = \frac{1}{5}\left(\frac{3}{2\pi}\right)^{3/2} (1-\tilde{\gamma}^2)\,. \tag{25}$$

$C_{\rm odd}$ can also be computed in arbitrary dimensions as shown in Appendix A4.

We note that for Gaussian fields, the computation of the total critical event density $n_{\rm ce}$, as well as partial densities of creation and destruction events $n_{\rm ce,\pm}$, differ from the computation of $n_{\rm me}$ only in the $C_{\rm odd}$ term that can also be found analytically for these quantities. The corresponding values are given in Appendix F.

In addition, let us note that the quantities $n_{\rm me}^{(j)}$ correspond to the following changes of the critical point densities:

$$\begin{aligned} {\rm d}n_{\rm cp}^{\rm p}/{\rm d}R &= -n_{\rm me}^{\mathcal{P}}, \quad {\rm d}n_{\rm cp}^{\rm f}/{\rm d}R = -(n_{\rm me}^{\mathcal{P}} + n_{\rm me}^{\mathcal{F}}), \\ {\rm d}n_{\rm cp}^{\rm v}/{\rm d}R &= -n_{\rm me}^{\mathcal{W}}, \quad {\rm d}n_{\rm cp}^{\rm w}/{\rm d}R = -(n_{\rm me}^{\mathcal{F}} + n_{\rm me}^{\mathcal{W}})\,. \end{aligned} \tag{26}$$

Here, superscripts p, f, w, and v denote peaks, filament saddle, wall saddle, and minima, respectively. Thus, for instance, $n_{\rm me}^{\mathcal{P}}$ and the change in the density of peaks ${\rm d}n_{\rm cp}^{\rm p}/{\rm d}R$ both evaluate to

$$n_{\rm me}^{\mathcal{P}} = \frac{3R}{R_\star^3 \tilde{R}^2}(1-\tilde{\gamma}^2)\frac{29\sqrt{15}-18\sqrt{10}}{1800\pi^2}\,. \tag{27}$$

This coincides with the result of Appendix A8, obtained by direct differentiation of $n_{\rm cp}^{\rm p}$.

From equation (24), we can compute the ratio of filament to peak mergers $r_{\mathcal{F}/\mathcal{P}} \equiv n_{\rm me}^{\mathcal{F}}/n_{\rm me}^{\mathcal{P}} = C_{2,\rm even}/C_{3,\rm even}$. Interestingly, the merger event ratio is independent of the spectral index of the field and is given by

$$r_{\mathcal{F}/\mathcal{P}} = \frac{24\sqrt{3}}{29\sqrt{2}-12\sqrt{3}} \approx 2.055\,08\,, \tag{28}$$

which is nothing but the ratio between the mean number of wall-type saddles and peaks minus 1. This relation can be readily obtained also from equation (26) by noting that the relative fraction of different critical points is smoothing-independent, and thus should be, after some algebra, the ratio of their rates of change, e.g. $(n_{\rm me}^{\mathcal{P}} + n_{\rm me}^{\mathcal{F}})/n_{\rm me}^{\mathcal{P}} = n_{\rm cp}^{\rm f}/n_{\rm cp}^{\rm p}$ so that $r_{\mathcal{F}/\mathcal{P}} = n_{\rm cp}^{\rm f}/n_{\rm cp}^{\rm p} - 1$. Equation (28) also shows that there are about twice more filaments disappearing in filament merger events ($\mathcal{F}$ events) than in halo merger events ($\mathcal{P}$ events). Similarly, we can compute $r_{\mathcal{F}/\mathcal{W}}$ to deduce that there are twice as many walls disappearing due to filament mergers ($\mathcal{F}$ events) as due to wall mergers ($\mathcal{W}$ events). Appendix A6 also presents these ratios in dimensions 4–6.

2.3.2 3D differential event counts of a given height

As argued by Press & Schechter (1974) and Bardeen et al. (1986), the initial mean density profile of a proto-object contains information about its future evolution (e.g. the time of collapse). In this section, we therefore extend our previous results by computing the net merger rate in 3 + 1D space as a function of the field height (the overdensity). While the *density-integrated* net merger rates, computed in the previous section, are directly connected to the derivatives of the *density-integrated* number density of critical points through equation (26), the net merger rates at fixed $\nu = \delta/\sigma_0$[7] do not verify such a simple relation, since the field height ν is not preserved along the 3 + 1D trajectory of an individual critical point. In other words, the field height of the critical event is not simply related to the height of its two progenitors. This gives us an additional source of change in the critical point number density at fixed ν. Thus, $n_{\rm me}(\nu)$ is a new statistics, not equivalent to ${\rm d}n_{\rm cp}(\nu)/{\rm d}R$, which focuses specifically on the contribution of mergers to the change of the critical point number density at a given ν. Studying $n_{\rm me}(\nu)$ allows us to make the distinction between mergers of important critical points and less significant ones. In particular, if we identify astrophysical objects by a threshold in ν, we will be able to study the mergers of that particular population.

The differential net merger density as a function of height is obtained by introducing $\delta_{\rm D}(x-\nu)$ in the expectation of equation (21). Under the assumption of a Gaussian random field, the field only correlates with its even-order derivatives (second in this case). Imposing the height of the critical events considered here therefore only modifies the term $C_{j,\rm even}$ while $C_{\rm odd}$ is left unchanged, following

$$C_{j,\rm even}(\nu) = \left\langle \delta_{\rm D}(x-\nu) \delta_{\rm D}(x_{jj}) \Theta_{\rm H}(x_{33}-x_{22}) \Theta_{\rm H}(x_{22}-x_{11}) \right. \\ \left. \times 2\pi^2 \delta_{\rm D}^{(3)}(x_{k\neq l}) \left| \sum_{kl} \tfrac{1}{2} \varepsilon^{jkl} x_{kk}^2 x_{ll}^2 (x_{kk}-x_{ll}) \right| \right\rangle. \tag{29}$$

The net merger density of kind j at height ν, $n_{\rm me}^{(j)}(\nu)$ then reads

$$n_{\rm me}^{(j)}(\nu) \equiv \frac{R}{\tilde{R}^2 R_*^3} C_{j,\rm even}(\nu) C_{\rm odd}. \tag{30}$$

Interestingly, $C_{j,\rm even}(\nu)$ appears to have an analytical expression once rotational invariants are used to evaluate the expectations. Following the formalism described in Pogosyan, Gay & Pichon (2009a), we introduce the variables

$$J_1 = I_1\,, \quad J_2 = I_1^2 - 3I_2\,, \tag{31}$$

[6]From now on, to simplify the notation, we will drop the superscript 3D from the critical event densities where it does not lead to confusion.

[7]Note that here and in the following, ν refers to specific values that the random field x may take.

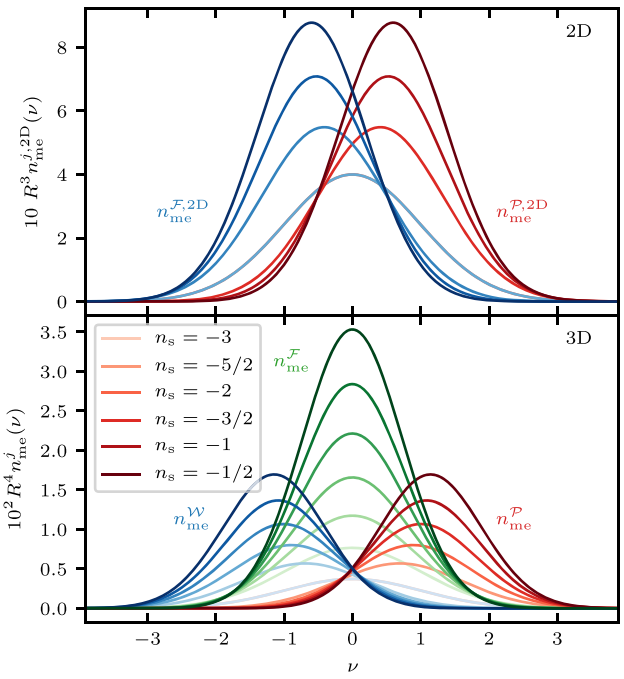

Figure 6. The PDFs of critical events net merger rates of the various types $\mathcal{P}, \mathcal{F}$ in 2D for n_s from -2 to $-1/2$ (top panel) and $\mathcal{P}, \mathcal{F}, \mathcal{W}$ in 3D for n_s from -3 to $-1/2$ (bottom panel), as labelled. Note that the dominant change with spectral index is in the amplitude, which scales like $1/(\tilde{R}^2 R_\star^d)$. The rest of the shape variation comes from the weaker γ and $\tilde{\gamma}$ dependence of $C_{\rm odd}$ and $C_{\rm even}$. In 2D, the $\mathcal{P}, \mathcal{F}$ merger rates coincide for $n_s = -2$ as the field and its second derivatives become uncorrelated ($\gamma = 0$).

$$J_3 = \frac{27}{2} I_3 - \frac{9}{2} I_1 I_2 + I_1^3\,, \quad \zeta = \frac{x + \gamma J_1}{\sqrt{1-\gamma^2}}\,, \tag{32}$$

which are linear combinations of the density field x and rotational invariants of its second derivatives, namely the trace $I_1\sigma_2 = \mathrm{tr}\,\mathbf{H} = \sigma_2(\lambda_1+\lambda_2+\lambda_3)$, minor $I_2\sigma_2^2 = 1/2((\mathrm{tr}\,\mathbf{H})^2 - \mathrm{tr}\,\mathbf{H}\cdot\mathbf{H}) = \sigma_2^2(\lambda_1\lambda_2+\lambda_2\lambda_3+\lambda_3\lambda_1)$ and determinant $I_3\sigma_2^3 = \det\mathbf{H} = \sigma_2^3\lambda_1\lambda_2\lambda_3$ of the Hessian matrix $\mathbf{H}$. The distribution of these variables is given by

$$P(\zeta, J_1, J_2, J_3) = \frac{25\sqrt{10\pi}}{24\pi^2} \exp\left(-\tfrac{1}{2}\zeta^2 - \tfrac{1}{2}J_1^2 - \tfrac{5}{2}J_2\right), \tag{33}$$

where J_3 is uniformly distributed between $-J_2^{3/2}$ and $J_2^{3/2}$ and J_2 is positive. Using these rotational invariants, one can rewrite equation (29) for each type of critical event as

$$C_{3,\rm even}(\nu) = \left\langle \tfrac{1}{3}\left(J_1^2 - J_2\right)^2 \delta_{\rm D}(x-\nu)\delta_{\rm D}(I_3) \times \Theta_{\rm H}(J_1+2\sqrt{J_2})\Theta_{\rm H}(-\sqrt{J_2}-J_1)\right\rangle, \tag{34}$$

$$C_{2,\rm even}(\nu) = \left\langle \tfrac{1}{3}\left(J_2 - J_1^2\right)^2 \delta_{\rm D}(x-\nu)\delta_{\rm D}(I_3) \times \Theta_{\rm H}(J_1+\sqrt{J_2})\Theta_{\rm H}(\sqrt{J_2}-J_1)\right\rangle, \tag{35}$$

$$C_{1,\rm even}(\nu) = \left\langle \tfrac{1}{3}\left(J_1^2 - J_2\right)^2 \delta_{\rm D}(x-\nu)\delta_{\rm D}(I_3) \times \Theta_{\rm H}(J_1-\sqrt{J_2})\Theta_{\rm H}(2\sqrt{J_2}-J_1)\right\rangle, \tag{36}$$

with

$$\delta_{\rm D}(I_3) = \frac{27}{2}\delta_{\rm D}\left(J_3 - \frac{3J_1J_2 - J_1^3}{2}\right), \tag{37}$$

$$\delta_{\rm D}(x-\nu) = \frac{1}{\sqrt{1-\gamma^2}}\delta_{\rm D}\left(\zeta - \frac{\nu+\gamma J_1}{\sqrt{1-\gamma^2}}\right). \tag{38}$$

The condition that the determinant I_3 is null due to specific λ_j being zero is enforced by restricting the range of J_1 according to the product of Heaviside functions, as specified in equations (34)–(36). The integration in equations (34)–(36) can be done analytically and an exact expression for $C_{j,\rm even}(\nu)$ follows

$$\begin{aligned} C_{3,\rm even}(\nu) &= \sum_{i=5,6,9} c_{3,i}\ \exp\left(-\frac{\nu^2}{2\left(1-5\gamma^2/i\right)}\right), \\ C_{2,\rm even}(\nu) &= c_{2,6}\ \exp\left(-\frac{\nu^2}{2(1-5\gamma^2/6)}\right), \\ C_{1,\rm even}(\nu) &= C_{3,\rm even}(-\nu), \end{aligned} \tag{39}$$

with

$$c_{3,5} = \frac{3\sqrt{5}\gamma\nu\sqrt{1-\gamma^2}\left(275\gamma^4 + 30\gamma^2\left(2\nu^2-23\right)+351\right)}{\pi\sqrt{2\pi}\left(9-5\gamma^2\right)^4},$$

$$c_{3,6} = -\frac{\mathrm{erf}\left(\frac{\gamma\nu}{\sqrt{2(1-\gamma^2)(6-5\gamma^2)}}\right)+1}{\sqrt{5}\pi\sqrt{6-5\gamma^2}}, \quad c_{2,6} = \frac{2}{\sqrt{5}\pi\sqrt{6-5\gamma^2}},$$

$$c_{3,9} = \frac{\mathrm{erf}\left(\frac{\sqrt{2}\gamma\nu}{\sqrt{(1-\gamma^2)(9-5\gamma^2)}}\right)+1}{4\pi\sqrt{5}\left(9-5\gamma^2\right)^{5/2}}\left(\frac{3600\gamma^4\nu^4}{(9-5\gamma^2)^2} + \frac{120\gamma^2(27-35\gamma^2)\nu^2}{9-5\gamma^2} + 575\gamma^4 - 1230\gamma^2 + 783\right).$$

The resulting net merger rate as a function of their height ν is plotted in Fig. 6, bottom panel, for different values of the spectral index n_s. Note that $n_{\rm me}^{(j)}(\nu)$ scales like $1/R^4$ but is also a function of R via the spectral parameters γ and $\tilde{\gamma}$. A comparison to measurement in numerically drawn random fields will be presented later in Fig. 11. Note that the mean density of net peak mergers, given by equation (30) for $j = 3$ and equation (39), is equivalent to formula C30 in Hanami (2001).

2.4 2D event counts and differential counts

Given its astrophysical interests when considering 2D maps in various contexts, let us also briefly present the analogues of equation (21) for 2 + 1D fields. It reads

$$n_{\rm me}^{\mathcal{P},2D}(\nu, R) = \frac{-2\pi R}{\tilde{R}^2 R_*^2}\left\langle (x_{211}+x_{222})x_{222}\delta_{\rm D}(x_1)\delta_{\rm D}(x_2)\right\rangle \times \left\langle \Theta_{\rm H}(-x_{11})\delta_{\rm D}(x_{22})\delta_{\rm D}(x_{12})\delta_{\rm D}(x-\nu)x_{11}\right\rangle, \tag{40}$$

where the even part $-2\pi\left\langle\Theta_{\rm H}(-x_{11})\delta_{\rm D}(x_{22})\delta_{\rm D}(x_{12})\delta_{\rm D}(x-\nu)x_{11}\right\rangle$ is nothing but

$$C_{\rm even}(\nu) = \left\langle I_1^2\Theta_{\rm H}(-I_1)\delta_{\rm D}(I_2)\delta_{\rm D}(x-\nu)\right\rangle, \tag{41}$$

once written in terms of the trace I_1 and determinant I_2 of the Hessian matrix.

After some algebra, given the knowledge of the 2D PDF written in Appendix G, we obtain for the peak merger rate

$$n_{\rm me}^{\mathcal{P},\rm 2D}(\nu,R)=\frac{2\pi R C_{\rm odd}^{\rm 2D}}{\tilde{R}^2R_*^2}\left[\frac{4\gamma\nu\sqrt{1-\gamma^2}}{\left(3-2\gamma^2\right)^2}\exp\left(-\frac{1}{2}\frac{\nu^2}{1-\gamma^2}\right)\right.$$
$$+\frac{\sqrt{8\pi}((1-\gamma^2)(3-2\gamma^2)+\gamma^2\nu^2)}{\left(3-2\gamma^2\right)^{5/2}}$$
$$\left.\times\,\mathrm{erfc}\left(\frac{-\gamma\nu}{\sqrt{2(1-\gamma^2)(3-2\gamma^2)}}\right)\exp\left(-\frac{3\nu^2}{6-4\gamma^2}\right)\right], \tag{42}$$

with

$$C_{\rm odd}^{\rm 2D}=\frac{3}{8\pi}(1-\tilde{\gamma}^2)\,.$$

The wall-filament merger rate is obtained by swapping ν to $-\nu$ in equation (42). The two rates are plotted in Fig. 6, top panel, and validated against Gaussian random fields later in Fig. 12. The net merger rate, $n_{\rm me}^{\mathcal{P},\rm 2D}(R)=2C_{\rm odd}R/(3\sqrt{3}\tilde{R}^2R_*^2)$, follows by integration over ν.[8]

Appendix A presents also the differential counts in dimensions 4–6, together with asymptotic expressions in the large dimension limit for the integrated count ratios. As expected, for any dimension, the number counts per unit log-volume are scale invariant (up to the slow variation in the spectral parameters), i.e. $R^d n_{\rm me}^{j,d\rm D}(\nu,R)$ for any $j\in\{1,\ldots,d\}$, is a function of γ, $\tilde{\gamma}$, and ν only.

2.5 Beyond Gaussian statistics

Let us finally compute the one-point statistics for weakly non-Gaussian fields. Following Gay, Pichon & Pogosyan (2012), the Edgeworth expansion around a Gaussian kernel of the joint statistics of the field x and its derivatives, $P(x,x_i,x_{ij},x_{ijk})$ involves the hierarchy of cumulants and reads

$$P(\boldsymbol{x})=P_{\rm G}(\boldsymbol{x})\left(1+\sum_{n=3}^{\infty}\sigma_0^{n-2}\frac{\langle\boldsymbol{H}_n(\boldsymbol{x})\rangle}{\sigma_0^{2n-2}}\cdot\boldsymbol{H}_n(\boldsymbol{x})\right), \tag{43}$$

where $\boldsymbol{x}=(x,x_i,x_{ij},x_{ijk})$, $\boldsymbol{H}_n$ is a vector of orthogonal polynomials[9] with respect to the Gaussian kernel $P_{\rm G}$, obeying $\boldsymbol{H}_n=(-1)^n\partial^n P_{\rm G}/\partial\boldsymbol{x}^n/P_{\rm G}$. At tree level in perturbation theory (Bernardeau et al. 2002), $\langle\boldsymbol{H}_n(\boldsymbol{x})\rangle/\sigma_0^{2n-2}$ is independent of the variance at redshift z, $\sigma_0(z)$, below $n=6$. Cumulants such as $\langle x_1^2x_{113}\rangle$ entering equation (43) could, in the context of a given cosmological model, involve a parametrization of modified gravity (via e.g. a parametrization of the perturbation theory kernel $F_2(\boldsymbol{k}_1,\boldsymbol{k}_2)$), and/or primordial non-Gaussianities (via e.g. the local non-Gaussianity parameter $f_{\rm NL}$), and enable us to study the first stages of the non-linear evolution of the Universe under the action of gravity. From this expansion, or relying on the connection between event ratio and connectivity discussed in Appendix A7, we can, for instance, compute the non-Gaussian correction to the ratio of critical events, defined in equation (28) as

$$\frac{r_{\mathcal{F}/\mathcal{P}}}{r_{\mathcal{F}/\mathcal{P},\rm G}}=1+c_r\left(8\left\langle J_1^3\right\rangle-10\left\langle J_1J_2\right\rangle-21\left\langle J_1q^2\right\rangle\right), \tag{44}$$

where $c_r=(29\sqrt{2}+12\sqrt{3})/210/\sqrt{\pi}$, while $q^2=\sum_i x_i^2=|\nabla\delta|^2/\sigma_1^2$ is the modulus square of the gradient, and J_1 and J_2 are defined in equation (32) via the trace and minor of the Hessian. These extended skewness parameters are isotropic moments of the underlying bispectrum that, when gravity drives the evolution, scale with σ at tree order in perturbation theory (e.g. $\left\langle J_1^3\right\rangle/\sigma_0$ is independent of σ_0). The correction to one entering equation (44) is negative (approximately equal to $-\sigma_0(1/7-\log(R)/5)$ for a Lambda cold dark matter (ΛCDM) spectrum smoothed over $R\,\mathrm{Mpc}\,h^{-1}$), suggesting that gravitational clustering reduces the relative number of peak mergers compared to filament mergers. When astronomers constrain the equation of state of dark energy using the cosmic evolution of voids disappearance, they effectively estimate σ (*via* its dependence in the cumulants) in equation (44). Conversely, for primordial non-Gaussianities, the extended skewness parameters from pure gravitational origin must be updated accordingly (see Gay et al. 2012; Codis et al. 2013). For instance, $\langle J_1q^2\rangle=\langle J_1q^2\rangle_{\rm grav}-2f_{\rm NL}\sqrt{1+f_{\rm NL}^2}/(1+4f_{\rm NL}^2)$.

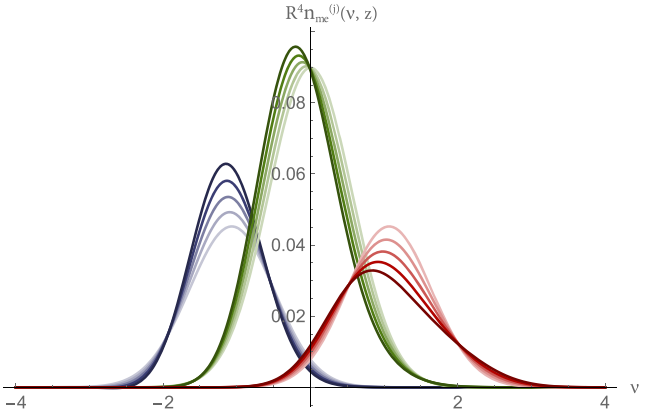

Figure 7. Predicted cosmic evolution of the product of extrema counts as a proxy for the event counts ($\mathcal{W}$ in blue, $\mathcal{F}$ in green, and $\mathcal{P}$ in red) for the variances $\sigma_0(z)=0$, 0.04, 0.08, 0.12, and 0.16 (from light to dark) and an underlying scale invariant power spectrum of index $n=-1$. The $\mathcal{F}$ counts have been rescaled by a constant 205/332 factor to better match the actual counts. The predicted trends with σ_0 are in qualitative agreement with the measured counts presented in Fig. 18.

Since the computation of the expectation (21) with the Edgeworth expansion (43) is beyond the scope of this paper, let us investigate an alternative proxy for the event rate. Fig. 7 makes use of the perturbative prediction of Gay et al. (2012) to first order in σ for the gravitationally driven non-Gaussian differential extrema counts to compute the product of such counts as a proxy for the events, namely $n_{\rm me}^{\mathcal{P}}(\nu,z)\propto n_{\rm cp}^{\rm p}(\nu,z)\times n_{\rm cp}^{\rm f}(\nu,z)$, $n_{\rm me}^{\mathcal{F}}(\nu,z)\propto n_{\rm cp}^{\rm f}(\nu,z)\times n_{\rm cp}^{\rm w}(\nu,z)$, and $n_{\rm me}^{\mathcal{W}}(\nu,z)\propto n_{\rm cp}^{\rm w}(\nu,z)\times n_{\rm cp}^{\rm v}(\nu,z)$. This *ansatz* is reasonable, since for a merger to occur, two critical points of the same height must exist beforehand. We use the Gaussian PDF as a reference, to recalibrate the relative amplitude of the filament to peak merger counts. Since Gay et al. (2012) provide fits to the critical point PDFs as a function of σ_0, it is straightforward to compute their product.

From Fig. 7, we see that gravitational clustering shifts the peak event counts to lower contrast. Less trivially, the filament merger rates also shift towards negative contrasts. From these PDFs, we can re-compute the cosmic evolution of the ratio of critical events, which appears to closely follow $r_{\mathcal{P}/\mathcal{F}}=7/34(1-\sigma_0/7)$ (for $n=-1$), in good agreement with equation (44), suggesting that this approximation indeed captures the main features of gravitational clustering.

[8]The code to reproduce the figures can be found in the online supplemental material and online.

[9]Not to be confused with the Hessian matrix **H** used elsewhere in this paper.

3 THEORY: TWO-POINT STATISTICS OF CRITICAL EVENTS

Let us now present a method to compute the two-point statistics of critical events. Such statistics are of interest, as they allow us to qualitatively understand the upcoming sequencing of processes of importance for galaxy formation, for example, to study the cosmic evolution of the connectivity of peaks, or to understand how large-scale tides bias mass accretion (the so-called assembly bias). Section 3.1 presents the two-point statistics of merger events in 3D, while Section 3.2 provides analytical approximations assuming mergers occur along a straight filament. Section 3.3 computes the conditional merger rates subject to larger scale tides. We match these predictions to simulations in Section 4.

3.1 Clustering of critical events in R, r space

We cannot generally assume that the orientations of two critical events are aligned with respect to the separation vector, so the covariant condition for critical event of type $j \in \{\mathcal{P}, \mathcal{F}, \mathcal{W}\}$, cond_j, is given by the argument of the expectation in equation (14) multiplied by a requirement on the sign of the two non-zero eigenvalues. For instance,

$$\mathrm{cond}_{\mathcal{P}}(\boldsymbol{x}) = J\,\delta_{\mathrm{D}}^{(3)}(x_i)\delta_{\mathrm{D}}(H) \times \Theta_{\mathrm{H}}(-\mathrm{tr}(x_{ik}))\Theta_{\mathrm{H}}(\mathrm{tr}^2(x_{ik}) - \mathrm{tr}(x_{il}x_{lk})),$$

where the two Heaviside conditions ensure that the trace is negative and the minor positive so that the two eigenvalues are negative. Note that we use an implicit sum on repeated indices here. From the joint two-point count of critical events, we can define the relative clustering of critical events of kind i, j smoothed at scales (R_x, R_y) and located at positions $(\boldsymbol{r}_x, \boldsymbol{r}_y)$, $\xi_{ij}(\boldsymbol{s})$ as

$$1 + \xi_{ij}(\boldsymbol{s}) = \frac{\langle \mathrm{cond}_i(\boldsymbol{x}) \times \mathrm{cond}_j(\boldsymbol{y})\rangle}{\langle \mathrm{cond}_i(\boldsymbol{x})\rangle \langle \mathrm{cond}_j(\boldsymbol{x})\rangle}, \tag{45}$$

where $\boldsymbol{x} = \{x, x_i, x_{ij}, x_{ijk}\}$ (respectively, $\boldsymbol{y}$) is the set of fields at location $\boldsymbol{r}_x$ (respectively, $\boldsymbol{r}_y$), and

$$\boldsymbol{s} \equiv \sqrt{2}\left(\frac{\boldsymbol{r}_x - \boldsymbol{r}_y}{\sqrt{R_x^2 + R_y^2}}\right), \tag{46}$$

the event separation that we define as the spatial separation between the two points in units of the quadratic mean smoothing length. We chose this definition as we expect the correlation lengths to be proportional to the smoothing scale; hence, events at different scales can only be meaningfully stacked if distances are expressed in terms of the smoothing length. Because we focus on a Gaussian smoothing, it is natural to associate the two smoothing scales using a quadratic mean as the product of two Gaussian kernels with scales R_x, R_y is equivalent to smoothing at a single scale $R = \sqrt{(R_x^2 + R_y^2)/2}$. Evaluating the expectation in equation (45) requires full knowledge of the joint statistics of the field $P(\boldsymbol{x}, \boldsymbol{y})$ (involving 40 variables; see Appendix G2).

We rely on Monte Carlo methods in MATHEMATICA in order to evaluate numerically equation (45). Namely, we draw random numbers from the conditional probability that $\boldsymbol{x}$ and $\boldsymbol{y}$ satisfy the joint PDF, subject to the condition that $x_j = y_j = 0$, $x = \nu_1$, and $y = \nu_2$. For each draw $(\boldsymbol{x}^{(\alpha)}, \boldsymbol{y}^{(\alpha)})$, $\alpha = 1, \ldots, N$, we drop or keep the sample, depending on the type of critical event given by the signs of $\mathrm{tr}(x_{ij})$ and $\mathrm{tr}^2(x_{ij}) - \mathrm{tr}(x_{il}x_{lj})$; if it is kept, we evaluate

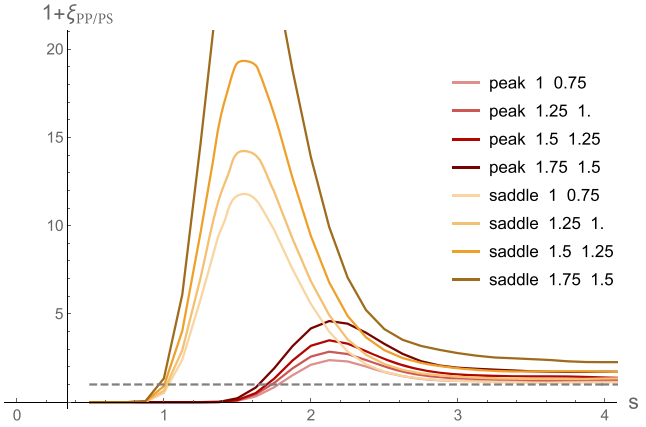

Figure 8. The autocorrelation of peak merger $\xi_{\mathcal{PP}}$ (in shades of red, as labelled in terms of the height of the two critical points) and the cross-correlation of peak and filament merger $\xi_{\mathcal{PF}}$ (in shades of yellow, as labelled) as a function of separation s. As expected, the saddle mergers are clustered closer to the higher peak compared to the peak mergers.

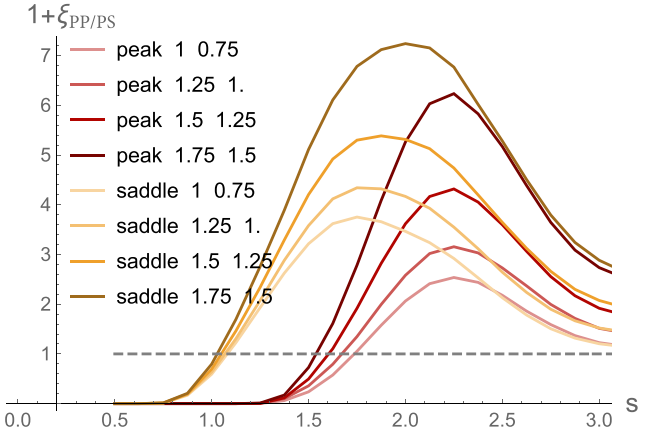

Figure 9. Same as Fig. 8 for the two-point correlation of events in 2D fields with scale-invariant power spectrum of index $n_{\mathrm{s}} = -1$. Next, filament mergers will occur before next peak mergers. The rarer the event, the more delayed, and the higher the clustering amplitude.

$J(\boldsymbol{x})\delta_{\mathrm{D}}^{(\epsilon)}(H(\boldsymbol{x}))\,J(\boldsymbol{y})\delta_{\mathrm{D}}^{(\epsilon)}(H(\boldsymbol{y}))$, where $\delta_{\mathrm{D}}^{(\epsilon)}$ is a normalized Gaussian of width ϵ, which in the limit of $\epsilon \to 0$ would correspond to a Dirac function, imposing here that the two determinants are zero. For small enough ϵ, we then have

$$\langle \mathrm{cond}_i(\boldsymbol{x})\mathrm{cond}_j(\boldsymbol{y})\rangle \approx \frac{P_m(x = \nu_1, y = \nu_2, x_l = y_l = 0)}{N} \sum_{k \in \mathcal{S}_{ij}} J(\boldsymbol{x}^{(k)})\delta_{\mathrm{D}}^{(\epsilon)}\left(H(\boldsymbol{x}^{(k)})\right) J(\boldsymbol{y}^{(k)})\delta_{\mathrm{D}}^{(\epsilon)}\left(H(\boldsymbol{y}^{(k)})\right), \tag{47}$$

where N is the total number of draws, P_m is the marginal probability for the field values and its gradients, and $\mathcal{S}_{ij}$ is the subset of the indices of draws satisfying the constraints i, j on the Hessians. The same procedure can be applied to evaluate the denominator of equation (45), which then yields an estimation of $\xi_{ij}(s, \nu_1, \nu_2)$. This algorithm is embarrassingly parallel.

The results of the numerical integrations are presented in Figs. 8 and 9 (in 3D and 2D respectively) which show the autocorrelation of

peak merger $\xi_{\mathcal{PP}}$ on the one hand, and the cross-correlation of peak and filament merger $\xi_{\mathcal{PF}}$ on the other hand at fixed merger height, as labelled. Here we used $\epsilon = 0.002$. Note that because equation (45) is a ratio, the prefactors in the counts involving scales all cancel out.

3.2 Correlation of peak mergers along filament

Let us briefly present the two-point statistics of high-density peak mergers while assuming for simplicity that the mergers occur along the same (straight) filament (discussed in Section 2.2), as it is instructive and simpler. In this approximation, we can resort to 1D statistics. In the high-density limit, we may drop the Heaviside constraint on the sign of the eigenvalues since all high-density critical points tend to be automatically maxima. Then the (1D) correlation function of peak mergers, $1 + \xi_{\nu_1\nu_2}(s)$ of height ν_1 and ν_2 becomes

$$\frac{\langle \delta_{\rm D}(x-\nu_1) x_{111}^2 \delta_{\rm D}(x_1)\delta_{\rm D}(x_{11})\, \delta_{\rm D}(y-\nu_2) y_{111}^2 \delta_{\rm D}(y_1)\delta_{\rm D}(y_{11})\rangle}{\langle \delta_{\rm D}(x-\nu_1) x_{111}^2 \delta_{\rm D}(x_1)\delta_{\rm D}(x_{11})\rangle \langle \delta_{\rm D}(y-\nu_2) y_{111}^2 \delta_{\rm D}(y_1)\delta_{\rm D}(y_{11})\rangle},$$

where the expectation is over the Gaussian PDF whose covariance for the field $(x, x_1, x_{11}, x_{111}, y, y_1, y_{11}, y_{111})$ obeys

$$\begin{pmatrix} 1 & 0 & -\gamma & 0 & \gamma_{00} & \gamma_{01} & \gamma_{02} & \gamma_{03} \\ 0 & 1 & 0 & -\tilde{\gamma} & -\gamma_{01} & \gamma_{11} & \gamma_{12} & \gamma_{13} \\ -\gamma & 0 & 1 & 0 & \gamma_{02} & -\gamma_{12} & \gamma_{22} & \gamma_{23} \\ 0 & -\tilde{\gamma} & 0 & 1 & -\gamma_{03} & \gamma_{13} & -\gamma_{23} & \gamma_{33} \\ \gamma_{00} & -\gamma_{01} & \gamma_{02} & -\gamma_{03} & 1 & 0 & -\gamma & 0 \\ \gamma_{01} & \gamma_{11} & -\gamma_{12} & \gamma_{13} & 0 & 1 & 0 & -\tilde{\gamma} \\ \gamma_{02} & \gamma_{12} & \gamma_{22} & -\gamma_{23} & -\gamma & 0 & 1 & 0 \\ \gamma_{03} & \gamma_{13} & \gamma_{23} & \gamma_{33} & 0 & -\tilde{\gamma} & 0 & 1 \end{pmatrix}, \tag{48}$$

where, for instance, $\gamma_{02}(s) = \langle x(\boldsymbol{r}_x) y_{11}(\boldsymbol{r}_y)\rangle$. The dominant contribution in the large threshold ν_1, $\nu_2 \gg 1$, large separation $s \gg 1$ regime reads

$$\xi^0_{\nu_1\nu_2}(s) = \frac{\nu_1\nu_2\,(\gamma_{00}(s) + \gamma\,(2\gamma_{02}(s) + \gamma\gamma_{22}(s)))}{\left(1-\gamma^2\right)^2}, \tag{49}$$

which as expected scales like the underlying correlation, $\gamma_{00}(s)$, boosted by the bias factor $\nu_1\nu_2$ (Kaiser 1984). In that limit, the next-order correction to the correlation function involving the third derivative of the field reads

$$\xi^1_{\nu_1\nu_2}(s) = \frac{2\left(\tilde{\gamma}^2\gamma_{11}(s) + 2\tilde{\gamma}\gamma_{13}(s) + \gamma_{33}(s)\right)^2}{\left(1-\tilde{\gamma}^2\right)^2}, \tag{50}$$

where $\tilde{\gamma}$-weighted linear combination of the autocorrelation of $\nabla\Delta\delta$ and the cross-correlation of $\nabla\nabla^2\delta$ and $\nabla\delta$ appear, evaluated at events separated by s. The assumption of successive mergers of peaks occurring along a straight filament is of course very simplified, and prevents us from considering cross-correlations between peak mergers and, for example, filament mergers.

3.3 Conditional merger rates in the vicinity of larger tides

In the context of galaxy formation, it is of interest to quantify conditional merger rates subject to tides imposed by the large-scale structure to explain geographically the origin of assembly bias. To do so one must compute the conditional event counts, subject to a given large-scale critical point at some distance $\boldsymbol{s}$ from the running point $\boldsymbol{x}(\boldsymbol{r}_x)$. The critical point can be e.g. a peak of a given geometry and height, if one is concerned with the impact of clusters on mergers trees of dark matter haloes in their vicinity (Hahn et al. 2009; Ramakrishnan et al. 2019), or it could be a saddle point, as a proxy for a larger scale filament, when studying how haloes growth stalls in such vicinity (Borzyszkowski et al. 2017; Musso et al. 2018). In turn, this involves the joint expectation,

$$\langle \mathrm{cond}_j(\boldsymbol{x})\, \delta_{\rm D}(y_i) |\det y_{ij}|\rangle\,. \tag{51}$$

Evaluating equation (51) requires the full knowledge of the joint statistics of the field at $\boldsymbol{x}(\boldsymbol{r}_x)$ and $\boldsymbol{y}(\boldsymbol{r}_y)$, $P(x, x_i, x_{ij}, x_{ijk}, y, y_i, y_{ij})$ (involving 30 variables). The correlations of the PDF involves the covariance of the field and its derivatives computed at two smoothing scales, R and $R_{\rm c}$ corresponding to the proxy for the timeline of the haloes and the large-scale structure, respectively. We can then marginalize over all variables, subject to, for example, imposing the height, $\nu_{\rm c}$, and shape, μ_i^c, of the large-scale critical point:

$$\langle \mathrm{cond}(\boldsymbol{x})\delta_{\rm D}(y_i)|\det y_{ij}|\delta_{\rm D}(x-\nu)\delta_{\rm D}(y-\nu_{\rm c})\Theta_{\rm H}(-\lambda_i)\delta_{\rm D}(\mu_i-\mu_i^c)\rangle,$$

where λ_i are the eigenvalues of x_{ij} and μ_i are the eigenvalues of y_{ij}. The conditions imposed by the mergers and the properties of the peaks and large-scale environment reduce the number of integrals from 30 to 21. Appendix E describes how to sample conditional event counts using constrained realizations of Gaussian random fields.

For the sake of simplicity, let us restrict computation to the conditional merger rates in 2D. Fig. 10 presents the excess probability of having a peak/filament merger at some distance r and orientation θ with respect to the frame set by a given critical point. Two configurations and types of events are considered. As expected, the tides impact merger rates. While it is beyond the scope of this paper to explore systematically all possible geometries and relative heights, let us stress that such two-point functions are physically very informative: For instance, the bottom panel is an indication of the early disappearance of filaments perpendicular to a wall embedding a filament, which seems qualitatively consistent with what is observed in N-body simulations.

4 MEASUREMENTS FOR GAUSSIAN RANDOM FIELDS

Let us validate the theory while counting critical events within realizations of Gaussian random fields. We then bin them to estimate their one and two-point statistics.

4.1 Method

For each power-law power spectrum $P_k(k) = k^{n_{\rm s}}$, with spectral index $n_{\rm s} = -2$, -1.5, -1, and -0.5, we have generated 250 Gaussian random fields. We have also generated 400 Gaussian random fields with a ΛCDM power spectrum using `mpgrafic` (Prunet et al. 2008) in a Planck Collaboration VI (2018a) cosmology generated using the Eisenstein & Hu (1999) fitting formula. Each realization will henceforth be called a 'cube'. Each cube has a size of 256^3 pixels and a physical extent of 100 Mpc h^{-1}.[10] Each cube has been smoothed using a Gaussian filter with scale ranging from 1 to 20 Mpc h^{-1} (2.56 pixel to 51.2 pixel). The smoothing was operated in Fourier space, assuming periodic boundary conditions. At each scale, all critical points are detected (maxima, minima, and saddle points) using the method detailed in Appendix H1. The critical events are then detected by matching cubes of different smoothing scales using the method detailed in Appendix H2.

Additionally, we have generated 200 2048^2 cubes with a power-law power spectrum with spectral index $n_{\rm s} = -1$ and a physical box

[10]The box size is only relevant in the ΛCDM case, as the power-law cases are scale invariant.

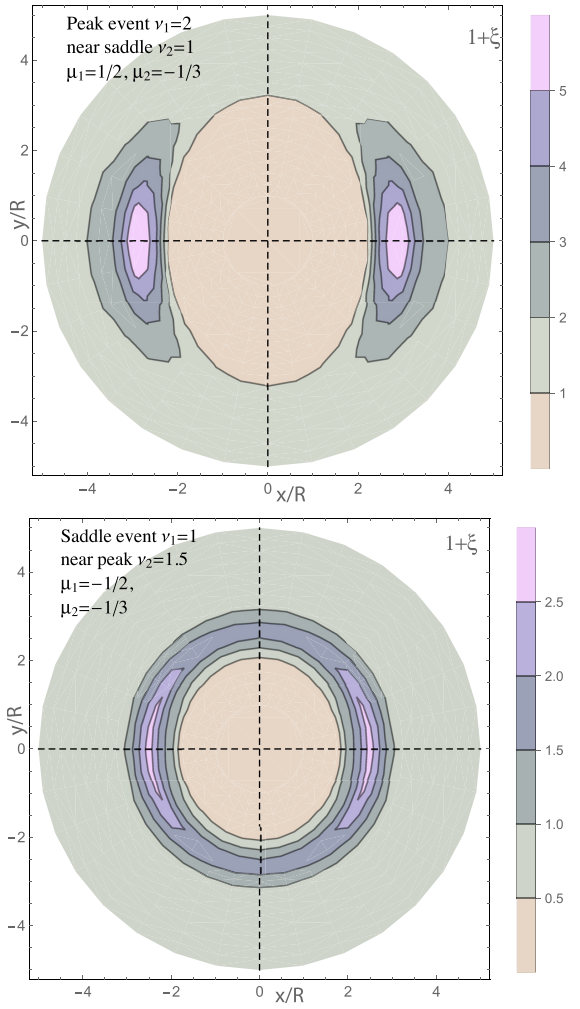

Figure 10. Theoretical prediction for the conditional excess probability, $1 + \xi$, of peak merger events in the frame of a 2D critical point at the origin as labelled. The critical point defines a local exclusion zone whose geometry is set by its fixed eigenvalues. For simplicity, we have chosen $R_c = R$, while the underlying power spectrum index is −1. See Fig. 17 for *measured* 3D counterparts.

size of 1000 Mpc h^{-1}, which we smoothed with a Gaussian filter with scale ranging from 1 to 20 Mpc h^{-1}.

4.2 Critical events counts

In this section, we present the number density of critical events measured in cubes with a power-law power spectrum and compare the theoretical predictions of Section 2.3.2 to measurements in cubes.

We first measured the ratio of the number of critical events of different kind. We found $r_{\mathcal{F}/\mathcal{P}} = r_{\mathcal{F}/\mathcal{W}} \approx 2.1$, regardless of the smoothing scale or the underlying power spectrum. This excess of about 2 per cent in the ratio originates from a slight overdetection of saddle points with respect to local extrema. Theory predicts this ratio to be $N_{\rm saddle}/N_{\rm peak} \approx 3.055$ in 3D (see e.g. Codis, Pogosyan & Pichon 2018, equation 2), while the measured value is 3.1. In the rest of this paper, we have corrected the excess number density of $\mathcal{F}$ critical events so that the number density ratio matches the prediction.

Let us now proceed to the number count at fixed density. Fig. 11 shows the PDF of the critical events as a function of their height

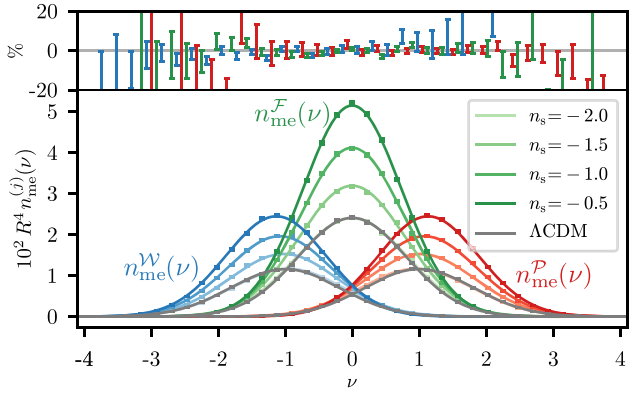

Figure 11. PDF of the critical events as a function of height in a scale-invariant GRF (Gaussian random field) as labelled. The left-hand bundle corresponds to wall mergers, the middle bundle to filament mergers, and the right-hand bundle to peak mergers. The solid curve corresponds to the theory while the error bars correspond to the error on the mean extracted from 160 simulations. The grey lines are the results obtained for a ΛCDM power spectrum initially smoothed over a scale of 2.5 Mpc h^{-1}. The top panel shows the residuals for $n_s = -2$. The detection algorithm is still accurate in 3D.

for different power-law spectra ($n_s = -2$, -1.5, -1, and -0.5; ΛCDM). The critical events have been selected at scale $2.35 \leq R \leq 3.01$ Mpc h^{-1} ($6.0 \leq R \leq 7.7$ pixel). The lower boundary ensures that the critical points are well separated.[11] The upper boundary is fixed so that the smoothed cubes have consistent effective spectral parameters $\gamma_{\rm eff}(R)$ and $\tilde{\gamma}_{\rm eff}(R)$. Indeed, the cubes have scale-dependent spectral parameters induced by the finiteness of the box and the discreteness of the grid (see e.g. Gay 2011, figure 5.1). Error bars have been estimated using a bootstrap method on 400 subsamples each made of 50 randomly chosen cubes. Solid lines show the result of a fit of the theoretical formula to the cube data with free parameters $\hat{\gamma}, \hat{\tilde{\gamma}}$.

The effective spectral index $\hat{n}_s$ is fixed using $\gamma = \sqrt{(n_s+3)/(n_s+5)}$. The measured values of γ and $\tilde{\gamma}$ are consistent with the effective values measured directly in the cubes using equation (6). For example with $n_s = -2$, the values measured in the cubes are $\gamma_{\rm eff} = 0.62 \pm 0.02$, $\tilde{\gamma}_{\rm eff} = 0.72 \pm 0.01$ ($n_{s,\,\rm eff} = -1.75 \pm 0.13$) using equation (6). The mean values have been estimated with a sample of 100 cubes and the errors are the standard deviations of the sample. The fitting procedure on the PDF of the critical events yields $\hat{\gamma} = 0.621 \pm 0.002$, $\hat{\tilde{\gamma}} = 0.724 \pm 0.003$ ($\hat{n}_s = -1.75 \pm 0.02$). The relative difference between theory and measurements, presented on the upper panel of Fig. 11, shows no systematic deviation of the measurements and is within a few per cent in the region where most of the events are.

In order to further test the theoretical prediction, we have proceeded to the same analysis in the 2D case. The results are presented in Fig. 12 and show that the agreement between theory and measurements is of the order of the per cent. Once again, no systematic deviation of the measurements is noted. The results in 2 + 1 and 3 + 1D confirm the analytical formula derived in Section 2.3.2 and illustrate the accuracy of the detection algorithm presented in Appendix H. Interestingly, since the algorithm has been designed to

[11] Critical points are typically separated by $R_* \gtrsim 0.6R$ (for $n_s < 0$), so $R = 6$ pixel gives a typical separation of 3.6 pixel between critical points, which is larger than the number of points used to infer the curvature.

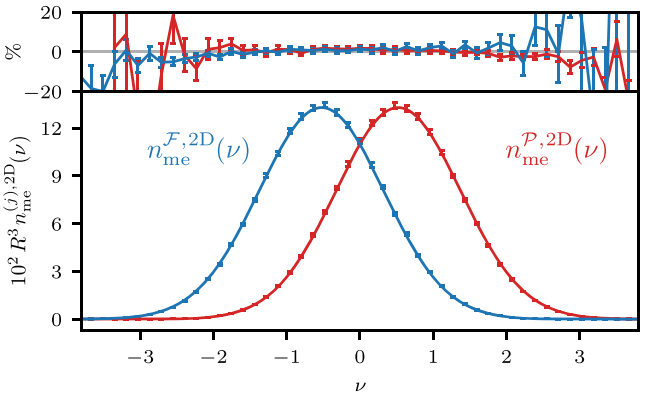

Figure 12. PDF of the critical events as a function of height in a scale-invariant GRF in 2D with spectral index $n_s = -1$. The left-hand curve corresponds to filament mergers and the right-hand curve to peak mergers. The solid curve correspond to the theory while the error bars correspond to the error on the mean extracted from 200 simulations. The top panel shows the residuals. The agreement between the analytic prediction and the measurements reflects the accuracy of the algorithm presented in Appendix H for identifying critical events.

make no assumption on the number of dimensions, it is expected to work as well in d dimensions.

4.3 Two-point statistics

Let us now estimate the two-point statistics of critical events using the critical events from the cubes presented above. For each cube in the simulation, we select all critical events in a thick slice of smoothing scales ($\Delta R/R = 0.3$). The critical events are then split in two subsamples, the first is selected at an overdensity $\nu = 1$ with kind j and the second at $\nu = 0.7$ with kind k ($j, k \in \{\mathcal{P}, \mathcal{F}, \mathcal{W}\}$). The correlation functions are then computed from the number of pairs at distance $s = r/R$ in all cubes. The pair counting was done using a dual-tree algorithm, as described in Moore et al. (2001).[12]

Fig. 13 shows the measured correlation functions in 2D for a power-law power spectrum with spectral index $n_s = -1$ (top panel) and in 3D with a ΛCDM power spectrum smoothed at scales between 1 and 20 Mpc h^{-1} (bottom panel). In both cases, the $\mathcal{PF}$ cross-correlation function (peak merger to filament merger correlation) peaks at $r \approx 1.5R$, while the $\mathcal{PP}$ autocorrelation function (peak merger autocorrelation) peaks at $r \approx 2.1R$. This indicates that each halo merger is more likely to be followed by a filament merger compared to another halo merger. Interestingly, peak mergers are also more likely to be followed by wall mergers. Indeed, a halo merger induces a topological defect, as it leads to a resulting overconnected halo. The defect is quickly corrected by a filament merger, decreasing the local connectivity of the halo back towards the cosmic average. Doing so, another topological defect appears as a void becomes underconnected as one of its walls disappeared. This last defect is then corrected by a last wall merger that makes the underconnected void disappear. Note that, while the above sequence of critical events is a possible one, other sequences are possible that leave the connectivity conserved. On average, critical events happen so that the local ratio of peak-to-filament, filament-to-wall, and wall-to-void stays constant as smoothing increases, so that the global connectivity

[12]See the SCIPY doc for more information.

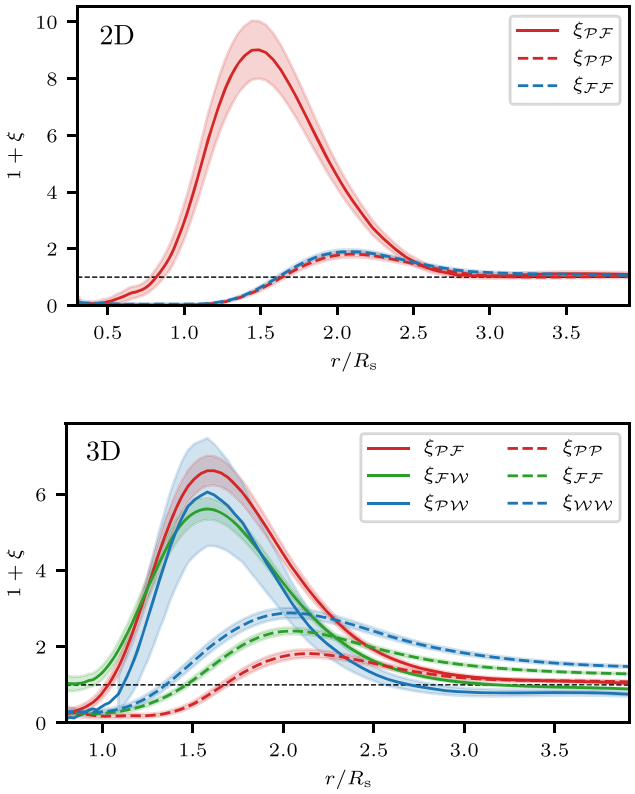

Figure 13. Top panel: correlation functions between critical events $\mathcal{P}$, $\mathcal{F}$ in 2D at fixed smoothing scale for $n_s = -1$. Bottom panel: correlation functions between critical events $\mathcal{P}$, $\mathcal{F}$, $\mathcal{W}$ in 3D at fixed smoothing scale for a ΛCDM power spectrum. Pairs of critical events have been selected at $\nu = 0.7$ and 1.0. The correlation function of halo merger with filament merger, $\xi_{\mathcal{PF}}$, peaks at $r \sim 1.5R$, while the halo merger autocorrelation function, $\xi_{\mathcal{FF}}$, peaks at $r \sim 2R$. This shows that halo mergers are more likely to be followed by filament mergers. The data have been filtered using a Savgol filter. Error bars have been estimated assuming a Poisson noise on the sample.

is preserved. The link between critical events and global connectivity of the cosmic web is further discussed in Section 5.2.

5 APPLICATIONS AND DISCUSSION

The scope of application of the present formalism is obviously very wide. Rather than attempting to cover it all, only a few examples will be presented, while a more thorough investigation is left for future work.

In a cosmic framework, Section 5.1 will first translate the one-point statistics presented in the previous section into destruction rates as a function of mass and redshift. Section 5.2 explains how mergers of filaments need to match that of haloes in order to preserve the connectivity of peaks. Section 5.3 explains how conditional merger counts in the vicinity of a filament explains how the environment drives assembly bias. Section 5.4 compares theoretical predictions of the destruction rates to results from N-body simulations and shows that the theory is able to reproduce the early non-linear stages of gravitational collapse. Finally, Section 5.5 presents an illustration of a correspondence between two critical events and mergers of walls and filaments in N-body simulations, while applications to other fields of research in cosmology (semi-analytical models, machine learning, intensity mapping) and beyond are discussed.

5.1 Destruction rates as a function of mass and time

The predictions in the initial Lagrangian space bear theoretical interest, yet they do not translate easily into measurable quantities. In this section, let us show how one can map these predictions to observable quantities, and in particular destruction rates in mass M and redshift z space. Qualitatively, each critical event encodes a merger that involves three proto-structures (e.g. two proto-haloes and their shared proto-filament). In the rest of this section, we will show that it is possible to relate the mass and the destruction time of the disappearing structure[13] to the density and smoothing scale of the field at the same location.

Together with the results of Section 2.3, one can then compute the destruction rates at different epochs for different object masses. When dealing with void mergers, we will in this section use the dual interpretation of critical events from the point of view of the low-density objects (see Fig. C1). One can use the spherical collapse model to establish a mapping between collapse time of spherical regions and their initial overdensity – high-overdensity regions collapse earlier in the history of the Universe than lower densities. At the same time, larger overdensities enclose more mass and will hence give birth to more massive structures. These relations mathematically read

$$\nu_{\rm TH}(R) = \frac{\delta_{\rm c}}{\sigma_{\rm TH}(R)D(z)}, \quad M = \frac{4\pi}{3}\bar{\rho}R^3, \tag{52}$$

where $\sigma_{\rm TH}(R)$ is the variance of the field smoothed by a Top-Hat filter on scale R, $\delta_{\rm c} = 1.69$ is the spherical collapse critical overdensity, $D(z)$ is the linear matter growth function, and $\bar{\rho}$ is the mean matter density of the Universe. The spherical collapse threshold can also be adapted to study the formation of voids (Sheth & van de Weygaert 2004; Jennings, Li & Hu 2013) with $\delta_{\rm v} = -2.7$. Note that this simple relation holds in principle for small enough voids only ($R \lessapprox 3\,{\rm Mpc}\,h^{-1}$).

From a theoretical perspective, the action of smoothing the density field δ enables to probe the time evolution of spherical proto-haloes by following the density evolution of peaks as the smoothing scale increases. In order to match the results of equation (52) with a Gaussian filter, one needs to establish a mapping of the smoothing scales between Top-Hat filtering and Gaussian filtering. This can be achieved by matching the variance of the field smoothed with a Gaussian filter $\sigma_{\rm G}(R/\alpha) = \sigma_{\rm TH}(R)$, although different approaches have been used.[14] Without loss of generality, equation (52) becomes for a Gaussian filter and a prescription for the value of α:

$$M = \frac{4\pi}{3}\bar{\rho}(\alpha R)^3. \tag{53}$$

This means that the volume associated to a Gaussian filter is equivalent to the volume associated with a Top-Hat filter (a sphere) with an effective size α times larger.

It is now straightforward to change variable from R to M and from ν to z using the spherical collapse condition with a Gaussian filter (equations 52 and 53), so that for condition c (peak or void),[15] the destruction rate reads

$$\left.\frac{\partial^2 n}{\partial \log M \partial z}\right|_c = n_{\rm me}^{(c)}(R,\nu)\frac{\partial R}{\partial \log M}\left|\frac{\partial \nu}{\partial z}\right|,$$
$$= -n_{\rm me}^{(c)}(R,\nu)\frac{|\delta_{\rm c}|}{3\alpha\sigma(R)D(z)^2}\frac{{\rm d}D}{{\rm d}z}\left(\frac{3M}{4\pi\bar{\rho}}\right)^{1/3}, \tag{54}$$

where $\alpha \approx 2.1$ and $\bar{\rho} \approx 2.8 \times 10^{11}\,h^2{\rm M}_\odot/{\rm Mpc}^3\,\Omega_{\rm m}$ (see e.g. Musso et al. 2018, table A1). From equations (30) and (54), we can now count explicitly how many peaks and voids of a certain mass or within some mass range are destroyed early or late in the accretion history, *via* straightforward integration.

Fig. 14 shows the destruction rate of peaks and voids as a function of the object mass. The cosmology-dependent terms of equation (54) ($D(z)$, ${\rm d}D/{\rm d}z$, and σ) have been computed using the code COLOSSUS (Diemer 2018) in a ΛCDM cosmology. The power spectrum has been computed using the fitting formulas of Eisenstein & Hu (1998). In order to evaluate the number density of critical events (the $n_{\rm me}$ term), we have assumed a scale-dependent equivalent power-law power spectrum.[16] The figure shows that for both peaks and voids, there is a cut-off mass scale above which objects are not destroyed any more.

The high-mass cut-off comes from the exponential cut-off of high $|\nu|$ objects, which suppresses massive objects (high R) at high redshifts. Due to the dependence of the destruction rate to the effective spectral index of the power spectrum as well as $\sigma(R)$, the destruction rates show significant redshift evolution. This is particularly emphasized on Fig. 14, right-hand panel, which shows the evolution of the destruction rate with mass at different redshifts. The evolution with redshift both depends on the rarity of the object, as encoded by ν but also on the local shape of the power spectrum, as encoded by the equivalent spectral index $n_{\rm s,\,eq}$.

Quantitatively, it should be noted that the mass scale of the cut-off and the precise value of the merger rate–mass relation will be subject to the same uncertainty in the value of $\delta_{\rm c}$, which also affects the halo mass function (Robertson et al. 2009; Ludlow, Porciani & Borzyszkowski 2014). The focus of this section is anyway to rephrase the critical event theory in astrophysical variables: The implementation of realistic merger tree models is left for future work. It should also, in principle, be possible to generalize equation (54) to filament mergers, but this would require the knowledge of a relation between the initial overdensity (or any other functional of the initial overdensity field) and the mass of the filament or its length, as well as a collapse condition. Shen et al. (2006) and Pogosyan et al. (1998) suggested this could be achieved using a spherical collapse criterion with a critical overdensity smaller than $\delta_{\rm c}$.

The impact of our results on filament merger rates in M, z space will be done in a follow-up work. Beyond the scope of this paper, those results could also be re-expressed in terms of the surviving structure and take into account the two objects' mass ratio, so that they can be compared to merger ratios measured in numerical simulations (e.g. Genel et al. 2009; Fakhouri, Ma & Boylan-Kolchin 2010; Rodriguez-Gomez et al. 2015).

5.2 Consistency with cosmic connectivity evolution

The properties of the initial random field was shown by Codis et al. (2018) to control to a large extent the connectivity of dark matter

[13] For halo mergers spotted by critical events, the disappearing halo is likely to be, but not necessarily, the less massive of the two proto-haloes.

[14] Possible prescriptions include matching $\langle\delta_{\rm TH}\delta_{\rm G}\rangle = \sigma^2_{\rm TH}$ or matching masses $M_{\rm G} = M_{\rm TH}$.

[15] Since ${\rm d}D{\rm d}z = -Df/(1+z)$ with $f \equiv {\rm dlog}\,D/{\rm dlog}\,a \sim \Omega_{\rm m}^{0.6}$.

[16] At each scale, the equivalent power-law power spectrum is given by the formula $n_{\rm s,\,eq}(R) = -3 - 2{\rm dlog}\,\sigma/{\rm dlog}\,R$, where σ is computed using a ΛCDM power spectrum.

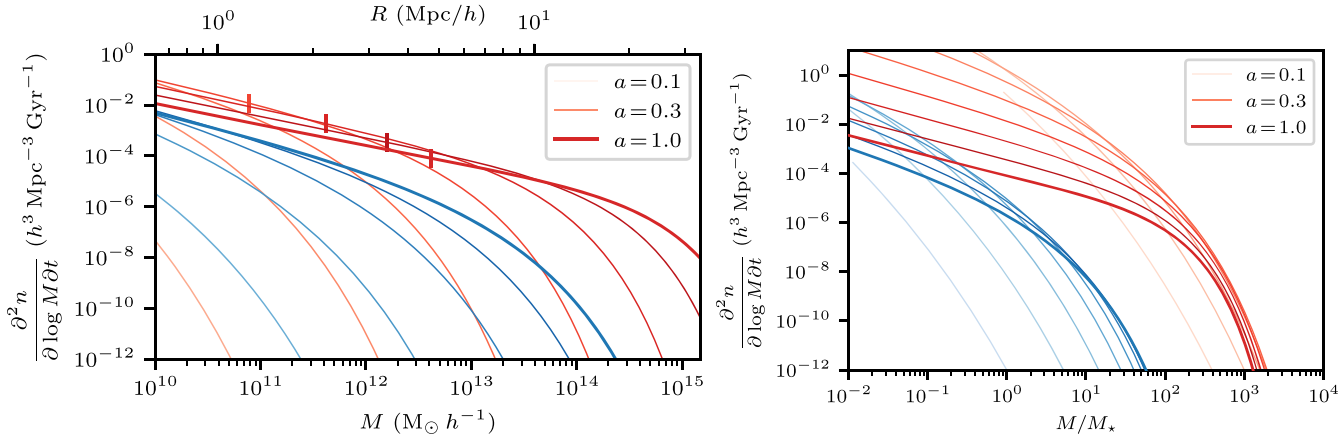

Figure 14. Destruction rates of haloes (red lines) and voids (blue lines) from expansion factor 0.1 (light colour) to 1.0 (dark colour), linearly spaced, in a ΛCDM universe as a function of object mass (left-hand panel) and as a function of mass relative to the non-linear mass (right-hand panel).

haloes, as defined by the number of connected filaments (locally and globally) at a given cosmic time. The upshot of this work is that the packing of peaks (i.e. the 'volume' they occupy, as imposed by their exclusion zone) and saddles implies that three to four filaments typically dominate locally. Interestingly, the rate of filament disappearing must match the peak merger rate, in order to preserve this number. Beyond numerology, this rate is important because filaments feed coherently dark matter haloes, so their lifespan matters to understand the balance between filamentary cold gas inflow (from subsisting filaments) and environmentally driven disruptions (from filament mergers).

Our qualitative understanding of the critical structure of Gaussian random fields remains in close relation to packaging: Each vicinity of a critical point, and with the same argument, of a critical event, must by continuity occupy a certain volume of space, as set by its eigenvalues, which puts constraints on the position of other points in the vicinity. Indeed, critical points are found where the gradient vanishes, with some local curvature, so that the field is quadratic in each eigenvector's direction. As a consequence, the gradient of the field is linear at non-null separation and cannot vanish, so that no other critical point can be found in the direct vicinity of another critical point or event. At large separations, the field decorrelates from its values at the critical point, so that another critical point event becomes likely. In other words, before connecting a given peak to a peak of a different height, the field must first go through a local saddle point along the ridge whose distance is set by the 'width' of that peak.

The same reasoning applies to critical events, except that the field has a specific third-order behaviour along the ridge defined by the eigendirection of the vanishing eigenvalue (it is an inflection point in that direction). For critical events, the process of smoothing the field will impact both the local curvature but also the curvature of all other critical points. Hence, it is expected that smoothing will also disconnect neighbouring peaks as mergers occur: The ridges are smoothed out because technically their saddle points vanish.

We can quantify this process via the two-point function of these events. From the auto- and cross-correlations of the $\mathcal{P}$ and $\mathcal{F}$ events presented in Section 3, we can define the ratio of the separation at the maximum of these two correlations ($s_{ij} = \mathrm{argmax}_s \xi_{ij}(s)$) as a measure of the relative 'proximity' of the two events. Since this ratio $s_{\mathcal{PF}}/s_{\mathcal{PP}} \approx 3/4$ is smaller than 1 (see Fig. 13), it means that filament mergers are more clustered around halo mergers than halo mergers around halo mergers, so that the rate at which filaments disappear matches the merger rate and the typical number of filaments per halo remains constant through cosmic time. As a result of this spatial clustering, the most likely sequence happening is a $\mathcal{PFFP}$ in 2D (one halo merger, followed by two filament mergers, followed by a halo merger), as presented on the cartoon of Fig. 15. This sequence conserves the connectivity of peaks, and is consistent with the relative rates of events. Fig. 15 illustrates an analogous consistent $\mathcal{PF}^4\mathcal{P}$ (one halo merger, followed by four filament mergers, followed by a halo merger) sequence in 3D. Fig. 16 shows how the local connectivity of 3 can also be preserved, as the weaker filaments typically lie off the main plane.

Finally, the clustering of filament disappearance impacts the connectivity of peaks as they merge as discussed in the next section (see Fig. 17, bottom right-hand panel). This is a direct consequence of the clustering of events of the various types.

5.3 Assembly bias in the frame of filaments

Previous works have highlighted the modulation effect induced by the environment on the assembly of dark matter haloes and the galaxies therein, which affect the secondary halo or galaxy properties, an effect often called 'assembly bias'. Let us now make use of the merger statistics to study the impact of the large-scale structures on assembly bias, following Section 3.3. Indeed, it is expected on theoretical ground that, at fixed mass, the typical accretion rate increases when going from the filament centre towards nodes (Musso et al. 2018). Looking at galactic properties instead, Kraljic et al. (2018) showed that the ratio of stellar rotation to dispersion (v/σ) is also modulated as a function of the distance and orientation to the nearest filamentary structure. Kraljic et al. (2020) suggested that galactic properties are linked to the connectivity of the halo, with more connected haloes hosting more quenched and less rotation-supported galaxies.

In this section, we show that in our framework, the connectivity of haloes increases in nodes and decreases in voids, resulting in a differential evolution of haloes, depending on their spatial location in the cosmic web. In order to do this, a suite of Gaussian random fields constrained to the presence of a proto-filament have been generated. The proto-filament is modelled as a filament-type saddle point at the centre of the box, the exact generation procedure being described in Appendix E. It is defined at a scale $R = 5\,\mathrm{Mpc}\,h^{-1}$, is oriented along the z-axis, and lies in a wall in the yz plane. Using the set of constrained GRFs, we compute the excess density of each kind of critical event with respect to the cosmic mean, at fixed smoothing

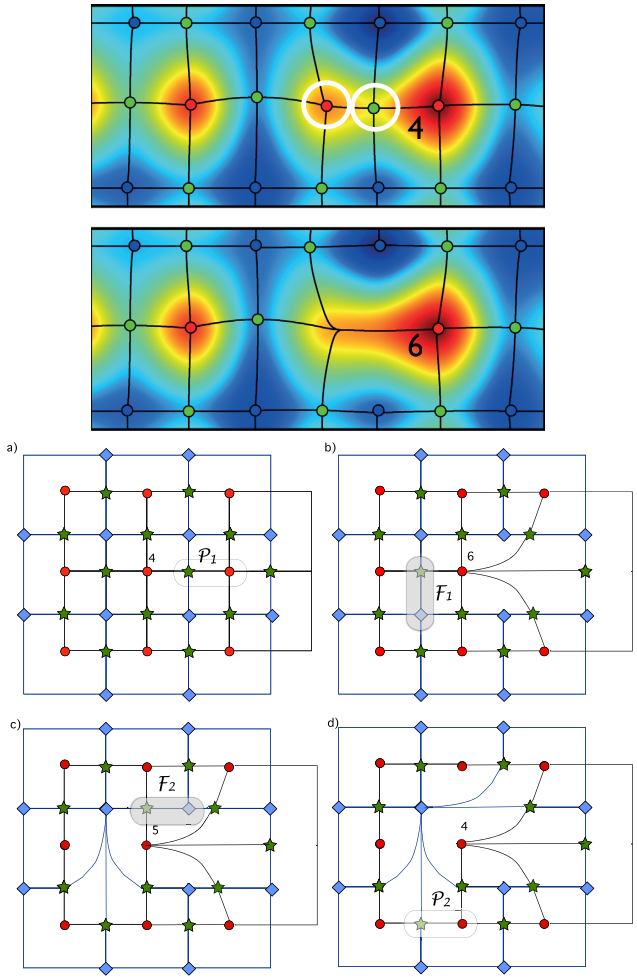

Figure 15. Top panels: snapshots of the density field in 2D at two smoothing scales (colour coded from blue, low density to red, high density). The black lines represent density ridges/troughs connecting the red peaks, and the blue voids via the green saddle points. As the two low persistence pairs of peaks (in white) merge, the connectivity increases from 4 to 6 (as labelled). The fate of this connectivity now depends on the nature and location of the next merger events (inspired from Sousbie 2011). Bottom panels: as labelled from (a) to (d), an abstraction of the merger sequence of a 2D 'cosmic crystal' impacting the connectivity of the central peak. Ridges are shown in black while troughs are shown in dark blue. The red circles represent the peaks, the green stars the saddles, and the blue diamonds the voids. A $\mathcal{P}_1$ merger (highlighted in light grey) raises the mean connectivity of the central peak from 4 to 6, but the next two $\mathcal{F}_{1,2}$ mergers (highlighted in darker grey) lower it back to 4. The next $\mathcal{P}_2$ merger (panel d) will reduce the void's connectivity. A more realistic representation of this process is also visible in Fig. 3.

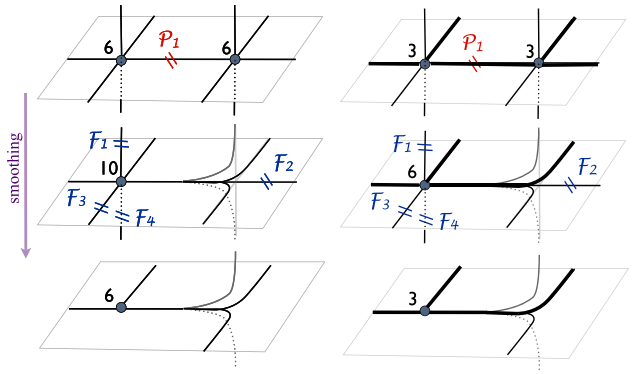

Figure 16. Following the cartoon shown in Fig. 15, the left-hand panel shows a smoothing sequence (from the top to bottom), which would preserve the connectivity of a 3D peak. It requires that each $\mathcal{P}$ merger should be followed by four $\mathcal{F}$ mergers in the vicinity. The right-hand panel highlights how the multiplicity is preserved if one starts with three dominant co-planar filaments.

scale (hence at fixed object mass) $2.5 \leq R \leq 5\,\mathrm{Mpc}\,h^{-1}$. The results are shown in Fig. 17.

Let us first restrict ourselves to the halo merger rate (top left-hand panel of Fig. 17). Going from one void to the wall, from the wall to the filament and from the filament to the nearest node, the halo merger rate increases and the maximum halo merger rate is found near the location where a node is expected ($z \sim \pm 10\,\mathrm{Mpc}\,h^{-1}$). At larger scales, the field becomes unconstrained so that the merger rate falls back to its cosmic mean. We reproduce here from first principles the results of Borzyszkowski et al. (2017), showing that haloes close to the filament centre are stalled compared to those in nodes: They do not undergo many mergers nor do they accrete much as the local tidal fields channels all the matter towards the two surrounding nodes, bypassing the centre of the filament. Quantitatively, haloes forming at the centre of the filament are found to have a halo merger rate close to the cosmic average, while those close to the nodes are expected to have 40 per cent more mergers. Conversely, haloes forming in a void next to a filamentary structure are expected to have a merger rate 20 per cent smaller than the cosmic mean.

Let us now add to the emerging picture the filament coalescence rate. Filament merger rates act locally to decrease the connectivity of haloes, as each merger will disconnect one filament from two haloes. The top right-hand panel of Fig. 17 shows that the merger rate is maximal along the wall and minimal along the filament. Going off the plane of the wall (x-direction), the filament merger rate simply decreases towards the cosmic mean. The filament merger rate is minimal in the nodes (−13 per cent) and maximal in the wall (+10 per cent). As a consequence, haloes forming in a filament and close to a node have a larger halo merger rate but a smaller filament merger rate. This, in turn, will have an impact on the assembly of dark matter haloes and their galaxies. In the wall, where the filament merger rate is the highest, we expect filaments to merge faster than haloes, resulting in haloes with fewer connected filaments. This can be interpreted using the results of Section 2.4. Indeed, in a cosmic wall, the geometry is locally 2D so that the theoretically expected connectivity becomes 4 instead of 6.

The bottom left-hand panel of Fig. 17 shows that the wall merger rate is decreased in walls and even more strongly in filaments compared to the rate found in voids. The minimum wall merger rate is found at the location of the node with a rate −40 per cent smaller than the cosmic mean. Conversely, the wall merger rate is enhanced in the two voids surrounding the wall with a rate 20 per cent above the cosmic mean.

The evolution of the connectivity with cosmic environment is summarized by the bottom right-hand panel of Fig. 17, which shows the ratio of halo mergers ($\mathcal{P}$ critical events) to filament mergers ($\mathcal{F}$ critical events), for which the cosmic mean is 2.055 (see equation 28). Small values of $r_{\mathcal{F}/\mathcal{P}}$ indicate that haloes merge faster than their surrounding filaments, so that the connectivity increases as haloes grow. In contrast, large values of $r_{\mathcal{F}/\mathcal{P}}$ indicate that filaments merge faster than haloes, so that the connectivity decreases as haloes grow. The bottom right-hand panel of Fig. 17 shows that in nodes, the ratio drops to about $r_{\mathcal{F}/\mathcal{P}} \approx 1.1$. In contrast, haloes forming in voids are expected to have a ratio of about 2.4.

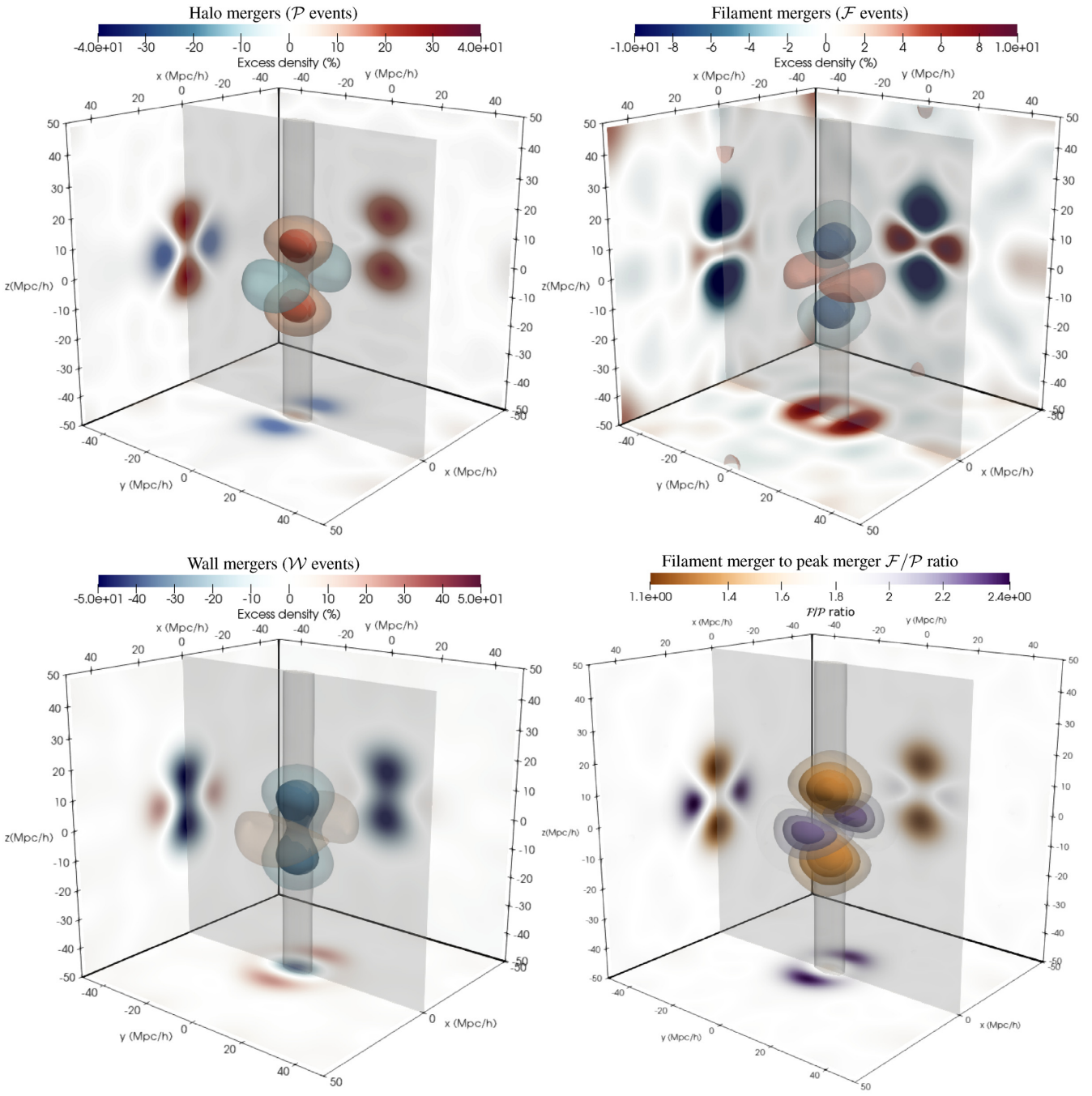

Figure 17. From the left- to right-hand side and top to bottom, peak-merger, filament-merger, and wall-merger excess density around a large-scale proto-filament, illustrated by the vertical cylinder (z-direction) and the wall in which it resides, illustrated by the grey plane (yz plane). The bottom right-hand panel shows the local ratio of filament to peak mergers $r_{\mathcal{F}/\mathcal{P}}$. Each side of the cube shows a slice through the centre, shifted to the side of the plot for visualization purposes. Red regions have an excess of critical events, while blue regions have a deficit of critical events with respect to cosmic average. Interactive versions of these plots can be found online for the halo mergers, filament mergers, wall mergers, and filament-to-peak-merger ratio. Going from voids to wall, from wall to filament, and from filament to the nearest node (along the z-axis), the halo merger rate increases and the filament merger rate decreases. Haloes in the filament are therefore stalled: they merge less than those in the nodes. At the same time, the filament merger rate decreases when going from the filament towards the node so that the mean connectivity, given by the ratio of halo merger to filament merger, is expected to increase.

We therefore expect that, at fixed final mass, haloes forming next to a node will grow an increasing number of connected filaments.[17] The expected physical outcome of this process is that the streams feeding a galaxy growing next to a node will become more and more isotropic with increasing connectivity. Assuming that an isotropic acquisition of matter leads to a smaller amount of angular momentum being transferred down to the disc, we propose that this effect prevents the formation of gaseous discs in the vicinity of nodes. Conversely,

[17] Conversely Codis et al. (2015) found that when averaged over all large-scale structures, connectivity increases with mass.

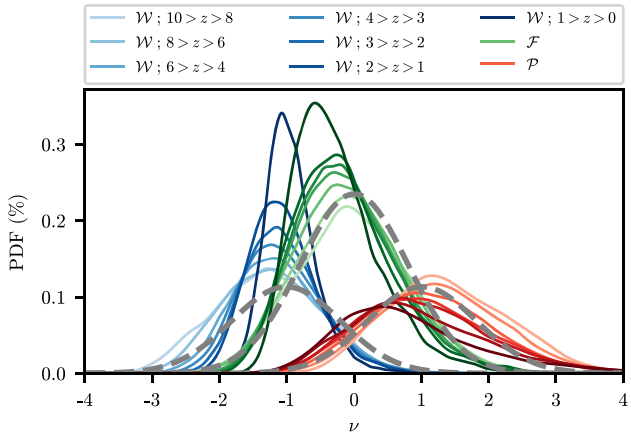

Figure 18. Critical events number counts as a function of the rarity in ΛCDM *N*-body simulations in different redshift bins as mentioned in the legend, with the same colours as Fig. 11. The curves have been normalized so that in each redshift bin, the integral of the three curves ($\mathcal{W}, \mathcal{P}, \mathcal{F}$) equals 1. At high redshift, the merger rates resemble the Gaussian prediction (thick dashed grey lines, with an arbitrary normalization). The skewness of the distributions increases with decreasing redshift as the field departs from Gaussianity, in qualitative agreement with the predictions of Fig. 7.

we expect that haloes growing in the neighbouring voids see their filaments destroyed faster than they merge, so that the halo is likely to grow with steadier flows coming from a few filaments (only the dominant ones survive) (see also Codis et al. 2015; Laigle et al. 2015, sections 6.2.1 and 5, respectively, for similar conclusions reached via the kinematic structure of large-scale flows in filaments).

5.4 Departure from Gaussianity at high z

Using the results of Section 2.5, we detail in this section the evolution of the critical event number counts in the mildly non-linear regime, at high z. Let us briefly quantify the effect first on simulations, and then compare to the proxy of Section 2.5 relying on known perturbative results. Fig. 18 presents the redshift evolution of critical event counts measured in 45 realizations of ΛCDM simulations in boxes of 500 Mpc h^{-1} involving 256^3 particles evolved using GADGET (Springel, Yoshida & White 2001). At each snapshot, the density field is sampled on a 256^3 grid smoothed with a Gaussian filter over 6 Mpc h^{-1}. The algorithm described in Appendix H is used to identify and match the critical points and critical events.

At high redshift ($z \gtrapprox 10$), the measured number counts of critical events is close to the Gaussian prediction. While we cannot make definite statements given the level of shot noise in the measurements and existing transients at high redshifts, clear trends are seen in the counts. In particular, at lower redshift, the $\mathcal{P}$ and $\mathcal{F}$ counts shift towards lower contrast, but, respectively, decrease and increase in amplitude, while the $\mathcal{W}$ counts increase in amplitude. Since haloes in low-density environments form later, it is expected that the low-z counts are biased towards low densities. Similarly, the mean density of a filamentary structure decreases with increasing time, as the less dense filaments take more time to gravitationally form, so that the PDFs of the filament mergers shifts to smaller densities at low z. The evolution of void structures with cosmological time mirrors that of peaks: early forming voids are the most underdense while late-time voids form out of less underdense regions. At fixed resolution, this results in a shift of the typical density of voids towards higher densities which in turn shifts the $n_{\rm me}^{\mathcal{W}}$ towards higher densities.

Overall, the cosmic evolution of the measured event counts seems to be in fairly good agreement with the model presented in Fig. 7, suggesting that, indeed, the set of critical events in the initial density field do capture the upcoming cosmic evolution of the cosmic web. Further works beyond the scope of this paper will be necessary to better match the weakly non-Gaussian regime in more details.

5.5 Discussion

There is a long tradition of relying on merger trees of dark matter haloes extracted from simulations as a means to tag the haloes with physical properties (see, e.g. Lacey & Silk 1991; White & Frenk 1991; Benson & Bower 2010, and references therein). It has been suggested that galactic properties, such as spin, do not seem to be entirely encoded in the (halo) merger tree (Vitvitska et al. 2002; Benson, Behrens & Lu 2020), a conclusion that could indicate that the anisotropy of the environment contributes to the spin of galaxies (Codis et al. 2015). One of the long-term main motivations for the present work was to provide us with a theoretically motivated extension to halo merger trees by adding the other two merger trees (filaments and walls). Using the theory and the tools developed in this paper, the set of critical events that define these merger trees could be fed into semi-analytical modelling. This would complement existing approaches by providing not only the past history of the DM halo (*via* its merger tree), but also of the other substructures in the Lagrangian patch (*via* the filament and wall merger trees). To that end, the critical event theory provides an unambiguous and theoretically motivated framework to describe and detect such events, either in the initial conditions (as a means to make predictions) or in numerical simulations (as a means to quantify the evolution).

Another possible approach would be to rely on modern machine learning techniques to identify which combination(s) of critical events are most likely to lead to galaxies of a certain type to be produced in cosmological simulations. This strategy is likely to be efficient and rewarding, as the set of critical events is a very strong compression of the set of initial conditions, and because once the segmentation has been done, the subset of events which are in the past history of a galaxy with a given tag have physical meaning. For instance, recent disconnect of filaments are likely to impact gas infall hence star formation and disc reformation (Pichon et al. 2011; Danovich et al. 2012; Aragon Calvo, Neyrinck & Silk 2019). The set of critical events represents a useful effective topological compression of the initial conditions which will impact the upcoming 'dressed' merger tree (i.e. the cosmic evolution of peaks *and* their filaments and walls). Note that the exact relative configuration of critical events in the position–smoothing space may be of relevance, and is not fully captured by the sole knowledge of the one- and two-point statistics.

As an illustrative proof of concept, we have detected the critical events in the initial conditions of two 256^3 *N*-body simulations. Fig. 19 shows two pairs of consecutive snapshots zoomed around an $\mathcal{F}$ and a $\mathcal{W}$ critical event (in simulations of sizes 100 and 500 Mpc h^{-1}, respectively). In order to take into account the Zel'dovich flow, we have displaced the critical events from their initial Lagrangian position by the mean displacement of the neighbouring DM particles. As expected, the $\mathcal{F}$ critical event can be related to the disappearance of a filament between two walls, while the $\mathcal{W}$ critical event encodes the disappearance of a wall between two voids. This figure illustrates that there exists at least a subset of critical events that can indeed be mapped to actual mergers in the evolved Universe, but note that the mapping between the critical events and the time of the merger in the simulation was done here

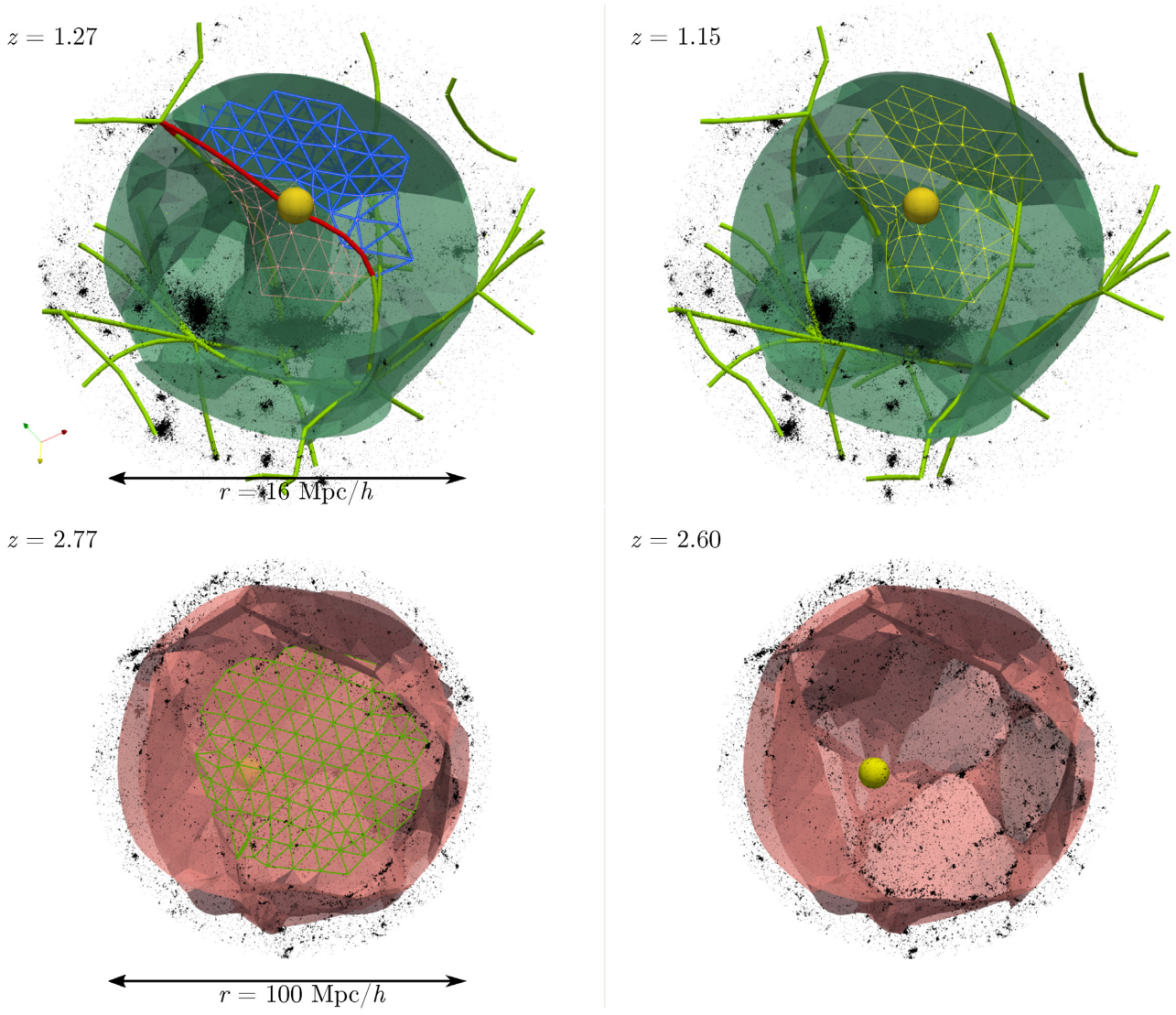

Figure 19. Top panels: two consecutive snapshots in a $100\,\mathrm{Mpc}\,h^{-1}$ simulation showing an $\mathcal{F}$ critical event (yellow ball) that encodes the disappearance of a filament (highlighted in red) separating two walls (red and blue wireframes). After the event, only one wall has survived (yellow wireframe). Bottom panels: two consecutive shapshots in a $500\,\mathrm{Mpc}\,h^{-1}$ simulation showing a $\mathcal{W}$ critical event (yellow ball) that encodes the merger of two voids separated by a wall (green wireframe). After the event, only one void subsists and the wall has disappeared. Individual DM particles are shown as black dots. The skeleton (green lines) and the walls (green and red surfaces) have been extracted using DISPERSE. Both critical events can be related to merger event in the evolved Universe.

by visual inspection. The quantitative study of the accuracy of the mapping between critical events in the initial conditions and in the corresponding dynamically evolved simulation will be the subject of future work.

One should note that, even if the mapping between critical events in the initial conditions and critical events in the density field evolved by the simulation could not be established uniquely, the applications highlighted above would be left unchanged as they only rely upon the detection of critical events in the *evolved field*, but it would however limit the scope of theoretical predictions.

Mapping of intensity of spectral lines, for instance, the H I 21-cm line (Madau, Meiksin & Rees 1997) across the sky, could also benefit from applying the present formalism to sequences of 2D maps as a function of redshift. Existing (e.g. Chime, Shaw et al. 2014) or upcoming surveys (e.g. SKA; Camera, Santos & Maartens 2015) will indeed provide both extrema and merger counts extracted from sets of maps at various redshifts. The cosmology dependence of extrema counts is through (R_*, γ) and the relevant cumulants, whereas the cosmology dependence of critical event counts also involve $(\tilde{R}, \tilde{\gamma})$ and higher order cumulants at fixed level of non-Gaussianity (e.g. involving third-order derivative of the field to first order as discussed in Section 2.5). Hence, studying both counts as a function of redshift will prove complementary.

These possible applications highlight the versatility of critical events: They yield diagnostics in the initial conditions, together with a theoretically motivated description of processes driving the evolution of the cosmic web in the evolved Universe. The theory presented in this paper provides a description of the evolution of mass infall that may play an important role in galaxy formation. Further efforts should be made to relate infall to the internal effects driving the formation of galaxies (star formation, feedback, turbulence, etc.).

5.5.1 Applications beyond cosmology

The present analysis was mostly restricted to (quasi-)Gaussian random fields because of their relevance in cosmology and also because in this context the theory can be developed in some details (as a Gaussian process defines a Morse function on a scale-by-scale basis). But the concept of bifurcation of critical points in a one parameter set of random fields extends beyond Gaussianity. Any system involving random field controlled by one parameter could, in principle, be investigated with this framework in order to identify bifurcation/mergers of ridges (though the specific role played by Gaussian smoothing would clearly generally not hold). For instance, critical events in dust maps (such as Meisner & Finkbeiner 2013; Planck Collaboration XI 2018b) could be used as an alternative statistics to quantify the properties of the underlying turbulence.

The theory of critical events could also find applications in fields where data are well described by their geometry, as critical events describe how this geometry changes with scale. For example, in the context of streaming of images, the set of critical events within a 2D image characterizes its multiscale topology. It would therefore be of interest to send the set of critical events, starting from the ones at the largest smoothing scales, as a means of prioritizing which subregion of the image needs to be streamed first because the topology of its excursion (i.e. the local parsimonious representation of the image as iso-contours) has changed. This would allow the received image to acquire its most important topological features first.

Following the results of Appendix A, our formalism could be extended to situations where the field whose evolution is investigated corresponds to realizations of probability distributions living in higher dimensions (or on more complex manifolds). In a more abstract setting corresponding to a landscape drawn from a given probability function, a wide range of important physical processes occur when rare events collide, boosting detection probabilities and passing a given threshold. For instance, dark matter annihilation rates (which scale like the density squared) are boosted when two substructures merges (Clark et al. 2018). In the context of this work, this corresponds to nucleation, or the appearance of pairs of critical points as one 'unsmoothes' (or more generally evolves) the field.

6 CONCLUSION

As a proxy for cosmic evolution, we computed the merger rate of critical points (peaks, saddle points, and minima) as a function of smoothing scale from the primordial density field to forecast critical events (halo, filament, and wall mergers) that drive the assembly of dark matter haloes and possibly galaxies. We recovered the non-linear prediction for the net density of peak merger found by Hanami (2001) and further considered all sets of critical points coalescence, including wall saddle to filament saddle (filament mergers) and wall saddle to minima (wall or void mergers), as they modify the geometry of galactic infall, such as filament disconnection or void disappearance, thus generalizing previous results that focused only on peaks. This 'critical event theory' is central to our understanding of the effect of the cosmic web on the formation of galaxies, since their evolution is the result of their past history, which is encoded in their extended merger tree and the properties of their host halo.

The key results of this paper are the following:

(i) We studied critical events of all types and presented analytical formulas for the one-point statistics of these events in fields of dimensions up to 6 (Section 2), and also their clustering properties *via* their two-point statistics (Section 3).

(ii) We have developed an algorithm to find critical events in numerical data sets that we used as a confirmation of the theory (Section 4). Such algorithm could be used, for example, to pre-compress streaming of images, or as input to machine learning as a means to learn galactic morphology from the initial conditions. We also developed an algorithm to generate Gaussian random fields subject to a given critical event.

(iii) We provided a covariant formulation of the critical event theory, which allowed us to also compute the two-point statistics for critical events. The two-point statistics show that halo mergers are typically followed by filament mergers, so that the connectivity is preserved.

(iv) We have shown that the critical event theory can be further extended to take into account the early stages of non-linear gravitational evolution. This has then been compared qualitatively to numerical simulations at high redshift. This extension also probes the non-Gaussianities that arise from primordial non-Gaussianities and can be used as a cosmological measurement.

We also presented some practical applications of the theory to astrophysical problems in Section 5. We computed the destruction rate of haloes and voids as a function of mass and redshift in a ΛCDM cosmology using a simple model to assign a mass and time to critical events (Section 5.1). This can be used as a test for the critical event theory, as well as an alternative cosmological measurement. We have established the link between critical events and connectivity. This allowed us to compute the connectivity of peaks and other critical events in arbitrary dimensions.[18] Physically, a duality between the evolution of the cosmic web (critical events) and its topological features (connectivity) was highlighted (Section 5.2) In addition, we showed that haloes forming near cosmic nodes do so by increasing their connectivity, with possible implication for the formation of their host galaxy (Section 5.3). Finally, using *N*-body simulations, we have shown that the critical event theory statistically recovers the evolution of the merger rates of the different structures (haloes, filaments, walls) in the mildly non-linear regime at high redshift (Section 5.4).

We have only touched on practical applications for the forecasting of special events in a multiscale landscape. It may prove to be a fruitful field of upcoming research in astronomy and beyond.

ACKNOWLEDGEMENTS

This work was partially supported by the Spin(e) grant ANR-13-BS05-0005 (cosmicorigin.org) of the French Agence Nationale de la Recherche and the Segal grant ANR-19-CE31-0017 (www.secular-evolution.org) of the French Agence Nationale de la Recherche. This project has received funding from the European Union Horizon 2020 research and innovation program under grant agreement No. 818085 GMGalaxies and by the National Science Foundation under Grants No. PHY11-25915 and PHY-1748958. SC's research is partially supported by Foundation MERAC. CC thanks the Institut Lagrange de Paris for partial funding. SC and CC thank the Korea Institute for Advanced Study for hospitality and financial support during the course of this project. MM thanks the Max-Planck Institute for Astrophysics for hospitality. CP thanks S. Colombi for pointing to Hanami's paper and acknowledges early and late discussions with Thierry Sousbie and Pooran Memari, respectively. We thank the referee, J. Primack, for a constructive report. We also thank

[18] It yields an analytical prediction of connectivity of peak in four dimensions: $\kappa_4 = 200\pi/(75\pi - 114 - 100\cot^{-1}(2)) \approx 8.35$.

A. Dekel, N. Cornuault, J. Devriendt, C. Park, and E. Pichon for fruitful discussions and useful comments, and CC thanks S. White for constructive criticisms. This work has made use of the Horizon Cluster hosted by Institut d'Astrophysique de Paris. We thank Stephane Rouberol for running smoothly this cluster for us and Thierry Sousbie for DISPERSE.

DATA AVAILABILITY

The data underlying this paper will be shared on reasonable request to the corresponding author.

REFERENCES

Agertz O., Teyssier R., Moore B., 2009, MNRAS, 397, 64
Aragon Calvo M. A., Neyrinck M. C., Silk J., 2019, Open J. Astrophys., 2, 7
Aubert D., Pichon C., 2007, MNRAS, 374, 877
Bardeen J. M., Bond J. R., Kaiser N., Szalay A. S., 1986, ApJ, 304, 15
Benson A. J., Bower R., 2010, MNRAS, 405, 1573
Benson A., Behrens C., Lu Y., 2020, MNRAS, 496, 3371
Bernardeau F., Colombi S., Gaztañaga E., Scoccimarro R., 2002, Phys. Rep., 367, 1
Blumenthal G. R., Faber S. M., Primack J. R., Rees M. J., 1984, Nature, 311, 517
Bond J. R., Myers S. T., 1996, ApJS, 103, 1
Bond J. R., Cole S., Efstathiou G., Kaiser N., 1991, ApJ, 379, 440
Bond J. R., Kofman L., Pogosyan D., 1996, Nature, 380, 603
Borzyszkowski M., Porciani C., Romano-Díaz E., Garaldi E., 2017, MNRAS, 469, 594
Bournaud F., Jog C. J., Combes F., 2007, A&A, 476, 1179
Camera S., Santos M. G., Maartens R., 2015, MNRAS, 448, 1035
Castorina E., Paranjape A., Hahn O., Sheth R. K., 2016, preprint (arXiv:1611.03619)
Clark H. A., Scott P., Trotta R., Lewis G. F., 2018, J. Cosmol. Astropart. Phys., 2018, 060
Codis S., Pichon C., Pogosyan D., Bernardeau F., Matsubara T., 2013, MNRAS, 435, 531
Codis S., Pichon C., Pogosyan D., 2015, MNRAS, 452, 3369
Codis S., Pogosyan D., Pichon C., 2018, MNRAS, 479, 973
Crittenden R. G., Natarajan P., Pen U.-L., Theuns T., 2001, ApJ, 559, 552
Danovich M., Dekel A., Hahn O., Teyssier R., 2012, MNRAS, 422, 1732
Dekel A., Birnboim Y., 2006, MNRAS, 368, 2
Diemer B., 2018, ApJS, 239, 35
Doroshkevich A. G., 1970, Astrophysics, 6, 320
Dubinski J., da Costa L. N., Goldwirth D. S., Lecar M., Piran T., 1993, ApJ, 410, 458
Dubois Y., Pichon C., Haehnelt M., Kimm T., Slyz A., Devriendt J., Pogosyan D., 2012, MNRAS, 423, 3616
Dubois Y., Peirani S., Pichon C., Devriendt J., Gavazzi R., Welker C., Volonteri M., 2016, MNRAS, 463, 3948
Edelsbrunner H., Letscher D., Zomorodian A., 2002, Discrete Comput. Geom., 28, 511
Eisenstein D. J., Hu W., 1998, ApJ, 496, 605
Eisenstein D. J., Hu W., 1999, ApJ, 511, 5
Fakhouri O., Ma C.-P., Boylan-Kolchin M., 2010, MNRAS, 406, 2267
Gay C., 2011, PhD thesis, Université Pierre et Marie Curie
Gay C., Pichon C., Pogosyan D., 2012, Phys. Rev. D, 85, 023011
Genel S., Genzel R., Bouché N., Naab T., Sternberg A., 2009, ApJ, 701, 2002
Hahn O., Porciani C., Dekel A., Carollo C. M., 2009, MNRAS, 398, 1742
Hanami H., 2001, MNRAS, 327, 721
Jedamzik K., 1995, ApJ, 448, 1
Jennings E., Li Y., Hu W., 2013, MNRAS, 434, 2167
Virtanen P. et al., 2020, Nat. Methods, 17, 261
Kaiser N., 1984, ApJ, 284, L9
Kraljic K. et al., 2018, MNRAS, 474, 547
Kraljic K. et al., 2020, MNRAS, 491, 4294
Lacey C., Cole S., 1993, MNRAS, 262, 627
Lacey C., Silk J., 1991, ApJ, 381, 14
Laigle C. et al., 2015, MNRAS, 446, 2744
Ludlow A. D., Porciani C., Borzyszkowski M., 2014, MNRAS, 445, 4110
Madau P., Meiksin A., Rees M. J., 1997, ApJ, 475, 429
Maggiore M., Riotto A., 2010, ApJ, 711, 907
Manrique A., Salvador-Sole E., 1995, ApJ, 453, 6
Manrique A., Salvador-Sole E., 1996, ApJ, 467, 504
Meisner A. M., Finkbeiner D. P., 2013, ApJ, 781, 5
Moore A. W. et al., 2001, Fast Algorithms and Efficient Statistics: N-Point Correlation Functions, Springer, Berlin, Heidelberg, p. 71
More S., Diemer B., Kravtsov A. V., 2015, ApJ, 810, 36
Musso M., Sheth R. K., 2012, MNRAS, 423, L102
Musso M., Sheth R. K., 2019, preprint (arXiv:1907.09147)
Musso M., Cadiou C., Pichon C., Codis S., Kraljic K., Dubois Y., 2018, MNRAS, 476, 4877
Naab T., Burkert A., 2003, ApJ, 597, 893
Paranjape A., Sheth R. K., 2012, MNRAS, 426, 2789
Paranjape A., Sheth R. K., Desjacques V., 2013, MNRAS, 431, 1503
Peacock J. A., Heavens A. F., 1990, MNRAS, 243, 133
Pichon C., Pogosyan D., Kimm T., Slyz A., Devriendt J., Dubois Y., 2011, MNRAS, 2493
Planck Collaboration VI, 2018a, preprint (arXiv:1807.06209)
Planck Collaboration XI, 2018b, preprint (arXiv:1801.04945)
Pogosyan D., Bond J. R., Kofman L., Wadsley J., 1998, Wide Field Surveys in Cosmology. Editions Frontieres, London
Pogosyan D., Gay C., Pichon C., 2009a, Phys. Rev. D, 80, 081301
Pogosyan D., Pichon C., Gay C., Prunet S., Cardoso J. F., Sousbie T., Colombi S., 2009b, MNRAS, 396, 635
Pranav P., Edelsbrunner H., van de Weygaert R., Vegter G., Kerber M., Jones B. J. T., Wintraecken M., 2017, MNRAS, 465, 4281
Press W. H., Schechter P., 1974, ApJ, 187, 425
Prunet S., Pichon C., Aubert D., Pogosyan D., Teyssier R., Gottloeber S., 2008, ApJS, 178, 179
Ramakrishnan S., Paranjape A., Hahn O., Sheth R. K., 2019, MNRAS, 489, 2977
Robertson B. E., Kravtsov A. V., Tinker J., Zentner A. R., 2009, ApJ, 696, 636
Rodriguez-Gomez V. et al., 2015, MNRAS, 449, 49
Rossi G., 2013, MNRAS, 430, 1486
Shaw J. R., Sigurdson K., Pen U.-L., Stebbins A., Sitwell M., 2014, ApJ, 781, 57
Shen J., Abel T., Mo H., Sheth R. K., 2006, ApJ, 645, 783
Sheth R. K., Mo H. J., Tormen G., 2001, MNRAS, 323, 1
Sheth R. K., van de Weygaert R., 2004, MNRAS, 350, 517
Sousbie T., 2011, MNRAS, 414, 350
Sousbie T., Pichon C., Kawahara H., 2011, MNRAS, 414, 384
Springel V., Yoshida N., White S. D. M., 2001, New Astron., 6, 79
Toomre A., Toomre J., 1972, ApJ, 178, 623
van de Weygaert R. et al., 2011, Trans. Comput. Sci., 14, 60
Vitvitska M., Klypin A. A., Kravtsov A. V., Wechsler R. H., Primack J. R., Bullock J. S., 2002, ApJ, 581, 799
White S. D. M., Frenk C. S., 1991, ApJ, 379, 52
Zhang L., 2015, preprint (arXiv:1509.00537)

SUPPORTING INFORMATION

Supplementary data are available at *MNRAS* online.

Figure 1. 2 + 1D landscape of a 2D field smoothed at a scale R.
Figure 2. 2 + 1D landscape of a 2D field smoothed at a scale R.
Figure 5. 2D slice, in the (x, R) plane, of the conditional mean density in the 3 + 1D position–smoothing space, under the constraint of a destruction critical event (red sphere, top panel) and a nucleation critical event (red box, bottom panel) at $R = 1$, $x = 0$.

Please note: Oxford University Press is not responsible for the content or functionality of any supporting materials supplied by the authors. Any queries (other than missing material) should be directed to the corresponding author for the article.

APPENDIX A: CRITICAL EVENTS IN ND

For the sake of completeness and possible interest in other fields of research, let us present the one-point statistics of critical events in arbitrary dimensions. We first generalize the spectral parameters relevant to the critical event theory in d dimensions in Appendix A1. We then proceed to derive the joint PDFs of the field and its second derivatives in Appendix A2, and its first and third derivatives in Appendix A3. These results are then used in Appendix A4 to derive the critical event number counts in higher dimensions. From this, we then proceed to provide asymptotic formulas in the high-density limit (Appendix A5), compute the ratios of critical events (Appendix A6), and establish the connection between critical points counts and critical events in any dimension (Appendix A7). In Appendix A8, we finally provide a confirmation of the net merger density derived using the number counts of critical points in 3D.

A1 Spectral parameters

In this section, we provide definitions for the spectral parameters of a d-dimensional Gaussian random field. Let us first define the variance of the ith derivative of the field:

$$\sigma_i^2(R) = \frac{d}{(4\pi)^{d/2}\Gamma\left(1+\frac{d}{2}\right)} \int_0^\infty \mathrm{d}k k^{d-1} P_k(k) k^{2i} W^2(kR), \tag{A1}$$

where $P_k(k)$ is the ND power spectrum and $W(kR) = \exp(-(kR)^2/2)$. The characteristic scales R_0, R_*, and $\tilde{R}$ are defined by equation (4), and the spectral parameters γ and $\tilde{\gamma}$ are defined by equation (5). In d dimensions for a power-law power spectrum with index n, we have

$$\frac{R_0^2}{R^2} = \frac{2}{n+d}, \quad \frac{R_*^2}{R^2} = \frac{2}{n+d+2}, \quad \frac{\tilde{R}^2}{R^2} = \frac{2}{n+d+4},$$
$$\gamma^2 = \frac{n+d}{n+d+2}, \quad \tilde{\gamma}^2 = \frac{n+d+2}{n+d+4}. \tag{A2}$$

A2 Joint PDF of the field and its second derivatives

From Pogosyan et al. (2009b), the joint distribution function of the set of d eigenvalues of the d-dimensional Hessian $\sigma_2\boldsymbol{\lambda}$ and density ν is

$$P(\nu, \boldsymbol{\lambda}) = \frac{1}{\mathcal{N}} \Delta(\boldsymbol{\lambda}) \exp\left(-\frac{1}{2} Q_\gamma(\nu, \boldsymbol{\lambda})\right), \tag{A3}$$

where $\boldsymbol{\lambda} = \{\lambda_i\}_{i=1\ldots d}$, $\Delta(\boldsymbol{\lambda}) = \prod_{i<j}(\lambda_j - \lambda_i)$ is the Vandermonde determinant, and Q_γ is a quadratic form in λ_i and ν given by

$$Q_\gamma(\nu, \boldsymbol{\lambda}) = \nu^2 + \frac{\left(\sum_i \lambda_i + \gamma\nu\right)^2}{(1-\gamma^2)} + \mathcal{Q}_d(\boldsymbol{\lambda}), \tag{A4}$$

with

$$\mathcal{Q}_d(\boldsymbol{\lambda}) = \frac{d(d+2)}{2}\left[\sum_i \lambda_i^2 - \frac{1}{d}\left(\sum_i \lambda_i\right)^2\right]$$
$$= (d+2)\left[\frac{1}{2}(d-1)\sum_i \lambda_i^2 - \sum_{i<j}\lambda_i\lambda_j\right] \tag{A5}$$

proportional to the Euclidean norm of the detraced Hessian matrix. Note that the expression in equation (A3) assumes that the eigenvalues are sorted; otherwise, the Vandermonde determinant would come with an absolute value. Finally $\mathcal{N}$ is a normalization quantified below.

A2.1 Determining the PDF normalization

Directly integrating equation (A3) is not easy due to the presence of couplings between the different variables in Q_γ. However, this integral is actually related to the integral over the joint PDF of the field and its second derivatives in an arbitrary frame. Indeed, the expression of the PDF in equations (A3)–(A5) was obtained after a change of variables from an arbitrary frame to the Hessian eigenframe, and the presence of the Vandermonde determinant is related to the orthogonality constraint of the matrix of eigenvectors (Doroshkevich 1970; Bardeen et al. 1986; Pogosyan et al. 2009b). More precisely, taking into account the volume of integration over all possible eigenvectors that keep the diagonalization of the Hessian unique, we have (Zhang 2015)

$$\mathcal{I} = \int \mathrm{d}\boldsymbol{y} \exp\left(-\frac{1}{2}\boldsymbol{y}^\mathrm{T}\cdot\boldsymbol{\Sigma}^{-1}\cdot\boldsymbol{y}\right),$$
$$= \frac{\mathrm{Vol}(O(d))}{2^d}\int \mathrm{d}\nu \prod_{i=1}^d \mathrm{d}\lambda_i \Delta(\boldsymbol{\lambda}) \exp\left(-\frac{Q_\gamma(\boldsymbol{\lambda})}{2}\right), \tag{A6}$$

where $\boldsymbol{y} = \{\nu, x_{ij}, 1 \le i \le j \le d\}$, and the volume of the orthogonal group in dimension d, $O(d)$, is given by

$$\mathrm{Vol}(O(d)) = \frac{2^d \pi^{d(d+1)/4}}{\prod_{k=1}^d \Gamma(k/2)}. \tag{A7}$$

Note that in equation (A6), the integral is made over the *sorted* eigenvalues $\lambda_1 < \lambda_2 <, \ldots, < \lambda_d$. The factor 2^d in the denominator comes from the fact that the diagonalization mapping is unique if we sort the eigenvalues *and* we choose the sign of each eigenvector. Finally, the matrix $\boldsymbol{\Sigma}$ above is the covariance matrix of the $\boldsymbol{y}$ vector.

We note that the first line of equation (A6) is nothing else than a multivariate Gaussian integral over $d(d+1)/2+1$ variables, so that its value is

$$\mathcal{I} = (2\pi)^{(d(d+1)+2)/4} |\boldsymbol{\Sigma}|^{1/2}. \tag{A8}$$

Comparing equations (A6) and (A3), the normalization factor $\mathcal{N}$ can then be written as a function of the determinant of $\boldsymbol{\Sigma}$:

$$\mathcal{N} = \frac{2^d}{\mathrm{Vol}(O(d))}(2\pi)^{\frac{d(d+1)+2}{4}} |\boldsymbol{\Sigma}|^{1/2}. \tag{A9}$$

A2.2 Determinant of $\boldsymbol{\Sigma}$

To evaluate $|\boldsymbol{\Sigma}|$, we recall that simple computations in Fourier space show that (Bardeen et al. 1986; Pogosyan et al. 2009b)

$$\langle x_{ij} x_{kl}\rangle = \frac{1}{d(d+2)}\left(\delta_{ij}\delta_{kl} + \delta_{ik}\delta_{jl} + \delta_{il}\delta_{jk}\right), \tag{A10}$$

while $\langle x^2\rangle = 1$ and $\langle x x_{ii}\rangle = -\gamma/d$. Therefore, the matrix $\boldsymbol{\Sigma}$ is block diagonal, with a dense subblock $\boldsymbol{\Sigma}_{\mathrm{diag}}$ corresponding to the field x itself and the diagonal elements of the Hessian x_{ii}, and a diagonal subblock $\boldsymbol{\Sigma}_{\mathrm{offdiag}}$ corresponding to the $d(d-1)/2$ independent off-diagonal elements $x_{i<j}$ of the Hessian, each having equal variance $(d(d+2))^{-1}$. The determinant of $\boldsymbol{\Sigma}$ thus factorizes into $|\boldsymbol{\Sigma}_{\mathrm{diag}}| \times |\boldsymbol{\Sigma}_{\mathrm{offdiag}}|$, where the determinant of the off-diagonal Hessian elements is simply given by

$$|\boldsymbol{\Sigma}_{\mathrm{offdiag}}| = (d(d+2))^{-d(d-1))/2}. \tag{A11}$$

Let us now compute the contribution of the dense covariance matrix $\boldsymbol{\Sigma}_{\mathrm{diag}}$ of the field and the diagonal elements x_{ii} of the Hessian. To compute its determinant, we will diagonalize the matrix using two successive steps. Let us first change to set of variables $\{\nu, I_1,$

$x_{11} - I_1/d, \ldots, x_{(d-1)(d-1)} - I_1/d\}$. The matrix $\mathbf{M}$ of the variable change reads

$$\mathbf{M} = \begin{pmatrix} 1 & 0 & \dots & \dots & \dots & 0 \\ 0 & 1 & \dots & \dots & \dots & 1 \\ \vdots & \frac{d-1}{d} & -\frac{1}{d} & \dots & \dots & -\frac{1}{d} \\ \vdots & -\frac{1}{d} & \frac{d-1}{d} & -\frac{1}{d} & \dots & \vdots \\ \vdots & \vdots & \ddots & \ddots & \ddots & \vdots \\ 0 & -\frac{1}{d} & \dots & -\frac{1}{d} & \frac{d-1}{d} & -\frac{1}{d} \end{pmatrix}. \tag{A12}$$

It is straightforward to show that the Jacobian determinant $|\mathbf{M}| = 1$, e.g. by first casting the trace I_1 as the last variable, and by using the Schur complement to the diagonal element corresponding to the trace. In this new set of variables, the covariance matrix reads

$$\mathbf{M}\boldsymbol{\Sigma}\mathbf{M}^{\mathrm{T}} = \begin{pmatrix} \begin{pmatrix} 1 & -\gamma \\ -\gamma & 1 \end{pmatrix} & \mathbf{0} \\ \mathbf{0} & \boldsymbol{\Xi} \end{pmatrix}, \tag{A13}$$

where

$$\boldsymbol{\Xi} = \frac{2}{d(d+2)}\mathbf{I}_{d-1} - \frac{2}{d^2(d+2)}\boldsymbol{u}\boldsymbol{u}^{\mathrm{T}}, \tag{A14}$$

and $\boldsymbol{u}$ is a $d-1$ column vector with all elements equal to 1.

At the second step, we diagonalize the matrix $\boldsymbol{\Xi}$, which is easily accomplished by collecting orthogonal bases of Span($\boldsymbol{u}$) and Span($\boldsymbol{u}$)$^{\perp}$, respectively. The last $d-2$ eigenvalues are equal to $2/d(d+2)$, while the first eigenvalue is equal to $2/d(d+2) - 2(d-1)/d^2(d+2) = 2/d^2(d+2)$. The determinant of $\boldsymbol{\Sigma}_{\mathrm{diag}}$ is therefore

$$|\boldsymbol{\Sigma}_{\mathrm{diag}}| = (1-\gamma^2)\left[\frac{d(d+2)}{2}\right]^{-(d-1)} d^{-1}. \tag{A15}$$

Putting everything together, we get the final expression of the PDF normalization $\mathcal{N}$ entering equation (A3):

$$\mathcal{N} = 2^{(d(d+3))/4}(d(d+2))^{-(d(d+1)-2)/4}\sqrt{\frac{\pi}{d}}\sqrt{1-\gamma^2}\prod_{k=1}^{d}\Gamma(k/2). \tag{A16}$$

A3 Joint statistics of the first and third derivatives

A3.1 Expression for the joint PDF

Here, we will look into the pdf of the first and third derivatives in d dimensions in order to compute the odd derivative term C_{odd} that enters critical event number counts in d dimensions. Let us first describe the joint distribution globally. The structure of this distribution is quite similar to that of the field and its second derivatives that were presented in Appendix A2. We have

$$P(z) = \frac{1}{\sqrt{(2\pi)^n\,|\widetilde{\boldsymbol{\Sigma}}|}}\exp\left(-\frac{1}{2}z^{\mathrm{T}}\widetilde{\boldsymbol{\Sigma}}^{-1}z\right), \tag{A17}$$

where $z = \{x_i, x_{ijk}, 1 \le i \le j \le k \le d\}$ is the set of the first and third derivative tensors, $\widetilde{\boldsymbol{\Sigma}}$ is the covariance matrix of z, and $n = d(d+1)(d+2)/6 + 1$ is the number of non-redundant terms in z. As before, the first derivatives get coupled to the third derivatives only via traces of the latter. Indeed, it can be shown that the quadratic form of the Gaussian PDF reads (Pogosyan et al. 2009b)

$$z^{\mathrm{T}}\widetilde{\boldsymbol{\Sigma}}^{-1}z = d\,\mathrm{Tr}\left\{\begin{bmatrix} 1 & -\tilde{\gamma} \\ -\tilde{\gamma} & 1 \end{bmatrix}^{-1}\begin{bmatrix} x_i x_i & x_i x_{iaa} \\ x_i x_{ibb} & x_{icc}x_{idd} \end{bmatrix}\right\} + \frac{d(d+2)(d+4)}{6}\bar{x}_{jkl}\bar{x}_{jkl}, \tag{A18}$$

where summation is assumed over repeated indices, and $\bar{x}_{ijk} = x_{ijk} - 3x_{aa(i}\delta_{jk)}/(d+2)$ is the traceless part of x_{ijk}. Given that we have d traces of x_{ijk}, and that the space of traceless symmetric tensors of the order of 3 is of dimension $w_3 = d(d+1)(d+2)/6 - d = d(d-1)(d+4)/6$, one expects the determinant of $\widetilde{\boldsymbol{\Sigma}}$ to show factors $(1-\tilde{\gamma})^d\,(d(d+2)(d+4))^{-w_3}$. Indeed, calculations similar to (but more cumbersome than) those of Appendix A2 yield

$$|\widetilde{\boldsymbol{\Sigma}}| = 3^d 2^{d(d-1)}(1-\tilde{\gamma})^d\,(d(d+2)(d+4))^{-w_3}\,(d^2(d+2))^{-d}.$$

Together with equations (A17) and (A18), this fully describes the joint distribution of first and third derivatives of the field. In the following, we will compute the conditional statistics needed for the term C_{odd}.

A3.2 Conditional statistics needed for C_{odd}

First, let us note that the first derivatives are Gaussian distributed with individual variance $\langle x_i^2\rangle = 1/d$ so that the probability density of first derivatives near the configuration when they all vanish is

$$P(x_i = 0) = \left(\frac{d}{2\pi}\right)^{d/2}. \tag{A19}$$

Now let us specify the different statistics of the third derivatives. By symmetry, one can note that

$$\left\langle\left(\sum_i x_{1ii}\right)^2\right\rangle = \frac{1}{d}, \tag{A20}$$

since the third derivatives are rescaled by σ_3, and

$$\langle x_{1jj}^2\rangle = \langle x_{111}x_{1jj}\rangle = \frac{1}{5}\langle x_{111}^2\rangle = 3\langle x_{1jj}x_{1kk}\rangle \quad \forall j \ne k \ne 1.$$

Therefore,

$$\frac{1}{d} = \langle x_{111}^2\rangle + (d-1)\langle x_{1jj}^2\rangle + 2(d-1)\langle x_{111}x_{1jj}\rangle + (d-1)(d-2)\langle x_{1kk}x_{1jj}\rangle \quad \forall j \ne k \ne 1$$

implies that $\langle x_{iii}^2\rangle = 15/d(d+2)(d+4)$ and all terms of the third derivatives covariance have been specified.

However, we are interested in statistics subject to a zero gradient constraint, in particular the three quantities of interest are (choosing the last dimension d as the degenerate one and assuming an implicit summation on the i indices)

$$\langle x_{ddd}^2|x_d = 0\rangle = \langle x_{ddd}^2\rangle - \frac{\langle x_{dii}x_d\rangle^2}{\langle x_d^2\rangle}, \tag{A21}$$

$$\langle (x_{dii})^2\,|x_d = 0\rangle = \langle (x_{dii})^2\rangle - \frac{\langle x_{ddd}x_d\rangle^2}{\langle x_d^2\rangle}, \tag{A22}$$

$$\langle x_{dii}x_{ddd}|x_d = 0\rangle = \langle x_{dii}x_{ddd}\rangle - \frac{\langle x_d x_{ddd}\rangle\langle x_d x_{dii}\rangle}{\langle x_d^2\rangle}, \tag{A23}$$

which can easily be computed thanks to the additional relation $\langle x_{ii}^2\rangle = 3/d(d+2)$:

$$\langle x_{ddd}^2|x_d = 0\rangle = \frac{3}{d(d+2)}\left[\frac{5}{d+4} - \frac{3\tilde{\gamma}^2}{d+2}\right], \tag{A24}$$

$$\langle (x_{dii})^2\,|x_d = 0\rangle = \frac{1-\tilde{\gamma}^2}{d}, \tag{A25}$$

$$\langle x_{dii}x_{ddd}|x_d = 0\rangle = \frac{3}{d(d+2)}(1-\tilde{\gamma}^2). \tag{A26}$$

A4 Critical event number counts in ND

It now follows that the critical event number counts of type j at height ν in dimension d reads

$$n^{(j)}_{d,\mathrm{ce}}(\nu) = \frac{R}{\tilde{R}^2 R^d_*} C^d_{\mathrm{odd}} C^d_{j,\mathrm{even}}(\nu)\,. \tag{A27}$$

The contribution from the odd part of the distribution function, $C_{d,\,\mathrm{odd}}$, depends on whether we consider total critical point count or net merger events, but can be obtained in a closed analytical form for arbitrary d in both cases.

To count net merger events as defined in equation (14), we evaluate $C_{d,\,\mathrm{odd}}$ as

$$C^d_{\mathrm{odd}} = \left\langle \sum_i x_{jii}\, x_{jjj} \delta^{(d)}_{\mathrm{D}}(x_i) \right\rangle . \tag{A28}$$

where the expectation in equation (A28) should be computed using the results for odd-order derivatives given in Appendix A3. Note that due to symmetries, the result does not depend on j. Using equations (A19) and (A24), we obtain

$$C^d_{\mathrm{odd}} = \frac{3}{d(d+2)} \left(\frac{d}{2\pi}\right)^{d/2} (1-\tilde{\gamma}^2), \tag{A29}$$

which is analogous to equation (39) in d dimensions.

If we are counting total density of critical events instead (equation 11 in d dimensions), one is led to introduce

$$C^{\mathrm{ce},d}_{\mathrm{odd}} = \left\langle \left| \sum_i x_{jii} \right| |x_{jjj}| \delta^{(d)}_{\mathrm{D}}(x_i) \right\rangle , \tag{A30}$$

where, once again, the final results do not depend on j. After a bit of algebra,

$$C^{\mathrm{ce},d}_{\mathrm{odd}} = \left(\frac{d}{2\pi}\right)^{d/2} \frac{2\sqrt{6}}{\pi} \sqrt{\frac{(d-1)\left(1-\tilde{\gamma}^2\right)}{d^2(d+2)^2(d+4)}} + \left(\frac{d}{2\pi}\right)^{d/2} \frac{6\left(1-\tilde{\gamma}^2\right)}{\pi d(d+2)} \tan^{-1}\left(\sqrt{\frac{3}{2}} \frac{\sqrt{d+4}\sqrt{1-\tilde{\gamma}^2}}{\sqrt{d-1}}\right). \tag{A31}$$

The contribution from the even, density-threshold-dependent term, $C^d_{j,\mathrm{even}}(\nu)$, is given by

$$C^d_{j,\mathrm{even}}(\nu) = \left\langle \delta_{\mathrm{D}}(x-\nu)\delta_{\mathrm{D}}(\lambda_j) \left| \prod_{i\neq j} \lambda_i \right| \right\rangle , \tag{A32}$$

where the condition of critical point of type j refers to the vanishing eigenvalue in the ordered list $\lambda_1 \leq \lambda_2 \leq \ldots \leq \lambda_d$, and $j = d$ corresponds to peak-filament mergers. The expectation value in equation (A32) is computed using the distribution function in equation (A3).

$C^d_{j,\mathrm{even}}(\nu)$ is a non-trivial function of ν because of the correlation between ν and $\sum_i \lambda_i$ seen in equation (A4). It does not allow for an exact analytical form; however, we can obtain the asymptotic behaviour of $C^d_{j,\mathrm{even}}(\nu)$ at large overdensities ν, as will be shown below. The PDFs of total critical events in 3+1D, 4+1D, and 5 + 1D can be obtained numerically using equations (A3), (A27), and (A29), and are shown in Fig. A1. Note that the intermediate signature events dominate in number over the extreme ones, in accordance with the relative number of critical points.

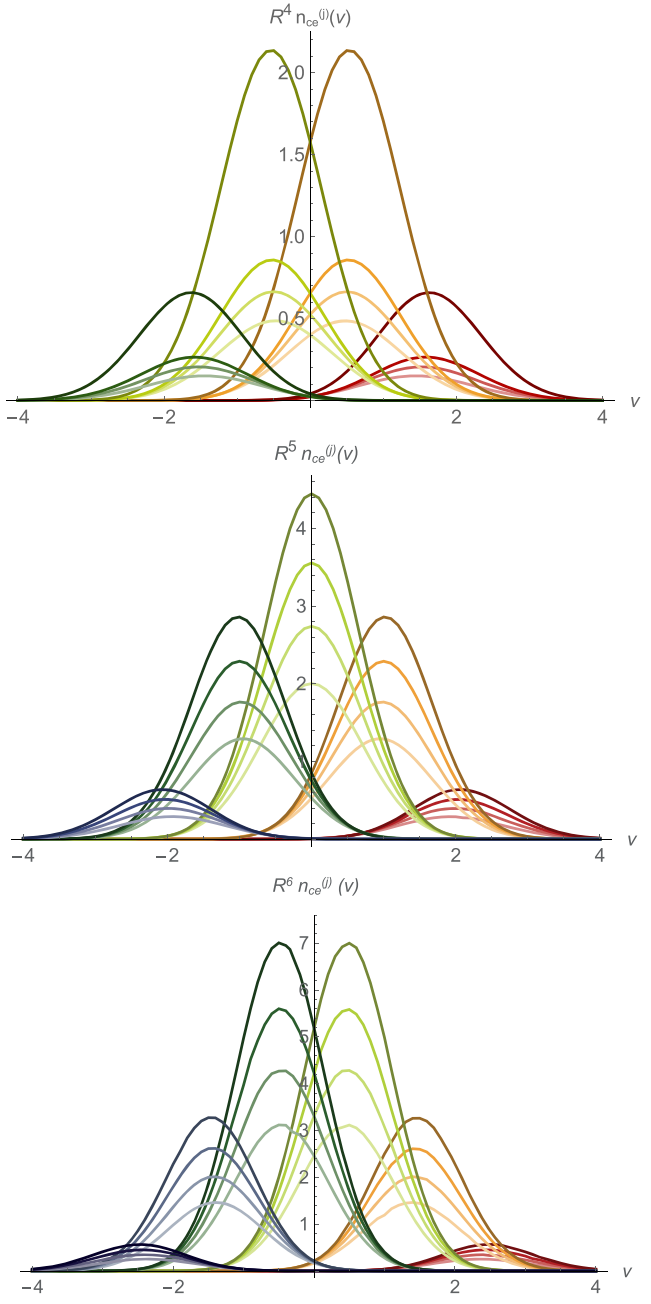

Figure A1. The PDF of critical events of the various types ($\mathcal{P}$, $\mathcal{F}$, $\mathcal{W}_1$, $\mathcal{W}_2$) in 3 + 1D (top panel), 4 + 1D (middle panel), and 5 + 1D (bottom panel) for $n_{\mathrm{s}} = -2, -3/2, -1, -1/2$ from light to dark.

A5 Asymptotics

In the large ν limit, the number density of peak-filament mergers in d dimensions will now be shown to scale like

$$C^d_{j,\mathrm{even}}(\nu) \underset{\gamma\nu\to\infty}{\propto} (\gamma\nu)^{2(d-1)} \exp\left(-\frac{1}{2}\frac{\nu^2}{1-\frac{d+2}{3d}\gamma^2}\right). \tag{A33}$$

To get to equation (A33), first note that in d dimensions, the average over the full range of eigenvalues of any monomial $\prod_i \lambda_i^{n_i}$ behaves

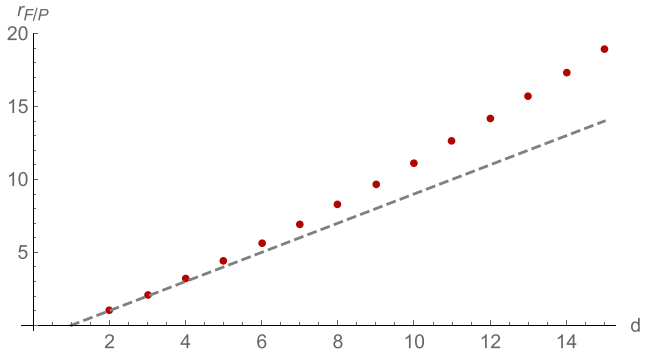

Figure A2. The ratio of peak to filament merger as a function of d. For reference, the first diagonal is shown as a dashed grey line as well. The ratio is approximately fitted as $d-1+((2d-4)/7)^{7/4}/2$ and shown as red dots. The dashed line is the identity.

as

$$\left\langle \prod_i \lambda_i^{n_i} \right\rangle \propto (\gamma\nu)^{\sum_i n_i} \mathrm{e}^{-\nu^2/2} \tag{A34}$$

in the high-ν limit. This follows from rewriting the exponential argument in equations (A4) and (A5) of the distribution in equation (A3) in terms of uncorrelated d-dimensional Hessian invariants (Pogosyan et al. 2009a) $J_1^{(d)} = \sum_i \lambda_i$ and $J_2^{(d)} = \left(\sum_i \lambda_i\right)^2 - \frac{2d}{d-1}\sum_{i<j}\lambda_i\lambda_j$ as

$$Q_d(\nu, \boldsymbol{\lambda}) = \frac{1}{2}(d+2)(d-1)J_2^{(d)}\,, \tag{A35}$$

so that

$$Q_\gamma(\nu, \boldsymbol{\lambda}) = \nu^2 + \frac{\left(J_1^{(d)} + \gamma\nu\right)^2}{(1-\gamma^2)} + \frac{1}{2}(d+2)(d-1)J_2^{(d)}\,, \tag{A36}$$

where $J_2^{(d)}$ is also uncorrelated with the overdensity ν. In the limit $\nu \to \infty$, $J_1^{(d)} \to -\infty$ and if all eigenvalues λ_i are unrestricted, the exact boundaries of integration in λ_i space become irrelevant. The average over $J_1^{(d)}$ and $J_2^{(d)}$ gives a power law in ν, while the factored out ν^2 term in Q_γ is responsible for the exponential 'controlling factor' of the asymptotic behaviour $\mathrm{e}^{-\nu^2/2}$. A classical example of this situation is found in the peak counts (Bardeen et al. 1986). For high peaks, all eigenvalues tend to be large and negative, and asymptotically yield equation (A34).

The situation changes when one or more eigenvalues are restricted to remain small and/or positive. This is the case for critical events where $\lambda_j = 0$, and thus $\lambda_i \geq 0$ for all $i \geq j$. In the $\nu \to \infty$, $J_1^{(d)} \to -\infty$ limit, only the subset of $j-1$ eigenvalues $\lambda_{i<j}$ becomes large and negative, so the average over the Hessian terms is effectively restricted to a subspace of dimension $j-1$. This affects the asymptotics, since $J_1^{(d)}$ and $J_2^{(d)}$ are correlated when projected to a lower dimensional hypersurface. Instead, we need to rewrite the PDF using combinations of $J_1^{(j-1)}$ and $J_2^{(j-1)}$.

In the case of peak filament critical events $j = d$. Setting $\lambda_d = 0$ leads to the following transformation:

$$J_1^{(d)} \to J_1^{(d-1)}\,, \text{ but } J_2^{(d)} \to \frac{1}{(d-1)^2}J_1^{(d-1)} + \frac{d(d-2)}{(d-1)^2}J_2^{(d-1)}\,,$$

which displays a coupling to J_1. Closing the square term for $J_1^{(d-1)}$ in equation (A36) now gives

$$\mathcal{Q}_\gamma(\{\lambda_{d-1}\}, 0) = \frac{3d}{3d-(d+2)\gamma^2}\nu^2 + \frac{d(d-2)(d+2)}{2(d-1)}J_2^{(d-1)} + \left(J_1^{(d-1)} + \frac{2(d-1)\gamma\nu}{3d-(d+2)\gamma^2}\right)^2 \frac{3d-(d+2)\gamma^2}{2(d-1)(1-\gamma^2)}. \tag{A37}$$

which yields a new coefficient in front of ν^2. The averaging in equation (A32) leaves this term as controlling the exponential factor of the $\nu \to \infty$ asymptote, and yields a polynomial in $\gamma\nu$ scaling like $\propto (\gamma\nu)^{2(d-1)}$, as stated in equation (A33), given that the Dirac in λ_d changes the measure $\prod_{i<j\leq d}(\lambda_i - \lambda_j)$ to $\prod_{i<j\leq d-1}(\lambda_i - \lambda_j) \times \prod_{i<d}\lambda_i$, hence the extra factor $(\gamma\nu)^{(d-1)}$.

Incidentally, a similar situation arises when computing the number density of filamentary saddle points (Gay et al. 2012), where the largest eigenvalue, though not zero, is still restricted to positive values, leading to an effective change of dimension by 1, and asymptotes with the same exponential behaviour as equation (A33).

A6 Ratios of critical events

From equation (A3), the integration over ν yields the marginal probability of $\boldsymbol{\lambda}$, which, up to a multiplicative constant, reads

$$\prod_{i\leq d} d\lambda_i \prod_{i<j}(\lambda_j - \lambda_i)\exp\left(-\frac{1}{2}\mathcal{Q}_d(\boldsymbol{\lambda}) - \frac{1}{2}\left(\sum_i \lambda_i\right)^2\right). \tag{A38}$$

Finally, the d-dimensional ratio of critical events of type j and k is simply given by

$$r_{j/k} = \left\langle \delta_{\mathrm{D}}(\lambda_j)\prod_{i\neq j}|\lambda_i| \right\rangle \Big/ \left\langle \delta_{\mathrm{D}}(\lambda_k)\prod_{i\neq k}|\lambda_i| \right\rangle,$$

where the PDF to evaluate this expectation is given by equation (A38). Note that these counts correspond to the area below each curve shown in Fig. A1. In 2 + 1D, we recover the ratio presented in the main text. In 3 + 1D, the ratio is analytic and reads $2(57+25\pi-50\cot^{-1}(3))/(75\pi-2(57+50\cot^{-1}(2))) \approx 3.17$. More generally,

$$\begin{aligned}
d=2:&\quad r_{\mathcal{F}/\mathcal{W}} = 1\,,\\
d=3:&\quad r_{\mathcal{F}/\mathcal{P}} = 2.06\,,\\
d=4:&\quad r_{\mathcal{F}/\mathcal{P}} = 3.17\,,\quad r_{\mathcal{W}/\mathcal{P}} = 3.17\,,\\
d=5:&\quad r_{\mathcal{F}/\mathcal{P}} = 4.36\,,\quad r_{\mathcal{W}_1/\mathcal{P}} = 6.72\,,\quad r_{\mathcal{W}_2/\mathcal{P}} = 4.36\,,\\
d=6:&\quad r_{\mathcal{F}/\mathcal{P}} = 5.67\,,\quad r_{\mathcal{W}_1/\mathcal{P}} = 11.97\,,\quad r_{\mathcal{W}_2/\mathcal{P}} = 11.97,
\end{aligned}$$

and $r_{\mathcal{W}_3/\mathcal{P}} = 5.67$. Note that these ratios are pure numbers and do not depend on the detailed shape of the underlying power spectrum.

A7 Self-consistency links with critical points counts

The results of this paper can be used to derive the connectivity as defined in Codis et al. (2018). Indeed, let us formally write $n_{\mathrm{cp}}^{(i)}$ the number density of critical point of kind i in d dimensions and $n_{\mathrm{me}}^{(i)}$ the net number density of critical event of kind $d-i+1$. The evolution of $n_{\mathrm{cp}}^{(i)}$ is given by

$$\frac{\mathrm{d}n_{\mathrm{cp}}^{(i)}}{\mathrm{d}R} = -\begin{cases} n_{\mathrm{me}}^{(1)} & \text{if } i=0,\\ n_{\mathrm{me}}^{(i)} + n_{\mathrm{me}}^{(i+1)} & \text{if } 0<i<d-1,\\ n_{\mathrm{me}}^{(d)} & \text{if } i=d-1. \end{cases} \tag{A39}$$

For Gaussian random fields, the number density of critical point can be formally written as

$$n_{\rm cp}^{(i)} = \frac{1}{R_*^d} \underbrace{\left\langle \left| \prod_j \lambda_j \right| \right\rangle \left\langle \delta_{\rm D}^{(3)}(x_i) \right\rangle}_{C_i},$$

where the PDF to evaluate the left-hand part of the right-hand side is given by equation (A38). Here C_i is a number common to all power spectra. The derivative of $n_{\rm cp}^{(i)}$ with respect to the smoothing scale is then

$$\frac{{\rm d}n_{\rm cp}^{(i)}}{{\rm d}R} = -n_{\rm cp}^{(i)} \times d \frac{{\rm d}\log R_*}{{\rm d}R}. \tag{A40}$$

Using equations (A39) and (A40) yields a simple relation between the number density of critical points and the number density of critical events:

$$n_{\rm cp}^{(i)} = \frac{1}{d \times {\rm dlog}\, R_*/{\rm d}R} \begin{cases} n_{\rm me}^{(1)} & \text{if } i = 0, \\ n_{\rm me}^{(i)} + n_{\rm me}^{(i+1)} & \text{if } 0 < i < d-1, \\ n_{\rm me}^{(d)} & \text{if } i = d-1. \end{cases}$$

For Gaussian random fields, one has the property that $n_{\rm cp}^{(i)} = n_{\rm cp}^{(d-i)}$ (with $i \in \{0, \ldots, d\}$), and $n_{\rm me}^{(i)} = n_{\rm me}^{(d-i+1)}$ (with $i \in \{1, \ldots, d\}$).

This provides us with simple way to compute the ratio of critical events as a function of the ratio of the critical points. For any d, the ratio of filament to peak is connected to the ratio of $\mathcal{F}$ to $\mathcal{P}$ critical events:

$$\frac{n_{\rm cp}^{\rm f}}{n_{\rm cp}^{\rm p}} = \frac{n_{\rm me}^{\mathcal{P}} + n_{\rm me}^{\mathcal{F}}}{n_{\rm me}^{\mathcal{F}}} = 1 + r_{\mathcal{F}/\mathcal{P}}. \tag{A41}$$

As an example, let use derive the ratio of other critical points in dimensions up to 6D. For $d = 4$,

$$\frac{n_{\rm cp}^{\rm f}}{n_{\rm cp}^{\rm p}} = \frac{n_{\rm cp}^{(1)}}{n_{\rm cp}^{(0)}} = 1 + r_{\mathcal{F}/\mathcal{P}} \approx 4.17,$$
$$\frac{n_{\rm cp}^{(2)}}{n_{\rm cp}^{(1)}} = \frac{n_{\rm me}^{(1)} + n_{\rm me}^{(2)}}{n_{\rm me}^{(0)} + n_{\rm me}^{(1)}} = \frac{n_{\rm me}^{(0)} + n_{\rm me}^{(1)}}{n_{\rm me}^{(0)} + n_{\rm me}^{(1)}} = 1.$$

For $d = 5$,

$$\frac{n_{\rm cp}^{\rm f}}{n_{\rm cp}^{\rm p}} = \frac{n_{\rm cp}^{(1)}}{n_{\rm cp}^{(0)}} = 1 + r_{\mathcal{F}/\mathcal{P}} \approx 5.36,$$
$$\frac{n_{\rm cp}^{(2)}}{n_{\rm cp}^{(1)}} = \frac{n_{\rm cp}^{(2)}}{n_{\rm cp}^{(3)}} = \frac{n_{\rm me}^{(1)} + n_{\rm me}^{(2)}}{n_{\rm me}^{(0)} + n_{\rm me}^{(1)}} = \frac{r_{\mathcal{F}/\mathcal{P}} + r_{\mathcal{W}_1/\mathcal{P}}}{1 + r_{\mathcal{F}/\mathcal{P}}} \approx 2.07.$$

For $d = 6$,

$$\frac{n_{\rm cp}^{\rm f}}{n_{\rm cp}^{\rm p}} = \frac{n_{\rm cp}^{(1)}}{n_{\rm cp}^{(0)}} = 1 + r_{\mathcal{F}/\mathcal{P}} \approx 6.67,$$
$$\frac{n_{\rm cp}^{(2)}}{n_{\rm cp}^{(1)}} = \frac{n_{\rm cp}^{(3)}}{n_{\rm cp}^{(4)}} = \frac{n_{\rm me}^{(1)} + n_{\rm me}^{(2)}}{n_{\rm me}^{(0)} + n_{\rm me}^{(1)}} = \frac{r_{\mathcal{F}/\mathcal{P}} + r_{\mathcal{W}_1/\mathcal{P}}}{1 + r_{\mathcal{F}/\mathcal{P}}} \approx 2.64,$$
$$\frac{n_{\rm cp}^{(3)}}{n_{\rm cp}^{(2)}} = 1.$$

Note that in the previous expressions, we have used the following substitutions $n_{\rm cp}^{\rm p} \equiv n_{\rm cp}^{(d)}$ and $n_{\rm cp}^{\rm f} \equiv n_{\rm cp}^{(d-1)}$ and the fact that $n_{\rm cp}^{(d)} = n_{\rm cp}^{(0)}$ and $n_{\rm cp}^{(d-1)} = n_{\rm cp}^{(1)}$ Given that Codis et al. (2018) provide an asymptotic limit for the global connectivity $\kappa \equiv 2n_{\rm cp}^{\rm f}/n_{\rm cp}^{\rm p}$, we can re-express it in terms of the ratio of critical events as

$$\frac{n_{\rm cp}^{\rm f}}{n_{\rm cp}^{\rm p}} = \frac{n_{\rm cp}^{(1)}}{n_{\rm cp}^{(0)}} = 1 + r_{\mathcal{F}/\mathcal{P}} \sim d + \frac{1}{2}\left((2d-4)/7\right)^{7/4}, \tag{A42}$$

which, in the large d limit, asymptotes approximately to

$$r_{\mathcal{F}/\mathcal{P}} \overset{d\to\infty}{\sim} \frac{1}{2}\left(\frac{2}{7}\right)^{7/4} d^{7/4} \approx \frac{1}{17} d^{7/4}. \tag{A43}$$

A8 Testing the link between critical points and events counts

From equation (A40) and because for a Gaussian filter, we have

$$\frac{{\rm d}\sigma_i^2}{{\rm d}R^2} = -\sigma_{i+1}^2,$$

one can easily derive

$$\frac{{\rm d}n_{\rm cp}^{(i)}}{{\rm d}R} = -n_{\rm cp}^{(i)} \times d \frac{R}{R_\star^2} \frac{1-\tilde{\gamma}^2}{\tilde{\gamma}^2}. \tag{A44}$$

which, in $d = 3$ for peaks, reads

$$-\frac{{\rm d}n_{\rm cp}^{\rm p}}{{\rm d}R} = 3n_{\rm cp}^{\rm p} \frac{R}{R_\star^2} \frac{1-\tilde{\gamma}^2}{\tilde{\gamma}^2} \tag{A45}$$
$$= \frac{3R}{R_\star^3 \tilde{R}^2}(1-\tilde{\gamma}^2) \frac{29\sqrt{15} - 18\sqrt{10}}{1800\pi^2}, \tag{A46}$$

which is equal to the net merger rate of peak type from equation (21) with $C_{\rm even}$ and $C_{3,\,\rm odd}$ given by equations (24) and (25), respectively.

APPENDIX B: RATE OF CHANGE WITH SMOOTHING

Let us show how the 3 + 1D number density of critical events is related to the rate of change of the 3D density of critical points with R, ${\rm d}n_{\rm cp}/{\rm d}R$. The 3D density of critical points is defined as

$$n_{\rm cp}(R) \equiv \left\langle \sum_{\rm cp} \delta_{\rm D}(\boldsymbol{r} - \boldsymbol{r}_{\rm cp}) \right\rangle, \tag{B1}$$

where the sum runs over the solutions $\boldsymbol{r}_{\rm cp}$ of the equation $\nabla\delta = 0$, H is the Hessian determinant, and brackets designate spatial averages on a 3D slice, $\langle \ldots \rangle \equiv \frac{1}{V}\int_V \ldots {\rm d}^3\boldsymbol{r}$. Critical points of a given kind (peak, saddle, or minimum) can be defined by further imposing the signs of the eigenvalues of the Hessian.

Outside the critical events, the trajectory of each critical point in the extended 3 + 1D space obtained by stacking spatial slices at different smoothing scales can be parametrized by R to yield the 3 + 1D coordinates $(\boldsymbol{r}_{\rm cp}(R), R)$. The equation for $\boldsymbol{r}_{\rm cp}(R)$ is obtained by requiring that the field gradient $\nabla\delta(\boldsymbol{r} = \boldsymbol{r}_{\rm cp}(R), R)$ be constant, which gives

$$\frac{{\rm d}\boldsymbol{r}_{\rm cp}}{{\rm d}R} = -\partial_R \nabla\delta \cdot \mathbf{H}^{-1}\big|_{\boldsymbol{r}=\boldsymbol{r}_{\rm cp}}. \tag{B2}$$

If one considers a single critical point, its contribution to the integral count is seemingly preserved along the track at 1, $\int {\rm d}^3\boldsymbol{r}\delta_{\rm D}(\boldsymbol{r} - \boldsymbol{r}_{\rm cp}) = 1$. Thus, if this was valid for all trajectories at every R, we would obtain a puzzling and incorrect conclusion that the number of critical points is conserved with varying smoothing. However, only trajectories that do not encounter a critical event can be continuously parametrized with R everywhere. At the critical event, a 3 + 1D geometrical line tracking the critical point turns around and continues back in reverse direction in R with a change of sign in H, and the R parametrization breaks. Equivalently, the lines of two critical points of different types with opposite signs of H (now both taken in the same R direction) meet and terminate. It can be shown that the merging of two branches is smooth to first order, but when parametrized in R, ${\rm d}\boldsymbol{r}_{\rm cp}/{\rm d}R$ diverges at the critical event and has opposite signs on the two branches (see Appendix D). This

clearly demonstrates why it is the critical events that are responsible for critical point number changes with smoothing.

To resolve this difficulty, we shall consider counting only half of the critical points, e.g. the ones with positive H (i.e. minima and filamentary saddle points in 3D). The other half, with negative H, has the same average number density due to the null Euler characteristic of the space, so that the total density is twice that of critical points with $H > 0$. Since the two sides of each merging pair of tracks have opposite H signs, this leaves us with only one of the two branches terminating at any critical event. So we have tracks that go forever, and tracks that terminate at critical events, but along all of them, R is a suitable parameter, since there is no backwinding.

Thus, we can compute the change with R of the density of critical points as

$$\frac{\mathrm{d}n_{\mathrm{cp}}}{\mathrm{d}R} = 2\frac{\mathrm{d}}{\mathrm{d}R}\left\langle \sum_{\mathrm{cp}} \delta_{\mathrm{D}}^{(3)}(\boldsymbol{r}-\boldsymbol{r}_{\mathrm{cp}})\Theta_{\mathrm{H}}(H(\boldsymbol{r}_{\mathrm{cp}},R))\right\rangle, \tag{B3}$$

and differentiating under the averaging operation, we find

$$\frac{\mathrm{d}n_{\mathrm{cp}}}{\mathrm{d}R} = 2\left\langle \sum_{\mathrm{cp}} \delta_{\mathrm{D}}^{(3)}(\boldsymbol{r}-\boldsymbol{r}_{\mathrm{cp}})\frac{\mathrm{d}}{\mathrm{d}R}\Theta_{\mathrm{H}}\left(H(\boldsymbol{r}_{\mathrm{cp}},R)\right)\right\rangle. \tag{B4}$$

Note that the contribution from Dirac's delta function vanishes, since $\mathrm{d}\delta_{\mathrm{D}}^{(3)}(\boldsymbol{r}-\boldsymbol{r}_{\mathrm{cp}})/\mathrm{d}R = -\mathrm{d}\boldsymbol{r}_{\mathrm{cp}}/\mathrm{d}R\cdot\nabla_{\boldsymbol{r}}\delta_{\mathrm{D}}^{(3)}(\boldsymbol{r}-\boldsymbol{r}_{\mathrm{cp}})$, and there is no $\boldsymbol{r}$ dependence left for the gradient to act on after integrating by parts.

Next we express the full derivative $\mathrm{d}H(\boldsymbol{r}_{\mathrm{cp}}(R),R)/\mathrm{d}R$ via field variables using equation (B2), and use the representation $\sum_{\mathrm{cp}}\delta_{\mathrm{D}}^{(3)}(\boldsymbol{r}-\boldsymbol{r}_{\mathrm{cp}}) = |H|\delta_{\mathrm{D}}(\nabla\delta)$ on a fixed R slice, to obtain

$$\frac{\mathrm{d}n_{\mathrm{cp}}}{\mathrm{d}R} = 2\left\langle |H|(\partial_R H - \partial_R\nabla\delta\cdot\mathbf{H}^{-1}\cdot\nabla H)\delta_{\mathrm{D}}^{(3)}(\nabla\delta)\delta_{\mathrm{D}}(H)\right\rangle,$$

having replaced volume averaging by ensemble averaging over the field distribution. Here the expression is understood as the $H\to 0^{+}$ limit, i.e. approaching the critical events along the positive H tracks. This allows us to replace the absolute value $|H|$ by H itself.[19] In the term $H(\partial_R H - \partial_R\nabla\delta\cdot\mathbf{H}^{-1}\cdot\nabla H)$, we recognize the $3+1$D Jacobian of equation (10), and finally obtain

$$\frac{\mathrm{d}n_{\mathrm{cp}}}{\mathrm{d}R} = 2\left\langle J\ \delta_{\mathrm{D}}^{(3)}(\nabla\delta)\delta_{\mathrm{D}}(H)\right\rangle. \tag{B5}$$

In this expression, the factor of 2 reflects the fact that each critical event affects two critical points; the appearance of J, rather than its absolute value $|J|$, and the fact that different critical events change the number of critical points according to the sign of J. Critical points are created at a critical event if J is positive, and destroyed if J is negative. Averaging over all J's in equation (B5) counts the balance of sources and sinks.

It is interesting to notice the analogy of equation (B5) with the Press–Schechter expression for the crossing rate of random walks through a threshold. Here the threshold is $H = 0$ rather than $\delta = \delta_{\mathrm{c}}$, and the random walks follow the critical point lines, but the crossing rate is still the total derivative of the probability of being above threshold, as in equation (B3), and it equals the expectation value of the derivative $\mathrm{d}H/\mathrm{d}R$ at $H = 0$ over all possible trajectories, i.e. $n_{\mathrm{ce}}^{\mathrm{3D}}$. The upcrossing probability (a better approximation to the first crossing rate, where up is meant towards smaller scales) is, on the other hand, the expectation value over trajectories with negative derivative only, and is therefore analogous to $n_{\mathrm{ce},-}^{\mathrm{3D}}$.

[19]Using tracks with negative H would lead to the same result due to the minus sign after differentiating $\Theta_{\mathrm{H}}(-H)$ and confirming that $\lim_{H\to 0^{-}}(-|H|\mathbf{H}^{-1}) = \lim_{H\to 0^{+}}|H|\mathbf{H}^{-1} = \lim_{H\to 0} H\mathbf{H}^{-1}$.

APPENDIX C: DUALITY IN EVENTS RANKING

In this paper and unless stated otherwise, the physical interpretation of critical events was done from the perspective of the densest structure. From this point of view, $\mathcal{P},\mathcal{F},\mathcal{W}$ critical events are interpreted as peak (proto-halo) mergers, filament, and wall mergers, respectively. It is however also possible to interpret critical events from the perspective of the least dense structure, in which case $\mathcal{P},\mathcal{F},\mathcal{W}$ critical events are interpreted as filament, wall, and void mergers, respectively. In order to illustrate this, let us focus on the central panel of Fig. C1, which illustrates an $\mathcal{F}$ critical event. Before the critical event, the topology of the field is described, from the left- to right-hand side, by a wall-type saddle point (W_1), a filament-type saddle point (F_1), a wall-type saddle point (W_2), and a filament-type saddle point (F_2). The critical event records the merger of F_1 with W_2. Now, in order to interpret the critical event in astrophysical terms, one is left with a choice of associating the merger to the surviving wall (W_1) or the surviving filament (F_2). In the former case, the merger is interpreted as a wall merger, while in the latter, it is interpreted as a filament merger. Note that if one interprets the critical event from the perspective of the disappearing structures instead, e.g. to compute disappearing rates (as is done in Section 5.1), one faces the same dual interpretation as the critical event records the merging of two critical events of different kinds (here, F_1 and W_2).

Wall critical events ($\mathcal{W}$) share a similar dual interpretation. From the point of view of the densest structures – the disappearing wall or the surviving one – the critical event is interpreted as a wall merger, where the void between two walls is crushed. This is illustrated by the red arrow; see the bottom panel of Fig. C1. Conversely, the critical event can be interpreted from the point of view of the least dense structure, i.e. the two voids. In this interpretation, the critical event records a void merger where the surviving void (green arrow) is the

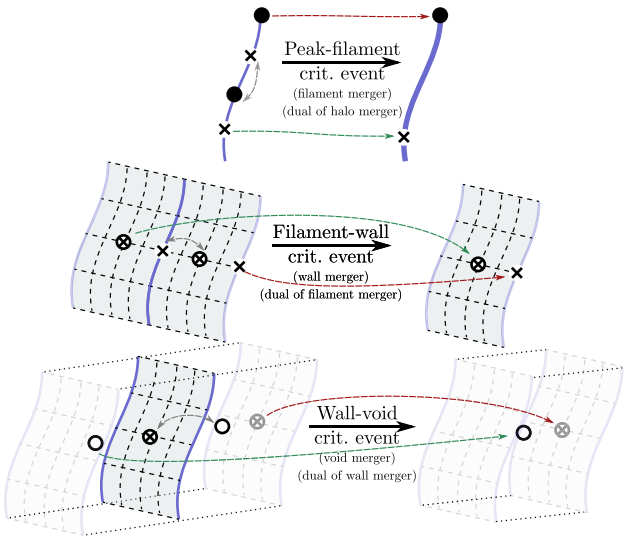

Figure C1. Same as Fig. 4 but interpreted from the point of view of the least massive structure. ● symbols are peaks, × symbols are filament-type saddle points (filament centres), ⊗ symbols are wall-type saddle points (wall centres), and ○ symbols are minima (void centres). Each critical event can be interpreted as the destruction of a pair of critical points (grey arrows) with a surviving structure. In the Fig. 4 description, the merger is associated with the densest surviving structure (peak, filament, and wall mergers; red arrows), while in a dual description, the merger is associated to the least dense surviving structure (filament, wall, and void mergers; green arrows).

result of the central wall being 'swallowed' into the disappearing void (grey arrow).

It is worth noting that this duality follows from self-consistency relations between critical events with connectivity. Indeed, after a critical event, the densest surviving structure (e.g. F_2, or a peak after a $\mathcal{P}$ critical event) becomes connected to the least dense surviving structure on the other side of the critical event (e.g. W_1 or a filament after a $\mathcal{P}$ critical event), each of these two structures being equally valid candidates as the 'astrophysical outcome' of the merger.

Finally, the dual interpretation also reflects the fact that, apart from extrema, all critical points have two channels of destruction. They can merge with a critical point of either the next or the previous kind. For example, a filament can be destroyed in a $\mathcal{P}$ critical event (where a filament between two peaks disappears) or in a $\mathcal{F}$ critical event (where a filament between two walls disappears). This can be mathematically expressed by relating the rate of change of the number density of critical points of a given kind to the number density of critical events (see Appendix A7).

APPENDIX D: LOCAL ANALYSIS OF NUCLEATION

Let us consider the problem of merging or nucleation of a pair of critical points near the critical event $\nabla\delta = 0$, $H = 0$, as one changes the smoothing radius R by ΔR (either positive in case of a nucleation or negative in case of a merger). Smoothing is assumed to be Gaussian. Calculations are done in 2D but are easily generalized to higher dimensions. The 1D case is a special case, with separate conclusions as discussed briefly at the end of this section.

D1 Probing local vicinity of critical events

The idea is to start with a particular, but sufficiently general configuration of the field at smoothing R and see how it changes with smoothing. We take the field at smoothing R to be described by the form

$$\delta_R = \delta_0 + \frac{\delta_{yy}}{2}y^2 + \frac{\delta_{xxx}}{6}x^3 + \frac{\delta_{yyx}}{2}y^2x + \frac{\delta_{xxy}}{2}x^2y + \frac{\delta_{yyy}}{6}y^3, \tag{D1}$$

where δ_R is the field at smoothing R, position x, y, and δ_0 is the field at smoothing R at the origin. Here we have used the short-hand notation $\delta_x = \partial\delta/\partial x$ (and similarly for higher derivatives). This can be viewed as one specific realization of the random field, or as the terms of Taylor expansion up to cubic order near the critical point $x = 0$, $y = 0$, where, with our choice of coordinates,

$$\delta_x = \delta_y = 0, \quad \delta_{xx} = 0\,. \tag{D2}$$

We want to find out under which conditions the shift by ΔR out of a critical event will create two critical points. This can be done by solving the problem perturbatively in ΔR, to the lowest order in ΔR. For this purpose, the terms used in the expression (D1) are sufficient, higher order terms do not modify the result. Given our choice of filtering, the evolution of the field with R is given by the diffusion equation (12). Hence, to first order in ΔR,

$$\delta_{R+\Delta R} \sim \delta_R + R\Delta R\nabla^2\delta_R\,, \tag{D3}$$

with the Laplacian,

$$\nabla^2\delta_R = \delta_{yy} + (\delta_{xxx} + \delta_{yyx})x + (\delta_{yyy} + \delta_{xxy})y\,, \tag{D4}$$

which is to be substituted in equation (D3) for the final form of the field configuration at the shifted smoothing. The shifted field will have extrema where the gradient is zero:

$$\frac{\partial\delta_{R+\Delta R}}{\partial x} = \frac{1}{2}\delta_{xxx}x^2 + \delta_{xxy}xy + \frac{1}{2}\delta_{yyx}y^2 + R\Delta R(\delta_{xxx} + \delta_{yyx}) = 0, \tag{D5}$$

$$\frac{\partial\delta_{R+\Delta R}}{\partial y} = \delta_{yy}y + \frac{1}{2}\delta_{xxy}x^2 + \delta_{yyx}xy + \frac{1}{2}\delta_{yyy}y^2 + R\Delta R(\delta_{xxy} + \delta_{yyy}) = 0. \tag{D6}$$

Since we are looking for appearance of critical points near the critical event, i.e. at position x, y close to 0 as $\Delta R \to 0$, we should solve the system of equations (D5) and D6) perturbatively in ΔR.

We start with the y-derivative, equation (D6). At leading order in y, the terms y^2 and xy can be dropped, leaving us with the following relation:

$$\delta_{yy}y + \frac{1}{2}\delta_{xxy}x^2 \sim -R\Delta R(\delta_{xxy} + \delta_{yyy}). \tag{D7}$$

There are two viable possibilities. Either $y \sim \Delta R$, or $y \sim x^2$. Let us now check equation (D5) for these possibilities. If $y \sim \Delta R$, we see that the xy and y^2 terms are subdominant with respect to the linear $R\Delta R$ term, but if $y \sim x^2$, these same terms are subdominant to x^2. Thus, the xy and y^2 terms can be always neglected, and we find that

$$\frac{1}{2}\delta_{xxx}x^2 \sim -R\Delta R(\delta_{xxx} + \delta_{yyx}), \tag{D8}$$

i.e. we always have a parabolic $x \sim \Delta R^{1/2}$ and $y \sim \Delta R$ behaviour (see Fig. 5). Note that it is not possible to have y subdominant to x^2 or ΔR, since in this case, equations (D7) and (D8) will be in general inconsistent. The solutions to equations (D7) and (D8) are two points (x_+, y) and (x_-, y), where

$$x_\pm = \pm\sqrt{\frac{-2R\Delta R(\delta_{xxx} + \delta_{yyx})}{\delta_{xxx}}}\,, \tag{D9}$$

$$y = -R\Delta R\frac{\delta_{yyx}\delta_{xxy} + \delta_{yyy}\delta_{xxx}}{\delta_{xxx}\delta_{yy}}\,. \tag{D10}$$

For dimensions higher than two, this standard linear dependence appears for all regular directions in which the second derivative of the field at the critical point does not vanish. The only condition for the existence of a pair of extrema near the critical event now arises from requiring that the square root argument in the expression for $x_\pm$ be positive:

$$-2R\Delta R\frac{\delta_{xxx} + \delta_{yyx}}{\delta_{xxx}} > 0\,. \tag{D11}$$

The type of critical points created or merged at a critical event is determined by the signs of the eigenvalues of the Hessian at the critical point locations. The Hessian of the smoothed field is given by

$$\frac{\partial^2\delta_{R+\Delta R}}{\partial x^2} = \delta_{xxx}x + \delta_{xxy}y, \tag{D12}$$

$$\frac{\partial^2\delta_{R+\Delta R}}{\partial y^2} = \delta_{yy} + \delta_{yyx}x + \delta_{yyy}y, \tag{D13}$$

$$\frac{\partial^2\delta_{R+\Delta R}}{\partial x\partial y} = \delta_{xxy}x + \delta_{yyx}y. \tag{D14}$$

Conversely, it is easy to show that to leading order in ΔR, the eigenvalues of the Hessian at the critical points are

$$\lambda_1 = \delta_{xxx}x_\pm = \pm\sqrt{-2R\Delta R\frac{(\delta_{xxx} + \delta_{yyx})}{\delta_{xxx}}}, \tag{D15}$$

$$\lambda_2 = \delta_{yy}. \tag{D16}$$

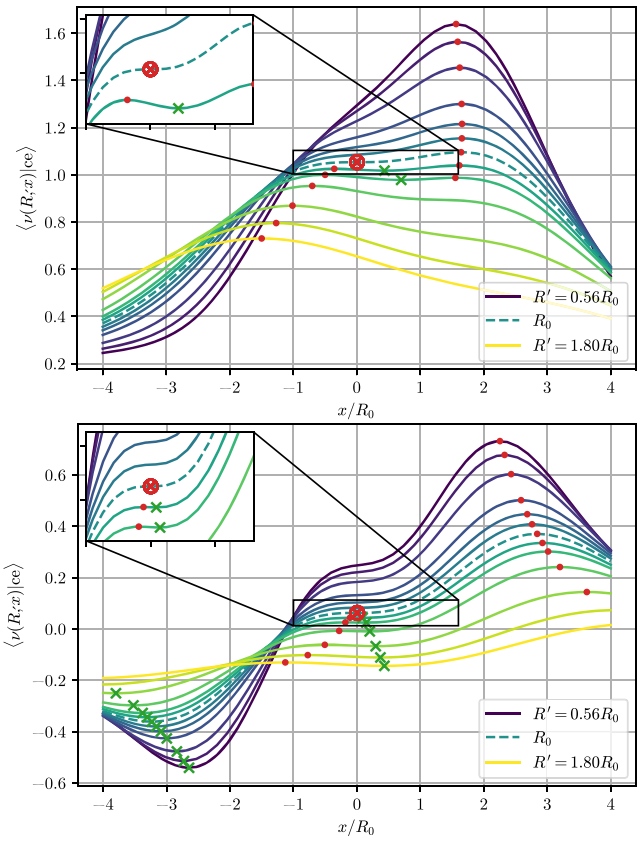

Figure D1. Multiple 1D slices of the conditional mean density field in 3 + 1D at different smoothing scales (from $R' = 0.56$ to $1.80R_0$, equally spaced) around a nucleation critical event (red ⊗ symbol), defined at scale R_0, with peaks (red ● symbols) and filaments (green × symbols) of the 1D slice. The nucleation critical event creates a pair of peak filament that is either shortly destroyed (top panel) or long-lived (bottom panel). The fate of the pair depends on the particular values taken by the field and its derivatives at the critical event.

This explicitly demonstrates that two merging or created critical points in a pair differ in nature with the sign of one eigenvalue. If $\delta_{yy} < 0$ (as well as the rest of the eigenvalues in higher dimensional case), the process describes interaction of one maximum and one filamentary saddle. If $\delta_{yy} > 0$, the process describes the interaction of a minimum and a saddle. In the multidimensional case, it is the set of signs of all non-zero eigenvalues that determine the type of interaction. In 3D, we have three cases: When both eigenvalues are negative, $\delta_{yy} < 0, \delta_{zz} < 0$, it describes maxima and filamentary saddle coalescence; when one is negative and one positive, $\delta_{yy} < 0, \delta_{zz} > 0$, it corresponds to filamentary and wall-like saddles interacting; and when both are positive, $\delta_{yy} > 0, \delta_{zz} > 0$, it corresponds to a wall and a void coalescence. Note that in this discussion, we do not consider eigenvalues as sorted, so the first (degenerate) direction is arbitrary.

D2 Discussion of the existence condition

The merging of a critical point pair corresponds to the situation when two critical points disappeared as smoothing reached R. Thus, two critical points existed for $\Delta R < 0$. This happens when

$$\frac{\delta_{xxx} + \delta_{yyx}}{\delta_{xxx}} > 0. \tag{D17}$$

Conversely, if the solution exists for $\Delta R > 0$, then two critical points appear out of a critical event as smoothing increases from R value. We see that this happens when

$$\frac{\delta_{xxx} + \delta_{yyx}}{\delta_{xxx}} < 0. \tag{D18}$$

This analysis thus proves that the nucleation process is in general possible – even for Gaussian smoothing – if the number of dimensions exceeds one.

The condition on merging or nucleation that we have derived by this local analysis is equivalent to the condition on the sign of the Jacobian defined in equation (10) presented in the main text ($J > 0$ for nucleation and $J < 0$ for merging events), since in our local coordinate representation, the sign-dependent part of this Jacobian is exactly $J \propto -\delta_{xxx}\sum_i \delta_{iix}$. Thus, we conclude that the regions in the space of third derivatives with negative Jacobian describe the merging (disappearance) of peak/saddle pairs, while regions with positive Jacobian describe the creation of peak/saddle pairs.

Note finally that in 1D, we do not have y- or higher directions, so all mixed derivatives vanish. A solution for finding extrema pair requires simply $x_\pm^2 = -2R\Delta R > 0$. This solution exists therefore only for negative ΔR, so in 1D, extrema pairs can only merge and never be created at a critical event if the field is smoothed with Gaussian filters.

Two examples of nucleation are presented on Fig. D1, which shows successive slices of the density field around a nucleation critical event at different smoothing scales. For both plots, the value of the density, its Hessian and third derivative are drawn from a Gaussian PDF until a $\mathcal{P}$ nucleation critical event is found in direction x. These values are then used to constrain the density field at a finite distance and different smoothing scale. The slice direction is oriented parallel to the critical event, so that peaks and minima in each 1D slice coincide at first order with peaks and filaments of the 3D density field.[20] The figure illustrates that pairs of critical points emerging from a nucleation critical event are either long- or short-lived, and an investigation using multiple constrained field showed that the latter is the most common type. Interestingly, it seems that pairs created from a nucleation critical event are very unlikely to annihilate, at least in this somehow contrived setup. A likely astrophysical counterpart to peak nucleation event may be splashback haloes (i.e. the temporary reappearance of a subhalo that as only recently been accreted; Aubert & Pichon 2007; More, Diemer & Kravtsov 2015, and for filament nucleation, the temporary re-appearance of an enclosed wall as two filaments merge, etc.). More work will however be required to astrophysically interpret them and study their properties in the initial density field.

APPENDIX E: EVENT GENERATION ALGORITHM

E1 Constrained field – peak constraint

We have used CONSTRFIELD coupled with MPGRAFIC from Prunet et al. (2008) to generate constrained realizations of a Gaussian random field. We generate an unsmoothed Gaussian random field, constrained to have a filament-type saddle point of height $\delta = 1$ ($\nu = 1.17$) at smoothing scale $R = 5\,\mathrm{Mpc}\,h^{-1}$. The eigenvalues of the Hessian are constrained to be $\{\lambda_1, \lambda_2, \lambda_3\} = \sigma_2\{-1/2, -1/2, -1\}$ with eigenvectors $\{\hat{x}, \hat{y}, \hat{z}\}$. Fig. E1 shows the mean density profiles

[20] As critical points, mostly slide along ridges of the skeleton.

as well as one realization. As expected, the density is locally entirely set by the constraints and has a parabola-like shape. At larger scales, the field decouples from the constraints resulting in large fluctuations around the mean value.

E2 Constrained field – higher order constraints

We developed a code that is able to numerically compute the covariance matrix between any derivative of the field up to third order or any antiderivative of the field up to second order (potential), smoothed by any filter function and at any separation. The code relies on the numerical integration of the correlation function between any two functionals of the field. Formally, let us define a linear functional F and its Fourier representation:

$$\tilde{F}[\delta](\boldsymbol{k}) = \int \mathrm{d}^3\boldsymbol{r} \mathrm{e}^{-i\boldsymbol{k}\cdot\boldsymbol{r}} F[\delta](\boldsymbol{r}). \tag{E1}$$

Functionals that can be written as a convolution with a distribution, which includes notably derivation operators and smoothing operators, can be further simplified as $\tilde{F}[\delta](\boldsymbol{k}) = \delta(\boldsymbol{k})\tilde{F}(\boldsymbol{k})$, where $\tilde{F}$ is now a function of $\boldsymbol{k}$ only. Common operators take a simple form in Fourier space; for example, the third derivative operator in direction i, j, k reads $(-i)^3 k_i k_j k_l$, the shift operator (that shifts the field by $\Delta\boldsymbol{x}$) reads $\exp(i\boldsymbol{k}\cdot\Delta\boldsymbol{x})$, and the Gaussian filter has its usual form $\exp(-k^2R^2/2)$. The covariance between two linear functionals of the field then simply reads

$$\langle F[\delta]G[\delta]\rangle = \frac{1}{(2\pi)^3}\int \mathrm{d}^3\boldsymbol{k} P_k(k)\tilde{F}(\boldsymbol{k})\tilde{G}^\star(\boldsymbol{k}), \tag{E2}$$

where the star symbol denotes here the complex conjugate. As a worked example, the covariance between the field smoothed by a Gaussian filter at scale R_1 at the origin and the field smoothed by a Gaussian filter at scale R_2, position $\boldsymbol{r}$ is given by equation (E2) with $\tilde{F}(\boldsymbol{k}) = \exp(-k^2R_1^2/2)$, and $\tilde{G}(\boldsymbol{k}) = \exp(-k^2R_2^2/2 + i\boldsymbol{k}\cdot\boldsymbol{r})$.

Let us write $\boldsymbol{X} = \{\boldsymbol{X}_1, \boldsymbol{X}_2\}$, where $\boldsymbol{X}_1$ is the density field sampled at p different locations and $\boldsymbol{X}_2$ contains the q values (the field and/or its (anti)derivatives) that will later be constrained to the value $\boldsymbol{a}$.

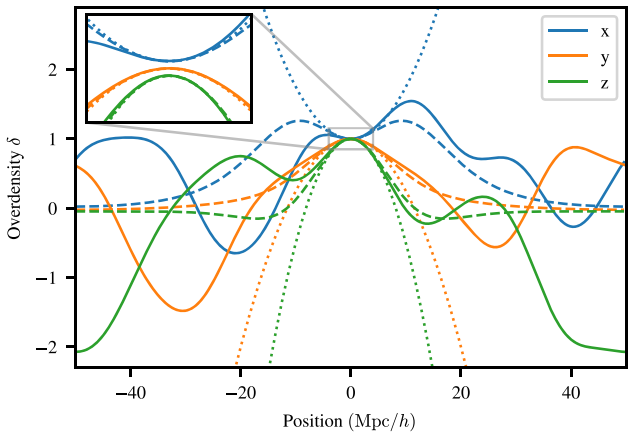

Figure E1. Density profile of a random field constrained to a density $\delta = 1$, null gradient, and a Hessian with eigenvalues $\sigma_2/2, -\sigma_2/2, -\sigma_2$ in directions x, y, z at the centre of the box, assuming periodic boundary conditions. The expectation of the field is shown in dashed lines and the value of the field in one realization is shown in solid lines. Dotted lines show the second-order Taylor series of the field around the constrained point. The inset shows a zoom on the constrained zone. For the sake of clarity, each curve have been shifted by 0.02. At small distances from the constraint, the field resembles its mean and its Taylor expansion.

For example, a critical event constraint (at fixed scale) could be represented by $\boldsymbol{X}_2 = \{x, x_1, x_2, x_3, x_{11}, x_{111}, x_{221}, x_{331}\}$ subject to the constraint $\boldsymbol{a} = \{\nu, 0, 0, 0, 0, \alpha_1, \alpha_2, \alpha_3\}$. The conditional mean $\bar{\boldsymbol{\mu}}$ and covariance $\bar{\mathbf{C}}$ of the field are then obtained from the full mean $\boldsymbol{\mu} = \langle\boldsymbol{X}\rangle$ and covariance $\mathbf{C} = \langle\boldsymbol{X}^{\mathrm{T}}\boldsymbol{X}\rangle$, computed using equation (E2), by simple arithmetic

$$\bar{\boldsymbol{\mu}} = \boldsymbol{\mu}_1 + \mathbf{C}_{12}\mathbf{C}_{22}^{-1}(\boldsymbol{a} - \boldsymbol{\mu}_2), \quad \bar{\mathbf{C}} = \mathbf{C}_{11} - \mathbf{C}_{12}\mathbf{C}_{22}^{-1}\mathbf{C}_{12}^{\mathrm{T}}, \tag{E3}$$

where we assumed here that the covariance is decomposed as $\mathbf{C} = \begin{pmatrix}\mathbf{C}_{11} & \mathbf{C}_{12}\\ \mathbf{C}_{12}^{\mathrm{T}} & \mathbf{C}_{22}\end{pmatrix}$, with sizes $p\times p, p\times q$, and $q\times q$ for C_{11}, C_{12}, and C_{22}, respectively, and similarly for the mean. One can then easily draw samples from the conditional multivariate distribution using $\bar{\boldsymbol{\mu}}$, $\bar{\mathbf{C}}$.

APPENDIX F: PAIR DESTRUCTION AND CREATION COUNTS

Three different definitions of the number count have been discussed in the text and presented in equations (11), (13), and (15). In this section, we present the results obtained in three dimensions for a Gaussian random field using these three definitions. For a Gaussian random field, the expectation of the even derivatives is left unchanged but the odd part is modified.

Using the total merger density definition of equation (11), the odd part reads

$$C_{\mathrm{odd}}^{\mathrm{ce}} = \frac{1}{5}\left(\frac{3}{2\pi}\right)^{3/2}(1-\tilde{\gamma}^2) \times\frac{2}{\pi}\left(\frac{2}{\sqrt{21(1-\tilde{\gamma}^2)}} + \tan^{-1}\frac{\sqrt{21(1-\tilde{\gamma}^2)}}{2}\right). \tag{F1}$$

Using the pair destruction and pair creation definition of equation (13), the odd part reads

$$C_{\mathrm{odd}}^{\mathrm{ce},-} = \frac{1}{5}\left(\frac{3}{2\pi}\right)^{3/2}(1-\tilde{\gamma}^2) \times\frac{1}{\pi}\left(\frac{2}{\sqrt{21(1-\tilde{\gamma}^2)}} + \frac{\pi}{2} + \tan^{-1}\frac{\sqrt{21(1-\tilde{\gamma}^2)}}{2}\right), \tag{F2}$$

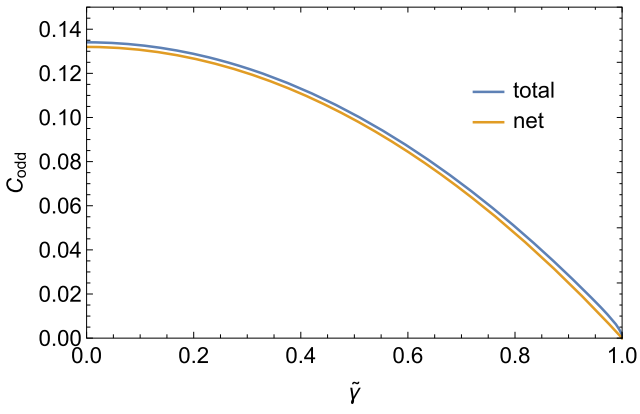

Figure F1. C_{odd} as a function of $\tilde{\gamma}$ when the definition for the total or the net merger density is used. The difference between the two curves is at the per cent level, at least for relatively small values of of $\tilde{\gamma}$. At higher $\tilde{\gamma}$ (typically above 0.8, i.e for a spectral index above -1), both nucleations and destructions become rarer and their ratio tend towards unity.

$$C_{\rm odd}^{\rm ce,+} = \frac{1}{5}\left(\frac{3}{2\pi}\right)^{3/2}(1-\tilde{\gamma}^2) \times \frac{1}{\pi}\left(\frac{2}{\sqrt{21(1-\tilde{\gamma}^2)}} - \frac{\pi}{2} + \tan^{-1}\frac{\sqrt{21(1-\tilde{\gamma}^2)}}{2}\right), \quad \text{(F3)}$$

respectively. For the sake of completeness, let us reproduce here the result, already presented in equation (23), using the net merger rate definition of equation (15):

$$C_{\rm odd} = \frac{1}{5}\left(\frac{3}{2\pi}\right)^{3/2}(1-\tilde{\gamma}^2)\,. \quad \text{(F4)}$$

A comparison of $C_{\rm odd}$ between total and net merger density is given in Fig. F1 and is shown to be at a few per cent level only. For $\tilde{\gamma}$ above 0.8 (i.e. for a spectral index above -1), there are at least 30 times fewer nucleations than destructions (this ratio is an increasing function of $\tilde{\gamma}$).

APPENDIX G: JOINT PDFS

Let us present here the PDF of the field and its (up to third) derivative, which will allow us to compute the expectations involved in the main text.

G1 One-point PDFs

Since the odd and even-order derivatives of Gaussian random fields do not correlate, let us write the joint PDF as $P_{\rm G} = P_0(x, x_{kl})P_1(x_i, x_{ijk})$. The expression for $P_0(x, x_{kl})$ for the Gaussian field was first given by Bardeen et al. (1986). Introducing the variables

$$u \equiv -\nabla^2 x = -(x_{11}+x_{22}+x_{33})\,, \quad \text{(G1)}$$

$$w \equiv \frac{1}{2}(x_{11}-x_{33})\,, \quad \text{(G2)}$$

$$v \equiv \frac{1}{2}(2x_{22}-x_{11}-x_{33})\,, \quad \text{(G3)}$$

in place of diagonal elements of the Hessian (x_{11}, x_{22}, x_{33}), one finds that u, v, w, x_{12}, x_{13}, and x_{23} are uncorrelated. Importantly, the field, x is only correlated with u and

$$\langle xu\rangle = \gamma, \quad \langle xv\rangle = 0, \quad \langle xw\rangle = 0, \quad \langle xx_{kl}\rangle = 0,\ k \neq l,$$

where γ is the same quantity as in equation (5). The full expression of $P_0(x, x_{kl})$ is then

$$P_0(x, x_{kl}) = \frac{5^{1/2}15^2}{(2\pi)^{7/2}(1-\gamma^2)^{1/2}}\exp\left[-\frac{Q_0+Q_2}{2}\right], \quad \text{(G4)}$$

with the quadratic forms Q_0 and Q_2 given by

$$Q_0 = x^2 + \frac{(u-\gamma x)^2}{(1-\gamma^2)}\,,$$
$$Q_2 = 5v^2 + 15(w^2 + x_{12}^2 + x_{13}^2 + x_{23}^2) = \frac{15}{2}\,\overline{x}_{ab}\overline{x}_{ab}\,, \quad \text{(G5)}$$

where the last identity is demonstrated in Pogosyan et al. (2009b) and involves the detraced tensors:

$$\overline{t}_{ij} = t_{ij} - \frac{1}{3}t_{aa}\delta_{ij}\,, \quad \text{(G6)}$$

$$\overline{t}_{ijk} = t_{ijk} - \frac{3}{5}\,t_{aa(j}\delta_{kl)}\,, \quad \text{(G7)}$$

with an implicit summation over repeated indices and symmetrization between parenthesized indices (e.g. $t_{aa(j}\delta_{kl)} = [t_{aaj}\delta_{kl} + t_{aak}\delta_{lj} + t_{aal}\delta_{jk}]/3$ and so on). Equation (G5) depends only on a single correlation parameter, γ. A similar procedure can be performed for the joint probability of the first and third derivatives of the fields, $P_1(x_i, x_{ijk})$ by defining the following nine parameters (see also Hanami 2001):

$$u_i \equiv \nabla_i u, \quad v_i \equiv \frac{12}{\epsilon}^{ijk}\nabla_i\left(\nabla_j\nabla_j - \nabla_k\nabla_k\right)x, \quad \text{with } j<k\,,$$
$$w_i \equiv \sqrt{\frac{5}{12}}\nabla_i\left(\nabla_i\nabla_i - \frac{3}{5}\nabla^2\right)x, \quad \text{(G8)}$$

and replacing the variables $(x_{i11}, x_{i22}, x_{i33})$ with (u_i, v_i, w_j). In that case, the only cross-correlations in the vector $(x_1, x_2, x_3, u_1, v_1, w_1, u_2, v_2, w_2, u_3, v_3, w_3, x_{123})$ that do not vanish are between the same components of the gradient and the gradient of the Laplacian of the field:

$$\langle x_i u_i\rangle = \tilde{\gamma}/3, \qquad i = 1, 2, 3, \quad \text{(G9)}$$

where $\tilde{\gamma}$ was defined in equation (5). This allows us to write

$$P_1(x_i, x_{ijk}) = \frac{105^{7/2}3^3}{(2\pi)^{13/2}(1-\tilde{\gamma}^2)^{3/2}}\exp\left[-\frac{Q_1+Q_3}{2}\right], \quad \text{(G10)}$$

with the quadratic forms

$$Q_1 = 3\sum_i\left(\frac{(u_i-\tilde{\gamma}x_i)^2}{(1-\tilde{\gamma}^2)} + x_i^2\right),$$
$$Q_3 = 105\left(x_{123}^2 + \sum_{i=1}^{3}(v_i^2+w_i^2)\right), = \frac{35}{2}\,\overline{x}_{ijk}\overline{x}_{ijk}\,. \quad \text{(G11)}$$

G2 Two-point PDFs

Calling $\boldsymbol{x} = (x, x_i, x_{ij}, x_{ijk})$ and $\boldsymbol{y} = (y, y_i, y_{ij}, y_{ijk})$, the joint PDF reads

$$P_2(\boldsymbol{x}, \boldsymbol{y}) = \frac{\exp\left[-\frac{1}{2}\begin{pmatrix}\boldsymbol{x}\\ \boldsymbol{y}\end{pmatrix}^{\rm T}\cdot\mathbf{C}^{-1}\cdot\begin{pmatrix}\boldsymbol{x}\\ \boldsymbol{y}\end{pmatrix}\right]}{\det|\mathbf{C}|^{1/2}\,(2\pi)^{15}}, \quad \text{(G12)}$$

where $\mathbf{C}$ is the covariance matrix that depends on the separation vectors only because of homogeneity :

$$\mathbf{C} = \begin{pmatrix}\mathbf{C}_{xx} & \mathbf{C}_{xy}\\ \mathbf{C}_{xy}^{\rm T} & \mathbf{C}_{yy}\end{pmatrix}. \quad \text{(G13)}$$

Note that $\boldsymbol{x}^{\rm T}\cdot\mathbf{C}_{xx}^{-1}\cdot\boldsymbol{x}$ is given by $Q_0(x)+Q_2(x)+Q_1(x)+Q_3(x)$, where the Q_i are given by equation (G5) and (G11). The cross terms will involve correlations of all components of $\boldsymbol{x}$ and $\boldsymbol{y}$:

$$\mathbf{C}_{xy} = \langle \boldsymbol{x}\cdot\boldsymbol{y}^{\rm T}\rangle\,. \quad \text{(G14)}$$

The correlation length of the various components of $\mathbf{C}_{xy}$ differs, as higher derivatives decorrelate faster. Note that the separations are measured in units of R, whereas the Q_i are independent of R.

APPENDIX H: DETECTION ALGORITHMS

The source code of the implementation is available upon request. It is based on PYTHON and the SCIPY stack (Virtanen et al. 2020).

H1 Critical points detection

This section presents the algorithm used to find the critical points in an N-dimensional field. Let F, F_i, and F_{ij} be a field evaluated on a grid, its derivative, and its Hessian. For any point $\boldsymbol{x}$ on the grid, we have the following relation:

$$F_j(\boldsymbol{x}) = F_j(\boldsymbol{x}_\mathbf{c}) + (x_i - x_{\mathrm{c},i})F_{ij}(\boldsymbol{x}) + \mathcal{O}(\Delta x_i^2). \tag{H1}$$

Critical points are found where $F'_j = 0$ by solving the linear system of equation:

$$\Delta x_i F_{ij} = -F_j, \tag{H2}$$

where $\boldsymbol{\Delta x} = \boldsymbol{x} - \boldsymbol{x}_\mathrm{c}$. The algorithm works as follows:

(i) Solve equation (H2) for each cell on the grid. We then get a set of points $(\boldsymbol{x}^i_\mathbf{c}, \boldsymbol{x}^i)$, where the former is the cell centre and the latter the closest critical point.

(ii) Remove all critical points found at $|\boldsymbol{x}^i_\mathbf{c}, \boldsymbol{x}^i|_\infty \geq \Delta x$, where Δx is the grid spacing.

(iii) For all critical point, compute the value of the Hessian by interpolating linearly from the $2N$ (four in 2D, six in 3D) neighbouring cells.

(iv) Compute the eigenvalues of the Hessians and the type of the critical point (maximum, saddle point(s), or minimum).

(v) Merge all critical points of the same kind closer than Δx. To do this, we first build a KD-Tree of the critical points and find all the pairs located at a distance $d_{ij} = |\boldsymbol{x}^i - \boldsymbol{x}^j|_\infty \leq \Delta x$. For each pair, we keep only the point that is the closest to its associated cell.

H2 Critical event detection

The algorithm is based on the idea that each critical event has two predecessors at the previous smaller smoothing scale (two critical points). Conversely, each critical point has either a critical point successor of the *same kind* at the next (larger) smoothing scale or a critical event. Therefore, a way to detect critical events is to find critical points that do not have a successor. These points will be referred to as 'heads' as they are the tip of a continuous line of critical points in the smoothing scale direction. Critical events are then found between pairs of heads of kind k and $k + 1$ (e.g. a peak and a filament).

Following this idea, the algorithm can be decomposed in two steps: Compute the heads of each kind, and then find pairs of heads to detect critical events. In the rest of the section, let us call R_0 (respectively, R_1) the smallest (respectively, largest) scale at which the field is smoothed. Let $C_{R,k} = \{\boldsymbol{r}_i, R\}_{i=1,\dots,N}$ be the set of the N critical points of kind k at scale R. The whole detection algorithm reads

1: **procedure** FindCritEvents($C_{R,k}$, α)
2: $E \leftarrow \{\}$ ▷ All critical events
3: **for** k **in** $1, \dots, d$ **do** ▷ Find heads of critical points
4: $H_k \leftarrow$ BuildHeads(k, $\Delta \log R$)
5: **end for**
6: $R \leftarrow R_0$
7: **while** $R \leq R_1$ **do** ▷ Find pairs of heads (crit. events)
8: $\Delta R \leftarrow R \times \Delta \log R$ ▷
9: $E \leftarrow E +$ FindHeadPairs($H_1, \dots, H_d, R, \alpha \Delta R$)
10: $R \leftarrow R + \Delta R$
11: **end while**
12:
13: **return** E
14: **end procedure**

The parameter α controls how far heads can be in the smoothing scale direction, in units of $\log R$. A value of 1 looks for pairs of heads at the same scale, and a value of 2 looks for pairs of heads at scales R, $R + \Delta R$.

The first step (line 4) of the algorithm builds the set of heads H_k. It works as follows:

1: **procedure** BuildHeads(k, $\Delta \log R$)▷ Build heads of kind k
2: $H_k \leftarrow C_{R_1,k}$ ▷ Initialise heads
3: $P_k \leftarrow H_k$ ▷ Initialise progenitors
4: $R \leftarrow R_1$
5: **while** $R \geq R_0$ **do**
6: $P'_k \leftarrow \{\}$▷ Initialise new progenitors at R
7: **for** p, c, d **in** SortedPairs(P_k, $C_{R,k}$, R) **do**
8: **if** $c \notin P'_k$ **then**
9: $P'_k \leftarrow P'_k + \{p, c\}$ ▷ Found new progenitor
10: **end if**
11: **end for**
12: $P_k \leftarrow P'_k$
13: **for** c **in** $C_{R,k}$ **do** ▷ Loop over crit. points
14: **if** $c \notin P'_k$ **then** ▷ Keep only unpaired ones...
15: $H_k \leftarrow H_k + \{c\}$ ▷ ... and add them to heads
16: $P_k \leftarrow P_k + \{c\}$
17: **end if**
18: **end for**
19: $R \leftarrow R(1 - \Delta \log R)$
20: **end while**
21:
22: **return** H_k ▷ Heads are points with no successors at larger R
23: **end procedure**

Here, SortedPairs(X, Y, R_max) returns (x, y, d), where x, y are points in X, Y and $d \leq R_\mathrm{max}$ is their relative distance (in $(\vec{r}, R)$ space). The tuples are sorted by increasing distance. This can be efficiently implemented using a KD-tree with periodic boundary conditions. BuildHeads builds all heads by using a watershed approach. Starting from the largest smoothing scales, it finds and discards all critical events that are progenitors of a head at any larger scale. The remaining points have no successor (they are the progenitor of nothing) and are hence heads.

Once the heads have been computed, the second step of the algorithm pairs them (line 9):

1: **procedure** FindHeadPairs($H_1, \dots, H_d, R, \Delta R$) ▷ Find pairs of heads (crit. events)
2: $H_{R,k} \leftarrow \{c \in H_k \,|\, R \leq c.R < R + \Delta R\}$ ▷ Keep heads at scale R
3: $P \leftarrow \{\}$ ▷ Head pair list
4: **for** k **in** $1, \dots, d - 1$ **do**
5: $P \leftarrow P +$ SortedPairs($H_{R,k}$, $H_{R,k+1}$, R)
6: $P \leftarrow P +$ SortedPairs($H_{R,k+1}$, $H_{R,k}$, R)
7: **end for**
8: $P \leftarrow$ SortByDistance(P)
9: $P' \leftarrow \{\}$ ▷ Pairs with no double counts
10: **for** c_1, c_2, d **in** P **do**
11: **if** $c_1 \notin P'$ **and** $c_2 \notin P'$ **then**
12: $P' \leftarrow P' + \{c_1, c_2\}$
13: **end if**
14: **end for**
15: $E \leftarrow \{\}$ ▷ Critical events
16: **for** c_1, c_2 **in** P' **do**
17: $E \leftarrow E +$ CritEventData(c_1, c_2)
18: **end for**

19:
20: **return** E
21: **end procedure**

Lines 5 and 6 ensure that the detection method is invariant by permutation of $k \leftarrow d - k + 1$. CritEventData(c_1, c_2) computes the properties (position, kind, gradient, etc.) of the critical events given by two critical points. FindHeadPairs works as follows. It first finds all pairs of heads separated by less than a smoothing scale. It then loops over all pairs (sorted by increasing distance) and greedily consumes heads. Each head can only be paired once, to its closest not-yet-paired head of either the previous or next kind. This prevents, for example, F critical points from being paired to a P and a W critical point, which would result in a double count. Note that this procedure may leave some heads unpaired (e.g. critical points at the largest smoothing scale do not merge but have no successor). In practice, the unpaired heads typically account for less than a per cent (0.5 per cent for $\Delta R = \alpha R \Delta \log R$ with $\alpha = 2$) of the total number of heads.

This paper has been typeset from a TEX/LATEX file prepared by the author.